Time-Resolved Low-Energy Electron Diffraction and Photoemission Pump-Probe Experiments

---

Dissertation

zur

Erlangung der naturwissenschaftlichen Doktorwürde
(Dr. sc. nat.)

vorgelegt der

Mathematisch-naturwissenschaftlichen Fakultät

der

Universität Zürich

von

Andrei D. Dolocan
aus Rumänien

Promotionskomitee

Prof. Dr. Jürg Osterwalder
Dr. Matthias Hengsberger
Prof. Dr. Peter Hamm

Zürich 2006

Die vorliegende Arbeit wurde von der Mathematisch-naturwissenschaftlichen Fakultät der Universität Zürich auf Antrag von Prof. Dr. Jürg Osterwalder und Prof. Dr. Hans-Werner Fink als Dissertation angenommen.

Search for Order
and you will find your Freedom.
Search for absolute Freedom
and you will become the slave
of your own Desires.

F. Herbert

Zusammenfassung

Die Dimensionen in modernen elektronischen Schaltungen und magnetischen Speichereinheiten erreichten innerhalb der letzten Dekade die Grössenordnung von Nanometern, und damit eine Längenskala, auf der quantenmechanische Prozesse eine dominante Rolle spielen. Das mikroskopische Verständnis fundamentaler Prozesse wie z.B. dem Verhalten der Elektronen und Atome eines Festkörpers in einem zeitlich veränderlichen elektromagnetischen Feld sind von daher Inhalt intensiver Forschungsarbeit. Aufgrund der relevanten atomaren Zeitskala sind ultrakurze Laserpulse ein wichtiges Werkzeug zur Untersuchung der Quasiteilchendynamik. Die erste Grundvoraussetzung zur Durchführung solcher Experimente ist die Charakterisierung ultrakurzer Laserpulse. Von besonderer Bedeutung sind hierbei die Pulsform und die Pulsdauer. Im ersten Teil der vorliegenden Dissertation werden mehrere experimentelle Methoden zur Pulscharakterisierung vorgestellt und auf die von unserem Lasersystem produzierten Pulse angewandt.

Im Hauptteil der Arbeit wird auf zwei zeitaufgelöste Methoden zur Untersuchung der elektronischen und strukturellen Dynamik in Festkörperoberflächen eingegangen. Die besetzte und unbesetzte elektronische Bandstruktur einer neuartigen, in unserer Gruppe gefundenen Struktur, der sogenannten *nanomesh* und deren Dynamik wird im ersten Teil mittels zeitaufgelöster Zwei-Photonen-Photoemission (2PPE) untersucht. Diese Struktur besteht aus einem komplexen und sehr regelmässigen Bornitrid-Netzwerk von Löchern, das sich auf einer Rhodium (111)-Oberfläche bildet. Mittels 2PPE konnten Rhodiumbänder nahe des Ferminiveaus aufgelöst werden. Desweiteren kann aus der Abhängigkeit der Spektren von der Photonenenergie auf einen Bornitridzustand geschlossen werden, dessen energetische Position ausserhalb des uns spektroskopisch zugänglichen Bereiches lag. Seine Lebensdauer konnte in zeitaufgelösten Experimenten abgeschätzt werden. Diese Resultate liefern erste Informationen zur Leitungsbandstruktur des isolierenden Bornitridnetzwerkes.

Rekonstruktionen von Oberflächen und häufig damit verbundene Instabilitäten gegenüber Phasenübergängen und deren Verständnis sind von grosser Bedeutung und können mit Strukturbestimmungsmethoden untersucht werden. Vor allem Phasenübergänge sind hierbei äusserst interessant, weil man nahe des kritischen Punktes Situationen fern des thermodynamischen Gleichgewichts durch die Einwirkung eines intensiven Lichtpulses studieren kann. Die dabei angewandte *pump-probe* (Pump-Abfrage) Technik erlaubt es, solche Prozesse stroboskopisch in Echtzeit zu studieren. Beugung langsamer Elektronen (LEED für *low-energy-electron diffraction*) ist das Standardwerkzeug zur Bestimmung der atomaren Struktur von Oberflächen. Diese Arbeit trug zur Entwicklung eines einzigartigen zeitaufgelösten LEED-Experimentes bei. Drei verschiedene gepulste Elektronenquellen wurden dabei charakterisiert und für erste Testexperimente an verschiedenen Systemen, wie der c(2×8)-Rekonstruktion der Ge(111)-Fläche und der Indium-induzierten 4×1 Rekonstruktion der Si(111)-Oberfläche, benutzt. Die Entwicklung eines Korrelationsexperimentes für Licht- und Elektronenpulse war ausschlaggebend für die ersten erfolgreichen Messungen von Transienten mit Elektronenpulsen mit einer Zeitauflösung von etwa 70 Picosekunden bei tiefen kinetischen Energien. Die ersten zeitaufgelösten LEED-Testexperimente basierten auf der Messung der Intensität verschiedener Beugungsmaxima als Funktion des Zeitversatzes von Laserpump- und Elektronenabfragepuls. Die Intensität, die während der vorübergehenden Temperaturzunahme

des Gitters aufgrund des Debye-Waller-Effektes abnimmt, wird hierbei als schnelles Thermometer genutzt. Aufgrund der niedrigen Debyetemperatur des In 4×1 Si(111)–Systems und des scharfen Phasenüberganges bei 110 K war dieses System ein guter Kandidat für erste zeitaufgelöste LEED-Experimente. Die Transienten zeigten allerdings nur sehr schwache Effekte, die mit einem kurzzeitigen Temperaturanstieg unvereinbar sind, und mindestens zum Teil durch eine kurzzeitige Raumladung, gebildet durch vom Pumppuls erzeugte Photoelektronen, erklärt werden können.

Abstract

With technology reaching towards the nanoscale level, science is in pursue of new methods for understanding this emerging quantum world. Fundamental processes like the electronic or structural response of solids to time-dependent coherent electromagnetic excitation are therefore subject to intensive research. These microscopic processes can only be studied at their length and time scale by pump-probe experiments. Ultrashort laser pulses are the main tool for the investigation of ultrafast quasiparticle dynamics in different media. Hence, the characterization of ultrashort laser pulses is the first requirement when performing time-resolved experiments. An important property of a laser pulse is its shape and in particular its temporal width. Therefore, several pulse diagnostic methods are discussed and applied for the case of our laser system.

The main topics of the present thesis refer to the electronic structure and dynamics of a nanostructured interface on one hand, and to the development of a time-resolved structural tool on the other hand. The occupied and unoccupied electronic band structure of a new boron nitride nanostructure forming on a rhodium (111) surface found recently in our group, the so-called *nanomesh*, was investigated by means of two-photon photoemission (2PPE). The photon-energy dependence of one- and two-color 2PPE spectra helps to identify transitions from occupied rhodium bulk states and give evidence for a BN-derived interface state about 3 eV above the Fermi level. Also, the lifetime of the intermediate state could be estimated. These findings provide some first experimental information on the conduction band states in this insulating boron nitride layer.

Phase transitions at surfaces or surface reconstructions are subject to detailed studies by surface structural methods. Moreover, non-equilibrium situations, produced by sudden energy deposition by means of ultrashort laser pulses on surfaces close to the critical temperature, can be investigated. Pump-probe techniques have the potential to follow the excitation and structural relaxation dynamics at a surface in real time. Low-energy electron diffraction (LEED) is a common method for investigating the long-range order of surfaces. This thesis contributes to the development of time-resolved LEED (t-LEED). Three different pulsed electron guns have been used for performing test experiments on various systems, including the Ge(111)-c(2×8) surface and the In/Si(7×7)-(4×1) surface forming In nanowires. The development of a new method for establishing both spatial and temporal overlap of electron and laser pulses helped to overcome one of the major obstacles for this technique. The electron-photon correlator based on a metal pinhole can be also used for estimating the time duration of the electron pulses. The t-LEED test experiments were designed to monitor the transient temperature rise upon arrival of the pump pulse by a Debye-Waller effect in a LEED spot intensity. Due to the fact that the In/Si(7×7)-(4×1) surface exhibits a surface phase transition at $T = 110$ K and a relatively low Debye temperature of ~ 370 K, it was considered as a good candidate for t-LEED measurements. However, due to the very weak temperature increase induced by the pump pulses, the maximum transient effect observed for this surface was less than 0.5%, and it was recognized that the space charge produced by the pump laser pulses at the surface is responsible for at least part of this small effect.

Contents

List of Acronyms

IAC	Intensity Autocorrelation
ICC	Intensity Cross-correlation
FRAC	Fringe Resolved Autocorrelation
ARUPS	Angle-Resolved Ultraviolet Photoemission Spectroscopy
BBO	β-Barium Borate
SHG	Second Harmonic Generation
BZ	Brillouin Zone
DOS	Density Of States
ESCA	Electron Spectroscopy for Chemical Analysis
FWHM	Full Width at Half Maximum
LEED	Low-Energy Electron Diffraction
t-LEED	Time-Resolved LEED
ML	Mono-Layer
ARPES	Angle Resolved Photoelectron Spectroscopy
PE	Photoemission
PES	Photoelectron Spectroscopy/Spectrum
2PPE	Two-Photon Photoemission
t-2PPE	Time-Resolved Two-Photon Photoemission
QP	Quasi-Particle
SBZ	Surface Brillouin Zone
STM	Scanning Tunneling Microscopy
UPS	Ultraviolet Photoemission Spectroscopy
XPS	X-ray Photoemission Spectroscopy
RT	Room Temperature
CC	Cross-Correlation
CC map	Cross-Correlation Map
RB	Red-Blue 2PPE
BB	Blue-Blue 2PPE
UHV	Ultra High Vacuum
0-delay	Zero-delay, Coincidence
fcc	Face Centered Cubic (lattice)

Chapter 1

Introduction: Time Resolved Experiments

In the last decade the information technology has grown enormously. Therefore more tools and media which allow for fast computing and huge storage capacities are urgently needed. Looking at the main picture it is obvious that new technologies which can reach molecular and atomic level are the next logical development step for digital storage. Even though being able to read and write digital information at the atomic level can change dramatically the available storage capacities, the new technology must be accompanied by very fast and safe data storage procedures. Otherwise the new subnano-scale memories can not provide enough access speed to be actually useful at the commercial level. For this purpose, researchers are looking at organized atomic surfaces in order to develop viable two-dimensional systems as future storage devices. The stability issues arising are very complicated due to the fact that, at the atomic level, electronic quantum effects play a key role in the way the surfaces behave. In other words, the physics which reaches towards one or two dimensions is no longer the well-known physics in three dimensions on which most of the actual electronic devices base their functionality. Development of novel switching devices in the emerging field of *spintronics* requires a better understanding of the interfaces between magnetic and non-magnetic, metallic, semiconducting and insulating materials [1]. Detailed understanding of microscopic mechanisms requires experimental observation of atomic systems at their microscopic length and time scale (nanometers and femtoseconds). Since the demonstration of the first Ti:sapphire solid state pulsed laser in 1990, the ultrashort laser pulses are increasingly used as the main tool for real-time observation of ultrafast processes.

Nowadays, *smaller* and *faster* are the key words for new scientific developments. Many-body systems with excess internal energy relax towards states of lower energy by rearrangement of molecular, atomic or nuclear structure. Observing these processes in real time requires a pump pulse for initiating the microscopic dynamics and a delayed probe pulse for detecting transition states of the evolving system [2]. Time-resolved spectroscopy which makes use of femtosecond laser pulses is now used for tracking atomic motion in molecules [3] or quasiparticle dynamics at surfaces [4]. Time-resolved two-photon photoemission (t-2PPE) is the common method for probing the charge carrier dynamics in solids as it incorporates many of the surface analytical capabilities of photoemission (PE) and inverse photoemission (IPE) (the traditional probes for surface and bulk band structures) with time-resolution that is approaching the fundamental response of electrons to optical excitation [5]. t-2PPE experiments performed on a system with an unknown unoccupied band structure can provide invaluable information which can be used as input for density functional calculations (DFT).

On the other hand, fast structural changes in solid surfaces can only be observed with short electron pulses. Such knowledge is crucial for understanding a series of phenomena like phase transitions [6] or surface reconstructions [7]. One of the standard tools for surface structural investigation is low-energy electron diffraction (LEED) [8]. Generation of low-energy electron pulses is done with ultrashort laser pulses which hit the cathode of a so-called LEED gun [9–11]. Unfortunately, one encounters several difficulties when using low-energy electron pulses: (1) the time width of such pulses is hardly smaller than 10 picoseconds even if very short laser pulses are used (under 100 femtoseconds); (2) it is very difficult to induce in a solid system a coherent fully reversible surface structural change which is sufficiently strong to be resolved by the LEED patterns.

The main part of this thesis is addressing both the issues of electronic and structural dynamics. Characterization of the ultrashort pulses is the first step when performing time-resolved experiments. Therefore, most of the tools which deal with the femtosecond pulse diagnostics are reviewed. t-2PPE experiments performed on a newly found system in our group, the so-called *nanomesh* [12], provide notable information about its unoccupied band structure which can be used as input for further calculations [13]. Further, two electron guns have been used for real time observation of surface structural changes. A new robust method for correlating the electron and laser pulses has been developed which makes it easier to set up a t-LEED experiment [14]. This method gives also an upper limit estimation for the time duration of the electron pulses. t-LEED experiments have been performed on Ge(111)-c(2×8) and In/Si(111)-(4×1) surfaces. Unfortunately, due to the very small induced surface temperature increase, only the transient space charge produced by the pump laser pulses was observed.

Chapter 2

Pulsed Laser

2.1 Gaussian Beam Optics

The Maxwell equations for the electromagnetic field describe the existence of traveling wave solutions which provide the spatial and temporal energy transport. In an infinite medium with no sources they lead to

$$\nabla \times \mathbf{E} - i\omega\mathbf{B} = \mathbf{0}\,; \quad \nabla \times \mathbf{B} + i\omega\epsilon\mu\mathbf{E} = \mathbf{0} \tag{2.1.1}$$

which combined with the zero-divergence equations give the Helmholtz wave equation [15]

$$(\triangle + \mu\epsilon\omega^2)\left\{ \begin{array}{c} \mathbf{E} \\ \mathbf{B} \end{array} \right\} = \mathbf{0} \tag{2.1.2}$$

The latter admits solutions of the form

$$\left\{ \begin{array}{c} \mathbf{E} \\ \mathbf{B} \end{array} \right\}(\mathbf{r}, t) = \left\{ \begin{array}{c} \mathbf{E_o} \\ \mathbf{B_o} \end{array} \right\} e^{i(\mathbf{k}\cdot\mathbf{r} - \omega t)} \tag{2.1.3}$$

where the wave vector

$$\mathbf{k} = \sqrt{\epsilon\mu}\,\omega\,\mathbf{n} = \frac{\omega}{v_\phi}\mathbf{n} \tag{2.1.4}$$

with $\mathbf{n}$, $\mathbf{E_o}$ and $\mathbf{B_o}$ constant complex vectors, $\mid \mathbf{n} \mid = 1$ and the wave *phase velocity*

$$v_\phi = \frac{\omega}{\mid \mathbf{k} \mid} = \frac{1}{\sqrt{\epsilon\mu}} = \frac{c}{n} \tag{2.1.5}$$

The quantity n is called the *index of refraction* and is usually a complex function of the frequency.

The solutions in eq. 2.1.3 are describing a *plane wave* and they are written in the convention that the physical electric and magnetic fields are obtained by taking the real parts of the complex quantities $\mathbf{E}$ and $\mathbf{B}$. The most general possible solution for a plane wave is provided in the case where $\mathbf{n}$ is a complex unit vector ($\mathbf{n} = \mathbf{n_R} + i\mathbf{n_I}$) which makes the exponential in eq.(2.1.3) $e^{i(k\mathbf{n}\cdot\mathbf{r} - \omega t)} = e^{-k\mathbf{n_I}\cdot\mathbf{r}} e^{i(k\mathbf{n_R}\cdot\mathbf{r} - \omega t)}$. The resulting wave is called *inhomogeneous plane wave* because it possesses exponential growth or decay in a certain direction. As a result, the plane surfaces with constant phase and amplitude are no longer parallel.

One important property of the plane waves is the *polarization*, which describes the orientation of the fields in time and space. Given a real $k\mathbf{n}$ wave vector and two other independent unit vectors $\{\mathbf{u_1},\mathbf{u_2}\}$ chosen such that they form an orthogonal basis in the real three-dimensional space together with $\mathbf{n}$, it can be shown[a] that the most general *homogeneous plane wave* propagating in the direction $\mathbf{k}$ is written as

$$\mathbf{E}(\mathbf{r},t) = (\mathbf{u_1}E_1 + \mathbf{u_2}E_2)e^{i(\mathbf{k}\cdot\mathbf{r}-\omega t)} \tag{2.1.6}$$

and

$$\mathbf{B}(\mathbf{r},t) = \frac{\sqrt{\epsilon\mu}}{k}\,\mathbf{k}\times(\mathbf{u_1}E_1 + \mathbf{u_2}E_2)e^{i(\mathbf{k}\cdot\mathbf{r}-\omega t)} \tag{2.1.7}$$

as a superposition of two *linear polarized* plane waves. In order to allow the possibility of a phase difference between the two waves, the amplitudes E_1 and E_2 are taken as complex numbers. The polarization state of a beam of light (either natural or totally or partially polarized) is completely described with the four *Stokes parameters*, proposed by G. G. Stokes in 1852. These parameters are quadratic in the electric field strength and can be determined through intensity measurements, together with a linear polarizer and a quarter-wave plate [15–18].

In 1941 R. C. Jones has invented another representation for the polarized light which complements that of the Stokes parameters: the *Jones vectors*. This technique is very concise and can be used to describe coherent beams but it is *only applicable to polarized waves* [17, 19].

Another simple solution of the Helmholtz equation 2.1.2 is the *spherical wave*

$$E(\mathbf{r},t) = \frac{E_o}{r}\exp[i(\omega t - kr)] \tag{2.1.8}$$

where r is the distance from the origin and $k = |\mathbf{k}|$ is the norm of the wave vector. Sufficiently close to the z axis but far away from the source, the spherical wave can be described through the *Fresnel approximation* [20]

$$E(\mathbf{r},t) \approx \frac{E_o}{z}\exp[i(\omega t - kz)]\exp\left[-ik\,\frac{\rho^2}{2z}\right] \quad , \quad \rho^2 = x^2 + y^2 \tag{2.1.9}$$

In other words, at points near the z axis and sufficiently far from the origin, the spherical wave can be approximated by a *paraboloidal* wave. For very far points it approaches the plane wave.

If the wave fronts (*i.e.* surfaces of constant phase) have normals which are very close to the propagation direction then the wave is said to be *paraxial.* It can be constructed from a plane wave with a complex amplitude which is allowed to slowly vary with the position, $E(\mathbf{r},t) = A(\mathbf{r})\exp[i(\omega t - kz)]$. This amplitude must satisfy the *paraxial Helmholtz equation*[b] [20] and has the form

$$A(\mathbf{r}) = \frac{A_o}{q(z)}\exp\left[-ik\,\frac{\rho^2}{2q(z)}\right] \quad , \quad q(z) = z + iz_o \tag{2.1.10}$$

---

[a] from the Maxwell equations we have $\mathbf{k}\perp\mathbf{E}\perp\mathbf{B}$, which means that the fields are in the same plane orthogonal to the direction of propagation

[b] $(\partial_x^2 + \partial_y^2 - 2ik\partial_z)A = 0$

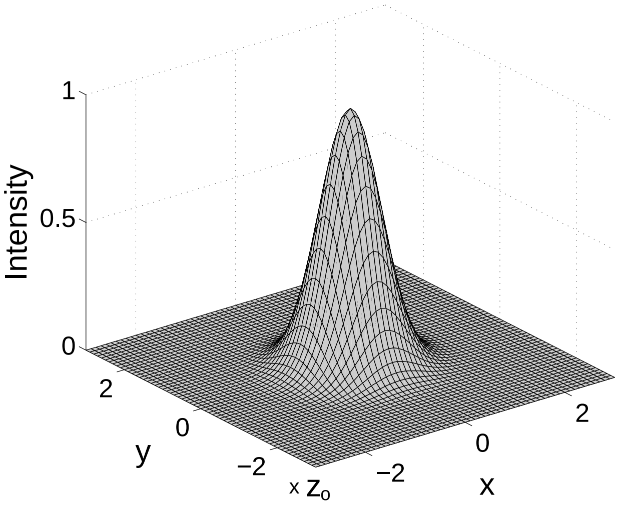

Figure 2.1: *The intensity* $|E(\mathrm{r},t)|^2$ *of a Gaussian beam with* $W_o = \sqrt{z_o}$ *at* $z = 0$*. The* x *and* y *coordinates are given in* z_o *units.*

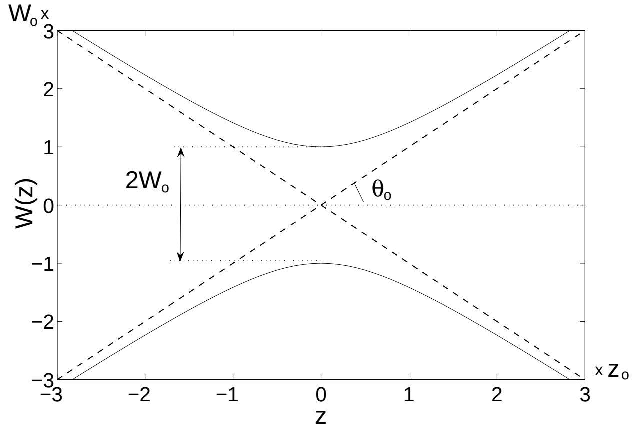

Figure 2.2: *The width evolution of a Gaussian beam with* $W_o = \sqrt{z_o}$ *at* $z = 0$*. The* z *coordinate is given in* z_o *units while* W *is expressed in terms of* W_o*.*

where the real parameter z_o is known as the *Rayleigh range*. By defining two new real functions $R(z)$ and $W(z)$ such that[c]

$$\frac{1}{q(z)} = \frac{1}{R(z)} - i\,\frac{\lambda}{\pi W^2(z)} \tag{2.1.11}$$

and replacing $q(z)$ in the eq. 2.1.10 and further in the eq. 2.1.9 one obtains the *Gaussian beam*

---

[c] λ is the wavelength of the electromagnetic wave

wave (figs. 2.1 and 2.2).

$$E(\mathbf{r},t) = A_o \frac{W_o}{W(z)} \exp\left[-\frac{\rho^2}{W^2(z)}\right] \exp\left\{i\left[\omega t - kz - k\frac{\rho^2}{2R(z)} + \tan^{-1}\left(\frac{z}{z_o}\right)\right]\right\} \tag{2.1.12}$$

where $W(z) = W_o\sqrt{1+(z/z_o)^2}$ is the beam radius at a given distance z from the origin $z = 0$, $R(z) = z[1+(z_o/z)^2]$ is the radius of the wavefront and $W_o = \sqrt{\lambda z_o/\pi}$ is the so called *beam waist*[d] (smallest beam radius possible, at origin). Far from the beam center, when $z \gg z_o$, the beam radius increases linear with z, defining a cone with a half-angle (fig. 2.2)

$$\theta_o = \frac{\lambda}{\pi W_o} \tag{2.1.13}$$

which confines about 86% of the beam power. At $z = z_o$ the radius of the wavefront is the smallest so it has the greatest curvature $(2z_o)^{-1}$.

2.2 What is a Short Laser Pulse?-Theoretical Description

Through *population inversion* in a *gain medium* one can amplify light *coherently*, with the help of a *resonant cavity* and *stimulated emission.* In 1960 T. H. Maiman set up the first operating CW-laser [21] using Cr^{3+}:Al_2O_3 (Cr:sapphire) as gain medium. Fundamentally the laser is formed by pulses in the time domain as the gain medium gets depleted every few *round trips* (the resonant cavity has a limited dimension), when the maximum possible intensity is output. A short laser pulse is simply a very short burst of coherent electromagnetic energy [22]. In order to generate it one needs three main ingredients [23–25]: *Broad Gain Medium* (laser dyes, Ti:apphire or related solid state laser materials), *Phase Locking* (active, passive) and *Dispersion Control.* If one considers a laser resonator of length l, the electric field at the output coupler can be written as a superposition of a certain subset of longitudinal modes which are favored by the finite *gain bandwidth* of the laser medium.

$$E(t) = \sum_n E(\omega_n)e^{i\omega_n t} = \sum_n E(\omega_n)e^{i2\pi n\frac{c}{2l}t} \tag{2.2.14}$$

where $E(\omega)$ is related (and not necessarily equal) to the gain profile of the medium. The above discrete Fourier transformation is periodic in time and it will yield a pulse train at the output coupler with a frequency given by the round trip time through the resonator $\nu_{rt} = c/2l$. The frequency spacing between the neighboring modes is very small compared to the central frequency of the gain profile. This allows one to use the *continuous Fourier transformation* instead of the discrete one

$$E(t) = \int_{-\infty}^{\infty} d\omega\, E(\omega)e^{i\omega t} \tag{2.2.15}$$

---

[d] $2W_o$ is called the *spot size*

together with the *inverse Fourier transformation*

$$E(\omega) = \frac{1}{2\pi} \int\limits_{-\infty}^{\infty} dt\, E(t) e^{-i\omega t} \tag{2.2.16}$$

As the laser pulse travels through some material inside the cavity, it is natural to assume that it will acquire also a *spectral phase* $\phi(\omega)$:

$$E(t) = \int\limits_{-\infty}^{\infty} d\omega\, E(\omega) e^{i(\omega t + \phi(\omega))} \tag{2.2.17}$$

which can be completely *random*, implying that the output of the resonator is not actually a pulse but incoherent light (noise). In order to prevent this from happening one has to force all the modes to have the same phase, a mechanism called *mode-locking.*

Theoretically a femtosecond laser pulse is described in the time domain as a *harmonic oscillatory function* (like *cosine*) modulated by a *Gaussian envelope*

$$E(t) = E_o \exp\left\{-\frac{t^2}{\sigma} + i\omega t\right\} \tag{2.2.18}$$

because it is the easiest model to perform Fourier transformations and other pulse-specific calculations. However, in reality one finds rarely a Gaussian pulse. Therefore, when the problem requires a more realistic approach, the *secant hyperbolic* (sech(x)=[cosh(x)]$^{-1}$) pulse shape is sometimes used:

$$E(t) = E_o \frac{2}{e^{t/\sigma} + e^{-t/\sigma}}\, e^{i\omega t} = E_o \,\mathrm{sech}\left(\frac{t}{\sigma}\right) e^{i\omega t} \tag{2.2.19}$$

which is the solution of the models describing pulse formation in femtosecond laser resonators.

The *Heisenberg uncertainty principle* states that, at the quantum level, *two conjugate variables* of a system can not be determined *simultaneously.* In the most general form it holds for *all* physical quantities with *noncommuting* operators [26]. The *uncertainty* of a *measured* quantity x is given by the *standard deviation*

$$\langle \Delta x \rangle = \sqrt{\langle x^2 \rangle - \langle x \rangle^2} \tag{2.2.20}$$

where the *expectation values* are expressed in terms of the system *Hamiltonian eigenvectors* $\{\Psi(x)\}$:

$$\langle x \rangle = \frac{\langle \Psi | x | \Psi \rangle}{\langle \Psi | \Psi \rangle} = \frac{\int_{-\infty}^{\infty} dx\, \Psi^* x \Psi}{\int_{-\infty}^{\infty} dx\, \Psi^* \Psi} \tag{2.2.21}$$

For photons $\langle \Delta E \rangle = \hbar \langle \Delta \omega \rangle$, so the universal time-energy quantum inequality becomes [25, 27]

$$\langle \Delta t \rangle \langle \Delta \omega \rangle \geq \frac{1}{2} \tag{2.2.22}$$

In the context of a laser pulse, $\langle \Delta \omega \rangle$ refers to the spectral bandwidth of the pulse while $\langle \Delta t \rangle$ describes the pulse temporal duration. Also, the pulse electric field E plays the role of the wavefunction Ψ. The meaning of the inequality above is that the pulse (*i.e* a statistically large group of photons) can not be localized both in time and frequency domain. Therefore, setting the localization time interval for a group of photons implies that they will necessarily have a minimum probable energy range.

For a perfectly mode-locked pulse, which has the instantaneous frequency constant in time and an envelope that can be described through an analytical function (like Gaussian or sech) in time and frequency, the *Time-Bandwidth Product* $\langle\Delta t\rangle\langle\Delta\omega\rangle$ is minimal. Such pulses are called *Fourier Transform Limited* (FTL). From all the possible FTL pulses the Gaussian shape envelope produces the smallest time-bandwidth product, 1/2. If a FTL pulse is described by *another* analytical function (like sech, for example) then the time-bandwidth product equality *still holds* but for a constant *larger* than 1/2. *The main conditions for a pulse to be FTL are that the instantaneous frequency is constant in time and that it has a symmetric spectrum.*

In practice one uses the quantities $\overline{\Delta t}$ and $\overline{\Delta\omega}$, which are defined as the *Full-Width at Half-Maximum* (FWHM) of the intensities ($I \sim |E|^2$) of the pulse in the time and frequency domain, respectively, because they are easier to measure.

As an example, for a Gaussian pulse of the form

$$E(t) = E_o \exp\left\{-\frac{t^2}{\sigma} + i\omega_o t\right\} \tag{2.2.23}$$

the intensity ($|E(t)|^2$) duration (*time-width*) reads

$$\overline{\Delta t} = \sqrt{2\sigma \ln 2} \tag{2.2.24}$$

while in the frequency domain the field becomes

$$E(\omega) = \frac{1}{2\pi}\int_{-\infty}^{\infty} dt\, E(t)e^{-i\omega t} = \frac{E_o}{2}\sqrt{\frac{\sigma}{\pi}}\exp\left\{-\frac{\sigma}{4}(\omega-\omega_o)^2\right\} \tag{2.2.25}$$

with the intensity ($|E(\omega)|^2$) spectral width

$$\overline{\Delta\omega} = 2\sqrt{\frac{2\ln 2}{\sigma}} \tag{2.2.26}$$

The time-bandwidth product is then simply

$$\overline{\Delta t}\cdot\overline{\Delta\omega} = 4\ln 2 \tag{2.2.27}$$

or

$$\overline{\Delta t}\cdot\overline{\Delta\nu} = \frac{2\ln 2}{\pi} = 0.441 \tag{2.2.28}$$

Following the same algorithm in the case of a sech-pulse one finds

$$\overline{\Delta t}\cdot\overline{\Delta\nu} = \left[\frac{\ln\left(3+2\sqrt{2}\right)}{\pi}\right]^2 = 0.315 \tag{2.2.29}$$

It is important to mention that the standard deviations refer more to the localization in time and frequency domain than to the actual duration and bandwidth of the pulse. As expected, the Gaussian shape leads to $\langle\Delta t\rangle = \sqrt{\sigma}/2$ and $\langle\Delta\omega\rangle = 1/\sqrt{\sigma}$ whose product is identical 1/2. Commonly, the FWHM quantities $\overline{\Delta t}$ and $\overline{\Delta\omega}$, defined above, are in fact used as the pulse temporal and spectral widths.

The quality of a short laser pulse is reflected (but not completely determined) by it's time-bandwidth product. If the time-width and the spectrum of a real pulse are measured experimentally then their product is minimal when the pulse is perfectly mode-locked. As a further consequence, a laser pulse which is very short in time will have a broad spectra in order to match the natural time-bandwidth requirements.

2.3 Short History of Pulsed Lasers

Ultrafast lasers have a relatively short history. They can be classified in three major generations [28] related to different optical development breakthroughs. The first generation emerged from lamp-pumped solid state, dye and gas lasers, actively or passively mode-locked, which were able to produce pulses of a few picoseconds. The proof of the first mode-locked laser was made in 1964 [29] with a He-Ne laser which generated nanosecond pulse widths. Shortly after the discovery of the CW dye laser [30] the second generation (CW mode-locked dye lasers) appeared [31]. These lasers make use of the strong gain (absorption) in the dyes to induce greater pulse compression, down to 30 fs. However, due to the dyes' limited lifetime and their health impact, they were soon replaced by femtosecond solid state lasers (the third generation), which are at present mostly used in ultrafast applications. The demonstration of the Ti:sapphire as a broadly tunable solid state laser medium [32] led to the first femtosecond argon ion pumped Ti:sapphire laser in 1990 [33] which generates pulses down to 60 fs. The mode-locking mechanism was explained in terms of the nonlinear *Optical Kerr Effect* [34,35]: an intense electromagnetic wave passing through an isotropic medium changes its dielectric response which translates in an instantaneous *linear* dependency of the refractive index with the intensity of the field ($|E(\mathbf{r},t)|^2$)

$$n(\mathbf{r},t) = n_o + n_1 I(\mathbf{r},t) \tag{2.3.30}$$

Longitudinal and transverse to the beam propagation direction, respectively, the index change, induced by the laser pulse itself, leads to the *Self-Phase-Modulation* (creation of new frequencies at the sides of an intense pulse which passes through a medium with a time-dependent index of refraction, the basic method for pulse compression) and the *Kerr Lens Effect* (a laser beam will undergo focussing while passing through a medium with a transverse variable refractive index, due to its variable cross-beam intensity).

During the last decade, the pulsed lasers became more powerful and ergonomic [28,36]. The 100 fs barrier was broken in 1978 [37] while in 1985 the first pulses under 10 fs became available through compression [38–40]. In the visible range the period of the optical wave is a few femtoseconds. This natural limitation forbids pulses to get shorter than $\simeq$ 5 fs, for which the width is about 2 optical cycles (in near-IR) [36]. However, in the last few years, the advancements made in producing the

High-Order Harmonics of femtosecond pulses in rare gases led to the first *attosecond* pulses in the far ultra-violet (UV) and X-ray range [41, 42]. Unfortunately the manipulation of this kind of pulses is rather difficult as the common optical components in the visible range can not be used. Moreover, the physical information is extracted indirectly through complicated analysis [2, 41–43].

2.4 Group Velocity Dispersion and Chirp

The index of refraction of any medium is a function of the frequency of the electromagnetic wave which is passing through. This effect is called *dispersion.* For a short pulse, which has naturally a wide spectrum, various wavelengths travel with different velocities while it propagates through a transparent material. This phenomenon represents the so called *chirp* (delay between frequency components) as the pulse undergoes a phase distortion increasing its duration. As a result, a pulse that was FTL before will no longer be FTL after passing through the material. This happens for any optical element and needs to be corrected in case of sensitive experiments. Most of the time the effect can be neglected for picosecond pulses but becomes very important for 100 fs pulses and even the limiting problem for sub 10 fs pulses.

A FTL pulse passing through a medium of length x will acquire a spectral phase due to the dispersion

$$\phi(\omega) = k(\omega) \cdot x \tag{2.4.31}$$

with the wave vector

$$k(\omega) = \frac{\omega \cdot n(\omega)}{c} \tag{2.4.32}$$

Therefore the pulse becomes

$$E(t) = \int_{-\infty}^{\infty} d\omega \, E(\omega) \, e^{i[\omega t - k(\omega) x]} \tag{2.4.33}$$

while the spectral intensity $I(\omega) = |E(\omega)e^{-i\phi(\omega)}|^2 = |E(\omega)|^2$ remains unchanged as long as only linear optics is used (beam splitters, gratings, etc.), *i.e.* no new frequency components can be generated[e]. In the theoretical treatment of the pulse propagation it is common to Taylor-expand the wave vector $k(\omega)$ around the center frequency ω_o of the pulse in order to model an approximation of the effects encountered:

$$k(\omega) = k(\omega_o) + d_\omega k(\omega_o)(\omega - \omega_o) + \frac{1}{2} d_\omega^2 k(\omega_o)(\omega - \omega_o)^2 + ... \tag{2.4.34}$$

Considering the above expansion in eq. 2.4.33 one can calculate for a FTL Gaussian pulse of the form of eq. 2.2.25

$$\begin{aligned} E(t,x) = E_o \sqrt{\frac{\sigma}{\sigma + i2xd_\omega^2 k(\omega_o)}} \exp\Bigg\{ &-\frac{\sigma}{\sigma^2 + 4x^2[d_\omega^2 k(\omega_o)]^2} \left(t - \frac{x}{v_g(\omega_o)}\right)^2 \\ &+ i \left[\frac{2xd_\omega^2 k(\omega_o)}{\sigma^2 + 4x^2[d_\omega^2 k(\omega_o)]^2} \left(t - \frac{x}{v_g(\omega_o)}\right)^2 + \omega_o \left(t - \frac{x}{v_\phi(\omega_o)}\right) \right] \Bigg\} \end{aligned} \tag{2.4.35}$$

---

[e] However, there can be components depleted by absorption

where the *group velocity* v_g is defined as the speed of the pulse envelope

$$v_g(\omega) = d_k\omega(\omega) = \frac{c}{n(\omega)}\left[1 + \frac{\omega}{n(\omega)}\,d_\omega n\right]^{-1} \simeq v_\phi(\omega)\left[1 - \frac{\omega}{n(\omega)}\,d_\omega n\right] \tag{2.4.36}$$

or in terms of the wavelength

$$v_g(\lambda) = v_\phi(\lambda)\left[1 + \frac{\lambda}{n(\lambda)}\,d_\lambda n\right] \tag{2.4.37}$$

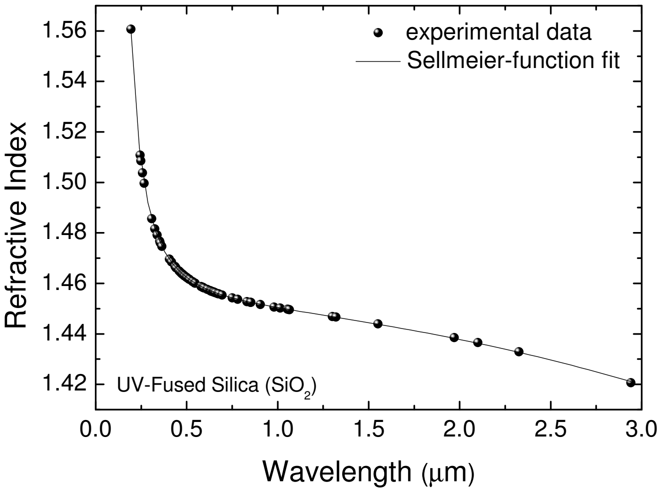

Figure 2.3: *The Sellmeier function ($j \leq 3$) is fitting the experimental data for the UV-fused Silica (SiO$_2$). Data from ref. [44].*

The dispersion $n(\lambda)$ for a specific material is usually described by the *Sellmeier equation* [16, 45]

$$n^2(\lambda) = 1 + \sum_{j>0} \frac{Aj\lambda^2}{\lambda^2 - \lambda_{oj}^2} \tag{2.4.38}$$

where A_j are constants and λ_{oj} are associated with natural absorption wavelengths for that material. These constants are found experimentally (fig. 2.3). Most of the media have *natural dispersion* meaning that $n(\lambda)$ decreases continuously with increasing wavelength. As a result, for these media, the group velocity is always smaller than the phase velocity while the pulse propagates. In other words the frequency components of the pulse travel faster than their envelope[f].

Looking at eq. 2.4.35 one can easily deduce that the pulse envelope is delayed by

$$t' = t - \frac{x}{v_g(\omega_o)} = t - x\,d_\omega k(\omega_o) = t - x\,\frac{n(\lambda_o)}{c}\left[1 - \frac{\lambda_o}{n(\lambda_o)}\,d_\lambda n(\lambda_o)\right] \tag{2.4.39}$$

---

[f] These plane wave components ($E_o\delta(\omega_o)$) do not carry any information because of their infinite duration and therefore the pulse energy propagates with the group velocity.

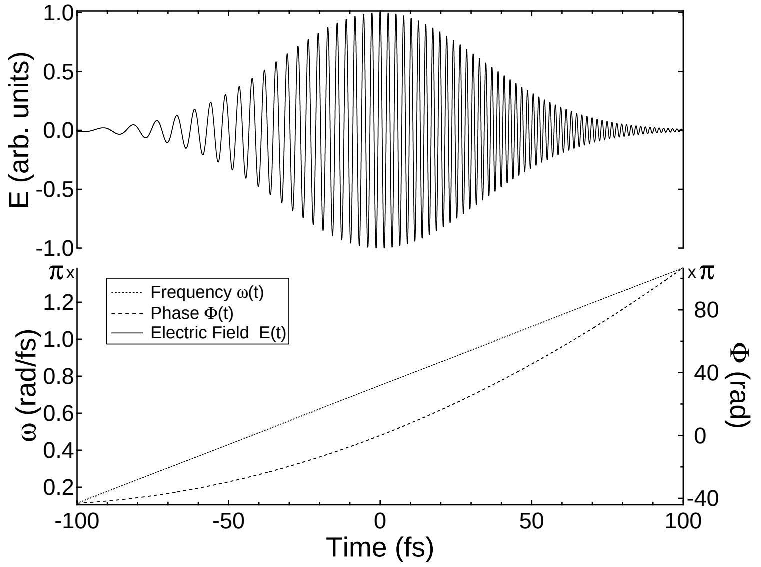

Figure 2.4: *Example of a calculated 55 fs FWHM Gaussian pulse with the central wavelength* $\lambda_o = 800$ *nm and linear positive chirp* $\alpha = 10^{-2}$ fs^{-2}. *The red components (lower frequencies, left side) travel faster than the blue ones (higher frequencies, right side). The total phase* $\Phi(t) = \alpha t^2 + \omega_o t$ *and the instantaneous frequency* $\omega(t) = d_t\Phi(t)$ *have been added. However, when experimental pulse measurements are made, the intensity* $|E(t)|^2$ *is plotted together with the spectral phase* $\Phi_s(t) = \alpha t^2$.

causing a slower propagation than in vacuum. The first expansion term $d_\omega k(\omega_o)$ is therefore responsible for slowing down the pulse and *does not destroy* its properties. The second order term

$$d_\omega^2 k(\omega_o) = d_\omega \left[\frac{1}{v_g(\omega)}\right](\omega_o) = \left[\frac{\lambda^3}{2\pi c^2}\, d_\lambda^2 n\right](\lambda_o) \tag{2.4.40}$$

is called the *Group Velocity Dispersion* (GVD) and has the effect of increasing the pulse duration[g] [25]. If $\overline{\Delta t}_{in}$ and $\overline{\Delta t}_{out}$ are the pulse duration before and after traveling through a medium of length x then from eq. 2.2.24 and eq. 2.4.35

$$\overline{\Delta t}_{out} = \sqrt{1 + \frac{4x^2[d_\omega^2 k(\omega_o)]^2}{\sigma^2}}\,\overline{\Delta t}_{in} \tag{2.4.41}$$

meaning $\overline{\Delta t}_{in} \leq \overline{\Delta t}_{out}$.

The instantaneous frequency is calculated from the total time derivative of the pulse phase in eq. 2.4.35

$$\omega(t) = d_t\Phi(t) = \omega_o + \frac{4x d_\omega^2 k(\omega_o)}{\sigma^2 + 4x^2[d_\omega^2 k(\omega_o)]^2} \cdot t \tag{2.4.42}$$

and shows that a FTL Gaussian pulse acquires a linear chirp during transmission through a transparent material. Normal dispersion ($d_\omega^2 k > 0$) leads to an increase in time of the instantaneous

---

[g] Sometimes $d_\omega^2 k$ is called the GVD *parameter*, proportional with the quantity $d_\lambda v_g$ referred as the GVD [24].

frequency $\omega(t)$, an effect called *positive chirp* (fig. 2.4). The lower frequencies arrive earlier meaning that the red part of the pulse spectrum travels faster than the blue part. The group velocity dispersion of an optical component can be compensated by another element with opposite GVD because linear dispersion is *additive.* Moreover, the chirp induced by an optical component can be pre-compensated by an earlier component. The third and higher order expansion terms of $k(\omega)$ destroy both the pulse duration and shape, generating the so-called *side wings.*

2.5 Group Velocity Dispersion Control

Towards the femtosecond regime the GVD starts to play a very important role in the pulse propagation. Even in a typical Ti:sapphire oscillator the duration of 100 fs pulse would double after one round trip through the cavity. Therefore it is imperative that this time-broadening effect is compensated for if one wants undistorted short pulses. Most of the common optical components have positive GVD which means that the lower frequencies travel faster than the higher ones. Hence, one has to add in the optical path elements with negative GVD, in which lower frequencies are retarded in order to preserve the initial temporal pulse shape.

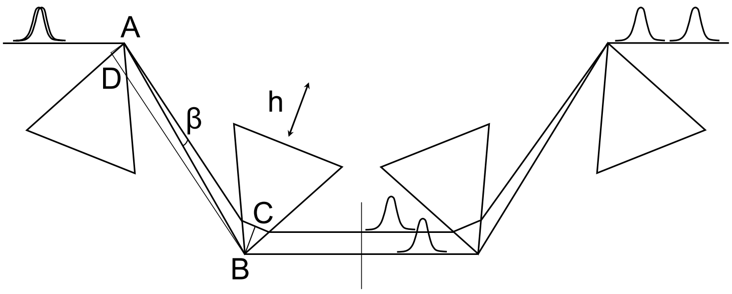

Figure 2.5: *Prism Compressor setup.*

It is well known that laser beams with different wavelengths are refracted with different angles while passing through an optical interface. This effect is called *angular dispersion* and has the interesting property of introducing GVD. The idea of using optical devices based on angular dispersion for continuous GVD tuning was first implemented for compression of chirped pulses with diffraction gratings [46]. The concept was later generalized to prisms and prism sequences [47].

The equation 2.4.41 provides the increase in time duration of a pulse that passes through a dispersive material of length x. Obviously the time duration of the pulse is always the smallest before it starts propagating through a given medium, as the GVD squared term $[d^2_\omega k(\omega_o)]^2 \geq 0$. In the case of a setup which has both positive and negative GVD components the dispersion adds up and one can annihilate the positive effects. However, the minimum pulse duration at the output is the one at the input, while the minimum total squared GVD possible is 0.

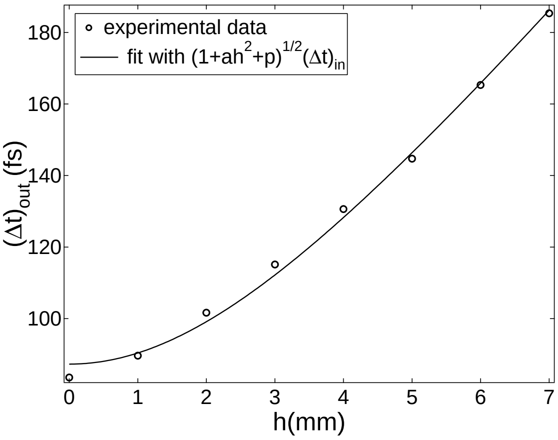

Figure 2.6: *Changing the amount of the prism material traversed by a blue laser pulse ($\lambda_o = 400nm$) one can induce a temporal broadening at the end of the whole optical setup.*

Probably the most widely used compressor, *i.e.* a device with negative GVD, is the *Prism Compressor* [48] shown in fig. 2.5. The prisms are all identical and cut in such way that for a specific wavelength the incident and exit angles are *Brewster angles* [17]. In this way the pulse travels through the prisms with minimum intensity loss. For normal dispersion material, the lower frequencies of the pulse (*'red'* part) are refracted less than the higher ones (*'blue'* part), meaning that the leading edge is delayed (has smaller group velocity $d_k\omega$) with respect to the trailing edge, yielding negative chirp [23, 24, 49]. The reason for this is that the wave fronts (*i.e.* surfaces of constant phase) of different frequency components are no longer parallel after the refraction. If the main direction is taken as the one followed by the blue part of the pulse (AB) then the wave vector will depend on the cosine of the respective frequency angle $k(\omega) = \frac{\omega}{c}\cos\beta(\omega)$. Also, the setup is built symmetrical so that the side frequencies spatially separated by the first prism pair (with an angle β) are recombined after the second pair. Considering the blue part of the spectrum traveling exactly over the tips of the first two prisms ($(AB) = l$) one can calculate the GVD induced in the pulse by the spatial decomposition

$$\mathrm{GVD}_{\mathrm{ang}}(\omega_o) = d_\omega^2 k(\omega_o) = -\left[\frac{2\lambda^3}{\pi c^2}(d_\lambda n)^2\right](\lambda_o) \tag{2.5.43}$$

where ω_o is the pulse central frequency and n is the refractive index of the prism material. The effect of the angular dispersion, $(d_\omega\beta)^2$, is considered twice as there are two pairs of prisms and the GVD is additive. Obviously, the quantity above is always negative, independent of the sign of $d_\lambda n$. As the GVD is linear in $d_\lambda v_g$ (eq. 2.4.37), results that the group velocity decreases with the increasing wavelength inside the pulse[h].

---

[h] It is interesting to notice that the optical path length (AC) of the red part of the spectrum is actually shorter

Nevertheless the laser beam has a certain thickness so it must pass through some prism material which induces a normal positive $\mathrm{GVD}_{\mathrm{mat}}$ (eq. 2.4.40). If h is the effective beam path in the prisms then eq. 2.4.41 becomes

$$\overline{\Delta t}_{out} = \sqrt{1 + \frac{4}{\sigma^2}[d^2_\omega \Phi^s_{tot}(\omega_o)]^2}\,\overline{\Delta t}_{in} \tag{2.5.44}$$

with the spectral phase GVD

$$\begin{aligned} d^2_\omega \Phi^s_{tot}(\omega_o) &= l \cdot \mathrm{GVD}_{\mathrm{ang}}(\omega_o) + h \cdot \mathrm{GVD}_{\mathrm{mat}}(\omega_o) + x \cdot \mathrm{GVD}_{\mathrm{rest}}(\omega_o) = \\ -l &\left[\frac{2\lambda^3}{\pi c^2}(d_\lambda n)^2\right](\lambda_o) + h\left[\frac{\lambda^3}{2\pi c^2}\, d^2_\lambda n\right](\lambda_o) + x \cdot \widetilde{\mathrm{GVD}}_{\mathrm{rest}}(\lambda_o) \end{aligned} \tag{2.5.45}$$

One usually replaces the second prism pair with a mirror which is just sending back the spatially broadened beam. Moreover, in the remaining configuration, the prisms are mounted on translation stages so that l and h can be varied. In this way the prism compressor spectral phase GVD can be adjusted to match the condition $d^2_\omega \Phi^s_{tot}(\omega_o) = 0$ in order to maintain the pulse to it's initial duration. As an example, we used a prism compressor with $l = 61.5$ cm in order to pre-compress a blue ($\lambda_o \simeq 400$ nm) pulse with an initial length of roughly 83 fs (fig. 2.6).

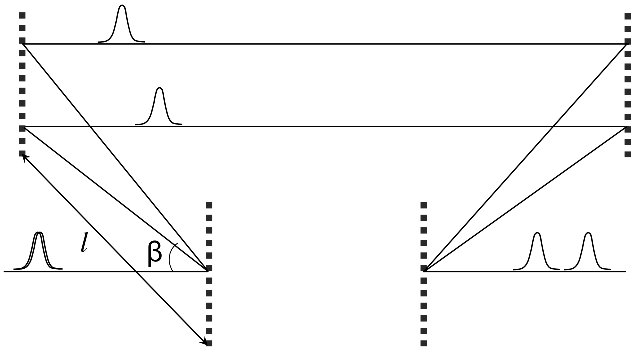

Figure 2.7: *Grating Compressor.*

The compression obtained with a prism setup is rather small. In order to generate larger negative dispersions one uses a more expensive configuration, the *Grating Compressor* (fig. 2.7). It consists of two pairs of parallel gratings which spatially resolve the frequency components, therefore inducing the desired negative GVD. As opposed to the prism compressor, the red part of the pulse is diffracted more than the blue part so it has a bigger optical path which adds up a larger negative dispersion. While in the first pair of gratings the pulse colors are separated in space, they are recombined in the

---

than the one of the blue part (AB). GVD, however, is negative due to the $\cos\beta$ dependence of the wave vector (in fact the optical path, using the *Fermat principle* [17], is $(BD) = (AC) = (AB)\cos\beta$ so the spectral phase GVD becomes $d^2_\omega \Phi^s_{ang} = l d^2_\omega[\frac{\omega}{c}\cos\beta]$).

second pair. The disadvantage of such a setup is the power loss in the order of 40-50%, depending on the chosen diffraction order. It can be shown [23, 24, 49] that the spectral phase GVD is

$$d_{\omega}^{2}\Phi_{gr}^{s} = -l\,\frac{\lambda^{3}}{\pi c^{2} d^{2} (\cos\beta)^{3}} \tag{2.5.46}$$

where l is the distance between the first pair of gratings, d the grating constant and β the diffraction angle. The double GVD provided by the two grating pairs has also been taken in account.

There are also important applications where pulses need to be stretched instead of compressed (when amplified, for example). The increase of time duration is usually made in a controlled way in *prism stretchers* or *grating stretchers* which provide positive GVD. These configurations follow the setups in the two compressors described above with the optical components placed no longer parallel but orthogonal on each other. Using grating stretchers in the commercial amplifier systems brings certain advantages: the intensity of the pulses is already reduced considerably before they reach the amplifier and the stretching is made in a controlled way (therefore reversible by a similar setup with a grating compressor).

2.6 The Laser System

Our system consists of a commercial Coherent MIRA Ti:sapphire oscillator which outputs pulses with a spectral width $\overline{\Delta\lambda} \simeq 35$ nm, at central wavelength $\lambda_o = 800$ nm, and time-width of about 55 fs. The oscillator is pumped by a VERDI 5 W diode-pumped Nd:Vanadate solid state laser (CW-laser at 532 nm) [50]. The maximum power obtained is roughly 500 mW at a repetition rate of 80 MHz, meaning $\simeq 6$ nJ/pulse. The output pulses can be amplified to powers over 1 W at repetition rates between 100 and 250 kHz ($\simeq 4$ μJ/pulse at 250 kHz) by a *Regenerative Amplifier* (RegA 9050 [50]) Ti:sapphire pumped by a VERDI 10 W (CW-laser at 532 nm). A requirement of the amplification process is that the oscillator pulses need first to pass through a grating stretcher in order to increase their time duration. After the RegA system they are compressed to $\overline{\Delta t} \simeq 64$ fs by a grating compressor which reverses the effects of the stretcher. We have also the possibility of generating pulses with a different central wavelength by using an *Optical Parametric Amplifier* (OPA [50]) which efficiently converts the initial $\lambda_o = 800$ nm pulses to any wavelength in the range from 450 to 750 nm (the OPA signal) and near-infrared (IR) from 940 to 2400 nm (the OPA idler).

Chapter 3

Pulse Measurement. Autocorrelation

3.1 Pump-Probe Experiments

In order to measure the duration of a very short event one needs an even shorter one to probe it. But then, of course, the question of how to measure the shortest event possible arises. Most of the atomic processes (vibrations, rotations, electronic excitations, etc.) occur in pico to femtoseconds, beyond the reach of the fastest electronic detectors. With the discovery of the ultrashort laser pulses the scientists gained a very powerful tool for measurements of ultrafast phenomena: the *Pump-Probe Technique*, *i.e.* one pulse sets in motion some process and a second one probes it after a given delay.

In the upper part of figure 3.1 the actual setup of a pump-probe experiment is depicted. An initial laser pulse is separated into two twin pulses by a beam-splitter. The resulting pulses travel afterwards along two different paths. One of them is called the pump pulse and is shot directly on the sample inducing a transient excitation while the second one is going over a delay stage and reads it. The sample arrival time between the pump and the probe pulse is varied by the delay stage which increases or decreases the probe path.

The pump pulse is usually a laser pulse while the probe pulse can be also laser (then probing the transient electronic density of states, like in a two-photon photoemission (2PPE) experiment [4], or the optical properties, like reflectivity [51]), it can be an electron pulse (probing the surface or the bulk structural modifications, depending on its energy [6, 14, 52]) or it can be X-rays (then probing the bulk modifications or even the atomic core-level dynamics [2, 53]).

One needs a fully reversible process induced by the pump pulse in such way that the probe pulse finds always the same amount of excitation for a given position of the delay stage. However, if the excitation is too strong and the process can not be reversed one can actually simulate the reversibility by changing the position of the sample after every pump hit. In this way the pulses find always the same initial conditions, under the assumption that the sample has the same properties in all spatial directions [6, 52].

In the lower part of the figure 3.1 is given a hypothetical curve that the detector may read from the probe pulses, where the *time zero* is given by a *specific position* of the delay stage for which the probe and the pump pulses arrive in the *same instance* on the sample. The time axis represents

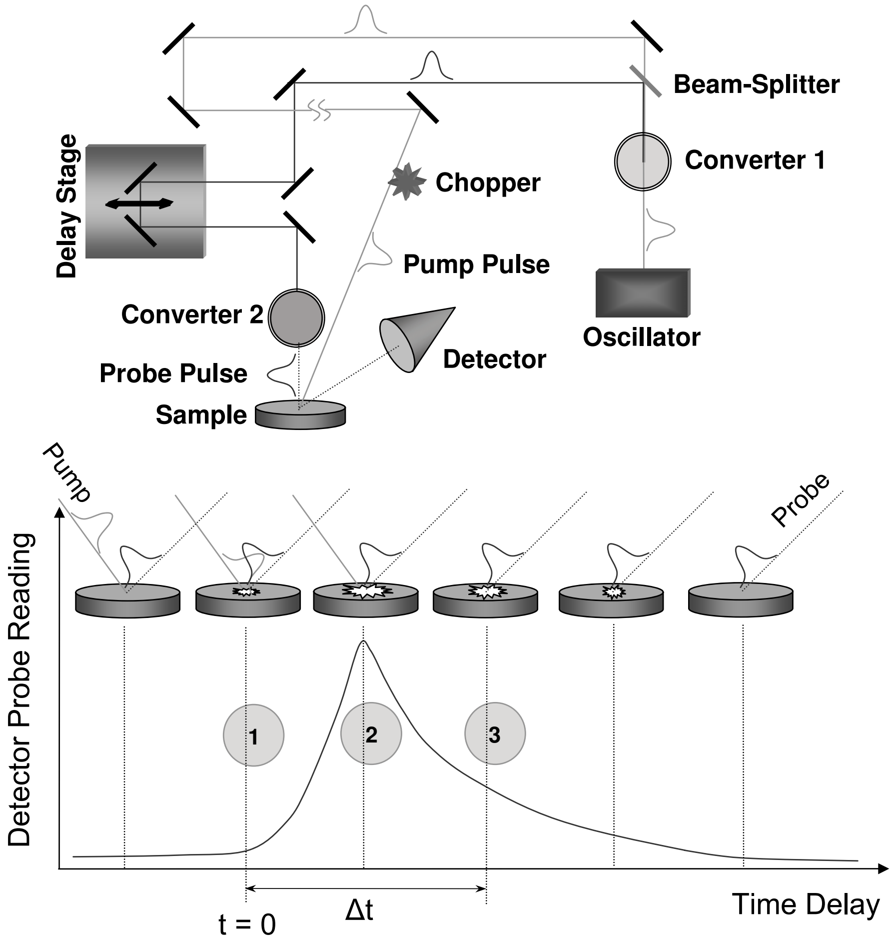

Figure 3.1: ***Upper part:*** *pump-probe experiment setup. The pump and probe pulses are generated from the same initial pulse. The delay stage varies the relative arrival time of the two pulses on the sample while the chopper allows the data to be normalized for laser power fluctuations. The converters transform the laser pulse into another type of pulse (laser, electron, etc.).* ***Lower part:*** *the principle. 1. The two pulses arrive in the same time on the sample and the transient excitation starts. 2. The pump pulse is absorbed completely. 3. The system evolves back towards equilibrium.*

the sample relative arrival time of the probe pulses with respect to the pump pulses[a]. The idea is to trigger the same transient excitation for many times and then take *'snapshots'* of it at certain times along its evolution. *One point of this curve is a statistical integration over a macroscopic time of the same situation in the excitation evolution.* In other words, the reversible process is induced repeatedly by the pump pulse while the probe pulse takes many *'photos'* of it at a certain time in its development. These *'snapshots'* are then *averaged* by the detector and when the data are satisfactory the delay stage changes the probe delay and the acquisition restarts.

---

[a] which translates into different positions of the delay stage.

While in principle this experiment seems simple, in reality the things are much more complicated. One has to consider various problems like finding the temporal and spatial overlap of the two pulses, fluctuations or even sample aging. Most of the laser flux stability issues are dealt with by normalizing the pump-probe data with the data taken almost simultaneously without the pump beam (chopping).

3.2 Second Harmonic Generation

When light emerges from low intensity sources[b] its interaction with matter is considered to be linear. In classical electrodynamics the light propagates through a medium by continuously inducing coherent absorption and emission from harmonic electronic dipoles. However, if the excitation intensity is high enough these oscillations become strongly anharmonic. Therefore the emitting dipoles can radiate energy at frequencies which are integer multiples of the original frequency [25]. The quantity which describes the response of a material to an electromagnetic excitation is called polarization and is a function of the interacting electric field

$$\mathbf{P} = \varepsilon_o \chi^{(1)} \mathbf{E} + \varepsilon_o \chi^{(2)} \mathbf{E}^2 + \varepsilon_o \chi^{(3)} \mathbf{E}^3 + ... \qquad (3.2.1)$$

The proportionality constants $\chi^{(m)} = \varepsilon^{(m)} - \varepsilon_o = (n^2)^{(m)} - 1$ are called susceptibilities of m order and they are represented by tensors of order[c] $(m+1)$ ($\varepsilon^{(m)}$ is the dielectric tensor). In this expansion the first term describes the linear optics while the others account for nonlinear optical effects. In the dipole approximation of the electron-photon interaction the second order susceptibility is a third order tensor which has components corresponding to the various possible orientations of the crystal axis and of light polarization. The second order nonlinearity $P_i^{(2)} = \varepsilon_o \chi_{ijk}^{(2)} E_j E_k$ is responsible for *second harmonic generation* (*i.e.* the input frequency is doubled by the nonlinear medium) [54], for sum and difference frequency generation and for parametric amplification and oscillation. In the particular case of a material with a structural inversion center this tensor vanishes [55]. Thus no second harmonic can be generated[d]. However, all crystals, liquids and gases can display third order optical nonlinearities, responsible for the *Optical* and *Electro-Optical Kerr Effect* [55].

In an anisotropic medium the phase velocity of light depends on both wave polarization and direction of propagation. Due to the anisotropy the polarization state of a plane wave may vary as it propagates through the medium. However, it can be shown that for a given direction of propagation, $\mathbf{n}$, in the medium, there exist two eigenwaves with well defined eigen-phase velocities and polarization directions such that a light wave with polarization parallel to one of these directions will remain in the same polarization state while it propagates through the anisotropic medium. The wavefront will be represented by a three-dimensional surface in $\mathbf{k}$ space (momentum space) which is known as the *normal surface* (also referred to as the *Fresnel's Equation*) and follows naturally from the electric field wave equation for the medium. This surface consists of two shells which,

---

[b] *i.e.* regular sources like a light bulb, light diodes, the sun

[c] in the assumption that the magnetic permeability of the medium can be approximated by the one in the vacuum ($\mu \simeq \mu_o$). $(n^2)^{(m)}$ and ε_o are the squared refractive index tensor and the vacuum dielectric constant respectively.

[d] Lack of inversion symmetry is also the prerequisite for linear electro-optic effect and piezoelectricity.

in general, have four points in common. The two lines that connect the origin and these points are known as the *Optical Axes.* Along **n**, the two independent plane-waves (orthogonal linearly polarized propagation modes) have phase velocities $\pm c/n_1$ and $\pm c/n_2$, where n_1^2 and n_2^2 are the two solutions of the Fresnel's equation [55]. In the direction of the optical axes the wave can only have one phase velocity following the unique solution k of the Fresnel's equation. However, it has two independent polarization directions. With respect to the incident wave, the dielectric response of the medium is given by the electric *displacement vector* $\mathbf{D} = \varepsilon \mathbf{E}$ which relates to the stored electromagnetic energy density by $U_{el} = \frac{1}{2}(\varepsilon^{-1})_{ij} D_i D_j$ (in the assumption that the first order dielectric tensor $\varepsilon^{(1)}$ is enough to describe the wave-medium interaction). When considering the constant energy density surfaces U_{el} in the **D** space, the latter equation leads to the *index ellipsoid* (or *optical indicatrix*)

$$\frac{x^2}{n_x^2} + \frac{y^2}{n_y^2} + \frac{z^2}{n_z^2} = 1 \tag{3.2.2}$$

where $\mathbf{r} = \mathbf{D}/\sqrt{2U_{el}}$ is the direction of the displacement vector and the principal indices of refraction n_i $(i = x, y, z)$ are related to the principal dielectric constants[e] ε_i by $n_i^2 \equiv \varepsilon_i/\varepsilon_o$. The equation 3.2.2 is used mainly to find the two indices of refraction and the two corresponding directions of **D** associated with the two independent plane waves that can propagate along the arbitrary direction **n** in the medium. In general, the three principal indices n_x, n_y, n_z are all different and thus there are two optical axes. The crystal is said then to be *biaxial*[f]. However, many optical materials have two main indices equal, in which case the normal surface consists of a sphere and an ellipsoid of revolution that intersect in two points along the z axis. Therefore the z axis becomes the *only* optical axis and the crystal is called *uniaxial*[g]. When all the main indices are equal the two sheets of the normal surface degenerate into a single sphere and the crystal becomes optically isotropic (in the cubic system, as example). In uniaxial crystals the plane containing the wave vector **k** of the incident light and the optical axis z is termed the *principal plane.* The light beam whose polarization is normal to the principal plane is called an *ordinary beam* or an *o-beam* whereas a beam with polarization in the principal plane is known as an *extraordinary beam* or *e-beam.* The refractive index of the o-beam does not depend on the propagation direction while for the e-beam it does. As a definition, the refractive indices of the ordinary and extraordinary beams in the plane normal to the z axis are the *principal values* of the refractive index and are denoted by n_o and n_e. In general, the refractive index of the e-beam depends on the polar angle θ between the z axis and the vector **k**, following the ellipse equation $n_e(\theta) = n_o\{(1+\tan^2\theta)/[1+(n_o/n_e)^2\tan^2\theta]\}^{1/2}$ (fig. 3.2). The crystal is called *negative* if $n_o > n_e$ and *positive* if $n_o < n_e$. When an arbitrary linear polarized laser beam passes through an uniaxial crystal it is divided into two orthogonally polarized beams (o- and e-beam) which propagate along two different directions. The o-beam will preserve the initial beam propagation direction, **k**, whereas the e-beam direction will make an angle θ_c (the *birefringence* or *walk-off angle*) with respect to **k**.

---

[e] the first order dielectric tensor $\varepsilon^{(1)} = (\varepsilon)_{ij}$ is a 3×3 diagonal matrix with $\varepsilon_i \equiv \varepsilon_{ii}$

[f] the corresponding crystal systems are triclinic, monoclinic and orthorhombic

[g] the corresponding crystal systems are tetragonal, hexagonal and trigonal

The first nonlinear optical effect observed after the lasers became available was the second-harmonic generation (SHG) [54]. When a laser beam, with central frequency ω, passes through a noncentrosymmetric crystal some pairs of the incoming photons are replaced by single photons with twice the initial frequency 2ω. Generally, the energy and momentum conservation in such mixing process read

$$\begin{aligned} \omega_1 + \omega_2 &= \omega_3 \\ \mathbf{k}_1 + \mathbf{k}_2 &= \mathbf{k}_3 \end{aligned} \tag{3.2.3}$$

where the indices '1' and '2' refer to the initial photons while '3' refers to the resulting photon. Since in the case of SHG the mixed photons have the same frequency and direction ($\omega_1 = \omega_2 \equiv \omega$ and $k_1 = k_2 \equiv k(\omega)$), the above equation leads to $2\omega = \omega_3$ and $2k(\omega) = k_3 \equiv k(2\omega)$. The momentum conservation relation is also known as the *phase-matching condition* and for the SHG it is yielding the refractive index equality $n(\omega) = n(2\omega)$. There are two different phase-matching types (I and II) in uniaxial crystals, provided by the different polarizations that can be used in the mixing process. If the mixing waves have the same polarization then the sum frequency (SF) radiation will be polarized in the orthogonal direction. This case is called type I phase matching[h]. If the mixing waves have different polarizations then one can speak about the type II phase matching. In the type $\mathrm{I}^{(-)}$ phase matching SHG, the angle θ that the incoming mixed waves must have with respect to the optical axis z in order to be efficiently converted can be calculated by putting the condition that $n_e(2\omega, \theta) = n_o(\omega)$, for which the dephasing quantity $\Delta k = k(2\omega) - 2k(\omega)$ is zero (fig. 3.2).

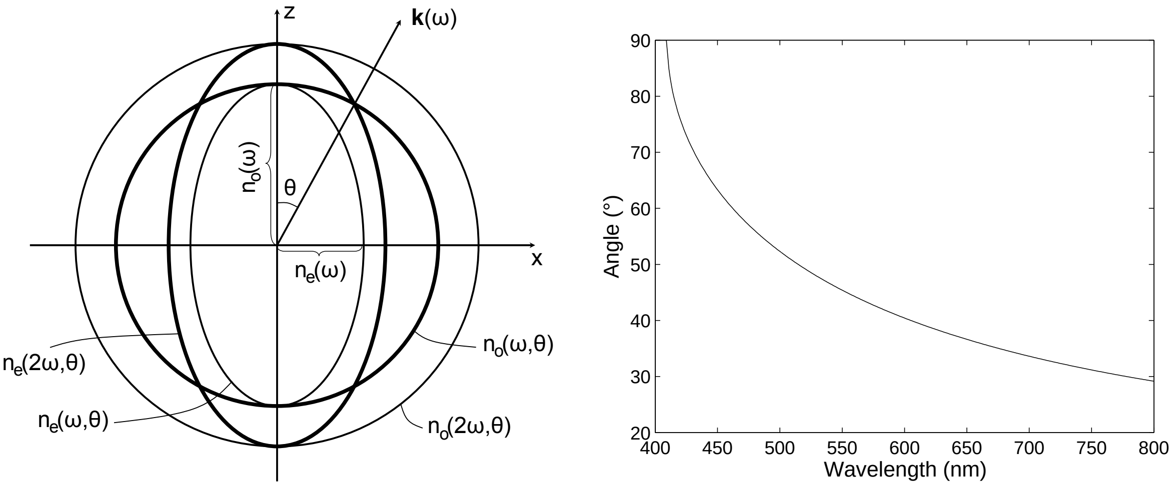

Figure 3.2: ***Left Graph**: Graphical representation of the type I phase matching condition for a negative uniaxial crystal with the optical axis along z. **Right Graph**: Calculated type* $I^{(-)}$ *phase matching angle for different wavelengths in a β-BBO crystal.*

---

[h] In negative crystals the mixed waves are o-beams (type $\mathrm{I}^{(-)}$ or 'ooe' phase matching), $\mathbf{k}_1^o + \mathbf{k}_2^o = \mathbf{k}_3^e(\theta)$, and in positive crystals they are e-beams (type $\mathrm{I}^{(+)}$ or 'eeo'), $\mathbf{k}_1^e + \mathbf{k}_2^e = \mathbf{k}_3^o(\theta)$.

The result can be written as

$$\sin^2\theta = \frac{[n_o(\omega)]^{-2} - [n_o(2\omega)]^{-2}}{[n_e(2\omega)]^{-2} - [n_o(2\omega)]^{-2}} \tag{3.2.4}$$

In the ideal case of a plane wave the intensity of the generated second harmonic is proportional to the squared intensity of the initial wave, $I^2(\omega)$, and depends also on the traversed length of the material L [25, 55, 56]:

$$I(2\omega) \propto I^2(\omega)\left[\frac{\sin(\frac{\Delta kL}{2})}{\frac{\Delta kL}{2}}\right]^2 \tag{3.2.5}$$

The real frequency converters have to deal with non-ideal situations: the incoming radiation is not a plane wave (it is divergent), the pulse is not monochromatic and the crystal temperature is unstable. Therefore, in estimating the efficiency of a converter one must consider the angular $\Delta\theta$, spectral $\Delta\nu$ and temperature ΔT bandwidths which are related to the maximum permissive divergence, spectral width of the convertible radiation and temperature variation of the crystal. These effects induce a non-zero dephasing during propagation in the crystal, meaning that $\Delta k \neq 0$. In the first order approximation $\Delta k \simeq \Delta k(\mathbf{0}) + (\partial_T\Delta k)\Delta T + (\partial_\theta\Delta k)\Delta\theta + (\partial_\nu\Delta k)\Delta\nu$, where $\Delta k(\mathbf{0}) = 0$ is the mismatch for the exact phase matching. By looking at the equation 3.2.5 one can observe that the power of the resulting radiation is halved if the mismatch is $\Delta k \simeq 0.886\,\pi/L$. When the group velocity of the mixing wave, v_{g1}, is equal with the group velocity of the resulting wave, v_{g2}, the *group velocity matching* (or *quasi-static regime*) takes place. In this case a Gaussian laser pulse will transform into a Gaussian SHG pulse. It can be shown that the time width of the initial pulse, $\overline{\Delta t}_1$, is almost equal with the time width of the SHG pulse, $\overline{\Delta t}_2$, at high conversion efficiencies and $\overline{\Delta t}_2 = \overline{\Delta t}_1/\sqrt{2}$ at low ones [45]. When $v_{g1} \neq v_{g2}$ the *group-velocity mismatch* (or *unsteady regime*) takes place. In this case the *inverse group velocity mismatch*, GVM$= |v_{g2}^{-1} - v_{g1}^{-1}|$ must be considered. The quantity $L_{qs} = (\mathrm{GVM}\,\overline{\Delta\omega}_1)^{-1}$ is called the *quasi-static length*[i] and characterizes

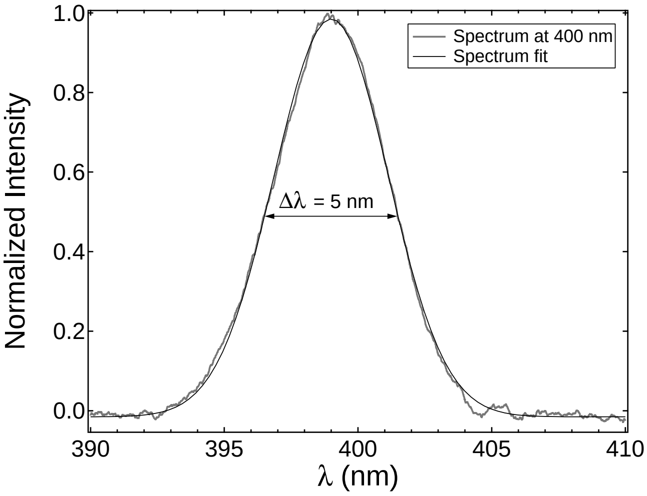

Figure 3.3: *The measured spectrum of the SHG pulses with central wavelength at 399 nm.*

---

[i] $\overline{\Delta\omega}_1$ is the spectral bandwidth of the initial pulse

the real length where the GVM can be ignored. If $L < L_{qs}$ then the crystal can be considered as in the quasi-static regime. A special case arises for $L_{qs} \ll L$ when the spectral width of the SHG pulse is lower than the one of the fundamental. This process is accompanied by strong temporal spreading of the SHG pulse, following $\overline{\Delta t_2} \approx \mathrm{GVM}\, L$ which is practically independent on $\overline{\Delta t_1}$. It can be also shown that the SHG spectrum has a maximum at $\omega_{max} = 2\omega_1 - \mathrm{GVM}^{-1}\Delta k$ and its spectral width is given by $\overline{\Delta\omega_2} = 2\pi(\mathrm{GVM}\, L)^{-1}$ [45]. The spectral bandwidth of the crystal, $\overline{\Delta E_{cr}}$, is represented by the possible spectral bandwidth of the SHG pulse which can by induced during the propagation of the fundamental for $L_{qs} \ll L$. In other words $\overline{\Delta E_{cr}} = 2\pi\hbar(\mathrm{GVM}\, L)^{-1}$. Comparing with the quasi-static regime conditions it can be stated that a noncentrosymmetric crystal has the potential to preserve the fundamental pulse time duration if $\overline{\Delta E_{cr}} > \hbar\overline{\Delta\omega_1}$.

As an example, we used a $L = 0.5$ mm wide β-BBO crystal as SHG medium in order to double a $\lambda_1 = 798$ nm fundamental 'red' pulse with $\overline{\Delta\lambda_1} = 26$ nm into a $\lambda_2 = 399$ nm 'blue' pulse. As mentioned before, the BBO bandwidth can be calculated knowing that the GVM for the 'ooe' phase matching at 800 nm is 194 fs/mm [45], yielding a value of 43 meV which is lower than the bandwidth of the fundamental $\simeq$ 51 meV (eq. 3.4.31). The quasi-static length reads $L_{qs} \simeq 0.06$ mm which is much less than the crystal length L. The spectrum for the SHG pulse was measured with a spectrometer and the value obtained was about 5 nm which lead to a bandwidth of 39 meV (fig. 3.3), relatively close to the BBO bandwidth. The 'blue' pulse time-width was also calculated to be between 47 and 97 fs by making use of the equations 3.3.6 and 3.4.31).

3.3 Ultrashort Pulse Measurement

The most important property of a laser pulse is its shape and in particular its temporal width. As discussed before, a very short event can be probed by a shorter or at least comparable one. Therefore, at the femtosecond time scale the only thing capable of measuring the pulse properties *is* the pulse *itself* [57]. For a start, using the uncertainty principle (eq. 2.2.22), one can estimate the lower limit for the duration of a pulse from its spectral width $\overline{\Delta\lambda}$ (taken, for example with a *Czerny-Turner* type spectrometer [22]). In fact, assuming that the pulse is FTL one can determine its shape in the time domain from the spectral intensity $I(\lambda)$ (or $I(\omega)$) and further, using eq. 2.2.28, 2.2.29,

$$\overline{\Delta t} \geq \frac{K}{c}\frac{\lambda_o^2}{\overline{\Delta\lambda}} \tag{3.3.6}$$

with $K = 0.441$ for Gaussian pulses or $K = 0.315$ for sech-type, estimating a duration of 27 or 19 fs respectively[j]. However, any phase information is lost and a chirped pulse can not be distinguished from a FTL pulse. This is actually the so-called *one-dimensional phase-retrieval problem* [22] which is *unsolvable.*

In the time domain, one could think of a *Michelson interferometer* (fig. 3.4) to correlate a laser pulse with itself. Two identical pulses resulting from an initial one (with the help of a beam-splitter) are spatially and temporally overlapped, one of them being variably delayed with respect to the

---

[j] In our case $\overline{\Delta\lambda} \simeq 35$ nm at $\lambda_o = 800$ nm.

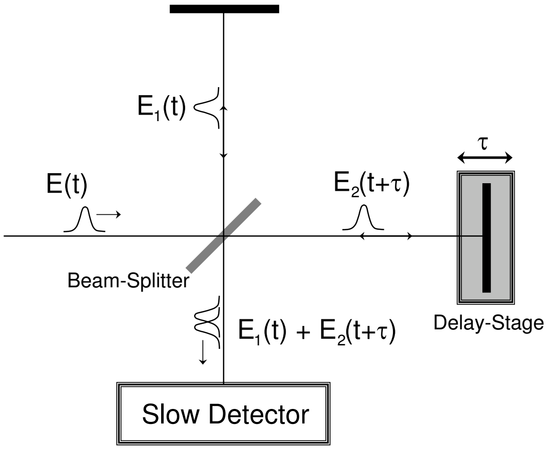

Figure 3.4: *Michelson Interferometer.*

other. The *slow detector* will record a signal averaged in time and proportional with the squared amplitude of the electric field detected [22, 23, 58]:

$$S^{(1)}(\tau) = \int_{-\infty}^{\infty} dt\, |E(t) + E(t+\tau)|^2 = \int_{-\infty}^{\infty} dt \Big\{ |E(t)|^2 + |E(t+\tau)|^2 + 2\mathrm{Re}[E(t)E^*(t+\tau)] \Big\} \quad (3.3.7)$$

which is usually called *First Order Autocorrelation* or *Field Autocorrelation* (or simply the *Interferogram*) due to its dependency on the *Autocorrelation* of the first order electric field of the pulse

$$S^{(1)}(\tau) \sim \int_{-\infty}^{\infty} dt\, E(t)E^*(t+\tau) \quad (3.3.8)$$

as the first two integral terms are just the *off-coincidence* offset. The Fourier transform of this *coincidence* term is actually the spectrum, a result known as the *Autocorrelation Theorem*

$$|E(\omega)|^2 = \frac{1}{2\pi} \int_{-\infty}^{\infty} d\tau\, e^{-i\omega\tau} \int_{-\infty}^{\infty} dt\, E(t)E^*(t+\tau) \quad (3.3.9)$$

Thus, an interferometer and a normal spectrometer yield the same information, the spectrum. Considering now the pulses in the frequency domain (expressed by their Fourier transforms, eq. 2.2.15) the interferogram becomes

$$S^{(1)}(\tau) = 2 \int_{\infty}^{\infty} d\omega\, E(\omega)E^*(\omega)(1 + \cos\omega\tau) \quad (3.3.10)$$

meaning that it depends only on the spectrum $|E(\omega)|^2$ which gives no information about the phase. From the interferogram one can extract the *coherence time* Δt_{coh} which is equal with the actual pulse duration $\overline{\Delta t}$ only in the case of a perfectly FTL pulse. As a general remark it can be stated that using only linear optics (gratings, beam-splitters, etc.) one can determine the coherence length but not the duration of a laser pulse [23]. Unfortunately, having only the spectrum of a pulse leads to a humongous number of trivial (time reversal, translation, absolute phase shift) and non-trivial (the issue of the pulse finite *support*) ambiguities [22]. In other words, the number of possible pulses that can yield the same spectrum is not just infinity but a *higher-order* infinity.

However, the interferogram of two different pulses is far from a regular one. For example, let us suppose two linearly-chirped Gaussian pulses (used therefore only with linear optics for which the dispersion is up to the second order),

$$E_{1,2}(t) = E_{o1,o2} \exp\left\{-\frac{t^2}{\sigma_{1,2}} + i\omega_{o1,o2}t + ia_{1,2}t^2\right\} \tag{3.3.11}$$

with real amplitudes E_{o1} and E_{o2} (the phase information is already condensed in the exponential), that are interfered collinearly in a slow detector. Performing the integral in eq. 3.3.7 one can write the normalized interferogram as

$$S^{(1)}(\tau) = 1 + \mathrm{Re}\left\{B \cdot \exp\left[-\tfrac{(\tau-\tau_o)^2}{A} - i\omega(\tau)\tau\right]\right\} \simeq 1 + \mathrm{Re}(B)\exp\left[-\tfrac{(\tau-\tau_o)^2}{A}\right]\cos\left[\omega(\tau)\tau\right] \tag{3.3.12}$$

where $B(\sigma_{1,2}, a_{1,2}, \omega_{1,2})$ is some complex constant ($\mathrm{Im}(B) \simeq 0$ for $a_1 \simeq a_2$ and $\omega_1 \simeq \omega_2$) and the envelope of the interferogram is *advanced* or *retarded* (depending on the sign of $\tau_o \propto (\omega_1 - \omega_2)$) with respect to the interfered pulses. The most important quantities are

$$A(\sigma_{1,2}, a_{1,2}) = \frac{(\sigma_1+\sigma_2)^2 + \sigma_1^2\sigma_2^2(a_1-a_2)^2}{\sigma_1+\sigma_2+\sigma_1\sigma_2(a_1^2\sigma_1+a_2^2\sigma_2)} \ , \tag{3.3.13}$$

which gives the width of the interferogram, and the linear chirped frequency $\omega(\tau) = \alpha(\sigma_{1,2}, a_{1,2}) \cdot \tau + \omega_o(\sigma_{1,2}, a_{1,2}, \omega_{1,2})$ with the chirp parameter

$$\alpha(\sigma_{1,2}, a_{1,2}) = \frac{\sigma_1^2(a_2-a_1)\left[1-a_1a_2\sigma_2^2\right] + a_2\left(\sigma_2^2-\sigma_1^2\right)}{(\sigma_1+\sigma_2)^2+\sigma_1^2\sigma_2^2(a_1-a_2)^2} \tag{3.3.14}$$

and $\omega_o \simeq \omega_{1,2}$ for $\omega_1 \simeq \omega_2$. It can be shown that $A \leq \sigma_1 + \sigma_2$ which leads to the important inequality between the temporal width of the interferogram and the widths of the interfered pulses:

$$\overline{\Delta t}_{int} \leq \overline{\Delta t}_1 + \overline{\Delta t}_2 \tag{3.3.15}$$

As remarked previously, the Fourier transform of the interferogram 3.3.12 *is* the spectrum when $\omega_1 \simeq \omega_2$. The calculation provides the spectral frequency width of the form

$$\overline{\Delta\omega} = 4\sqrt{\frac{1+\alpha^2A^2}{A}\ln 2} \tag{3.3.16}$$

In the particular case of two different Gaussian pulses with no chirp

$$S^{(1)}(\tau) = 1 + B \cdot \exp\left(-\frac{\tau^2}{\sigma_1+\sigma_2}\right)\cos\left(\frac{\sigma_1\omega_1+\sigma_2\omega_2}{\sigma_1+\sigma_2}\,\tau\right) \tag{3.3.17}$$

and, obviously, interchanging the width of the two pulses ($\sigma_1 \leftrightarrow \sigma_2$) leaves the interference envelope intact. However, if the *complete* information is available (the oscillations are visible and the central frequencies of the pulses are known) then the widths can be *exactly* attributed. But this does not mean the fields are *uniquely* determined, for the simple reason that the *theoretical* interferogram depends on the way we chose the pulse shapes. It can be shown that there are still an infinite number of pulses which can reproduce the actual *experimental* interferogram.

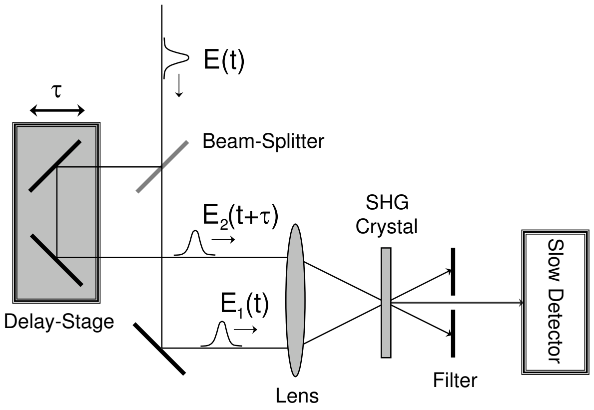

Figure 3.5: *The intensity autocorrelator experimental setup.*

The common method for *estimating* the pulse duration is the *Intensity Autocorrelator* (IAC) which *attempts* to measure the pulse intensity in time [59] by employing nonlinear optics. Two identical replicas of the initial pulse are sum-frequency mixed in a *second-harmonic-generation* (SHG) crystal [19, 45] with a variable temporal overlap (fig. 3.5). The field generated in the nonlinear crystal (for $\lambda_o \simeq 800$ nm usually *$\beta-$barium borate*, $\beta-$BaB$_2$O$_4$ or simply BBO [60]) is the product of the two pulses $E(t)E(t+\tau)$ and hence oscillates at twice the frequency of the original light $2\omega_o$. The slow detector will read the intensity of this field, averaged in time:

$$A^{(2)}(\tau) = \int_{-\infty}^{\infty} dt\ |E(t)E(t+\tau)|^2 = \int_{-\infty}^{\infty} dt\, I(t)I(t+\tau) \tag{3.3.18}$$

meaning that the SHG crystal correlates the intensity of the pulse with itself (*intensity autocorrelation* or IAC). If a Gaussian pulse shape is considered (eq. 2.2.18), the autocorrelation reads

$$A^{(2)}(\tau) = |E_o|^4 \sqrt{\frac{\pi\sigma}{4}} \exp\left(-\frac{\tau^2}{\sigma}\right) \tag{3.3.19}$$

Thus, the width of the autocorrelation function is $\sqrt{2} \simeq 1.441$ times longer than the pulse duration. For a sech-pulse the multiplication factor is 1.543.

The most obvious loss of information in an IAC is the the phase. But even though the requirements for the intensity of the pulse are far less ambitious than in the case of the field (no phase needed) the IAC does not determine intensities *uniquely.* It can be shown that there are many pulse-shapes, constructed from an initial one with the *Blaschke products*[k], which lead to *exactly* the same IAC [22]. Moreover, the pulse duration depends on its *assumed* shape as the autocorrelation is *symmetric* by definition around $\tau = 0$ regardless of the symmetry of the pulse. However, if a pulse is broadened in time, the effect will be detected by an IAC. Therefore it can be stated that an IAC reflects qualitatively the pulse duration and not the coherence length [23]. Beside the time-reversal ambiguity there are also several *approximate* ambiguities which make quite different intensities to be experimentally indistinguishable [22] (IACs are so similar that the error is less than 0.1%). As the pulse shape becomes more complex the autocorrelation becomes *simpler* and approaches the shape of a narrow *spike* on a *pedestal*, independent of the intensity structure [61]. Calculations show that the spike is a measure of the coherence length while the pedestal is giving the pulse duration.

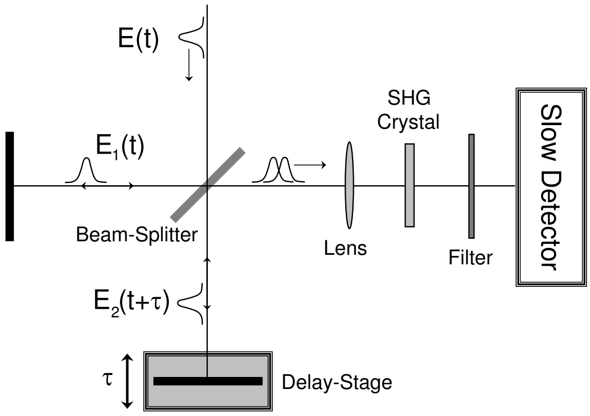

Figure 3.6: *The FRAC experimental setup.*

The combination spectrum-autocorrelation was intensively studied as people thought that the constrains they impose to each other are sufficient to provide the pulse uniquely, including the phase. Indeed, the algorithm typically used to find the phase from intensities in both domains ($I(\omega)$ and $I(t)$), called the *Gerchberg-Saxton Algorithm* [62], which involves making a guess for the phase and Fourier-transforming back and forth between the two domains with the amplitudes replaced by the measured quantities, yields an *unique* phase. Unfortunately, the IAC does *not* provide an *unique* intensity of the pulse and that is where methods like *Temporal Information Via Intensity* (TIVI) [63] fail.

The IAC of two completely different Gaussian pulses with linear chirp (eq. 3.3.11) gives simply

$$A^{(2)}(\tau) = E_{o1}^2 E_{o2}^2 \sqrt{\frac{\pi\sigma_1\sigma_2}{2(\sigma_1+\sigma_2)}} \exp\left(-\frac{2\tau^2}{\sigma_1+\sigma_2}\right) \tag{3.3.20}$$

and its width satisfies a Pythagorean-sum relationship with the durations of the two pulses

$$\overline{\Delta t}_{AC}^2 = \overline{\Delta t}_1^2 + \overline{\Delta t}_2^2 = (\sigma_1+\sigma_2)2\ln 2 \tag{3.3.21}$$

---

[k] If the spectrum intensity is multiplied with products of the form $B(\omega) = \prod_{m=1}^{N} \frac{\omega-\omega_m^*}{\omega-\omega_m}$, where ω_m's are complex numbers, then it does not change as $|B(\omega)\cdot E(\omega)|^2 \equiv |E(\omega)|^2$ (obviously $|B(\omega)|^2 = 1$ for real ω). However, the Fourier transform of the new spectrum intensity will generate an infinite number of possible temporal intensities.

showing that the pulses can not be distinguished from each other. This formula is useful for interpreting the photoelectron signals from 2PPE experiments performed on surfaces which lack unoccupied states and with different *colors*, where the pulses are large compared to an optical cycle (in visible, ~ 3 fs) (refer to chapter 4).

In 1983 J. C. Diels introduced the *Interferometric Autocorrelation* or the *Fringe-Resolved Autocorrelation* (FRAC) [64] which combines both the spectrum and autocorrelation data into one single trace. The setup adds a *thin* SHG crystal (required by the *phase-matching-bandwidth* conditions [65,66]) at the output of a Michelson interferometer and the resulting (appropriately filtered) transient field $[E(t)+E(t+\tau)]^2$ is recorded with a slow square-law detector (fig. 3.6) as function of the pulses delay τ. In general, the nonlinear-optical phase-matching bandwidth is inversely proportional to the crystal thickness, so very thin crystals are required for measurements of very short laser pulses as they have a broad spectral content. The expression for FRAC is given by [22,23]

$$S^{(2)}(\tau) = \int\limits_{-\infty}^{\infty} dt\, \left|[E(t)+E(t+\tau)]^2\right|^2 = \int\limits_{-\infty}^{\infty} dt\, \left[I^2(t)+I^2(t+\tau)\right] + 4\int\limits_{-\infty}^{\infty} dt\, I(t)I(t+\tau) +$$
$$+\, 4\int\limits_{-\infty}^{\infty} dt\, [I(t)+I(t+\tau)]\, \mathrm{Re}\,[E(t)E^*(t+\tau)] + 2\int\limits_{-\infty}^{\infty} dt\, \mathrm{Re}\left[E^2(t)E^{*2}(t+\tau)\right] \tag{3.3.22}$$

where the first term is a constant offset, the second is the intensity autocorrelation discussed above, the third is, up to a constant, the interferogram of $E(t)$ weighted with the sum of intensities and the fourth is, also up to a constant, the interferogram of the second harmonic $E^2(t)$. Usually $I(t)+I(t+\tau)$ varies far less than $E(t)$ so the third term is simply equivalent with the spectrum of the pulse. On the other hand the fourth term is equivalent with the spectrum of the second harmonic, providing *different* information.

Experimentally, when building an interferometric autocorrelator, the first thing one should check is that the maximum and the offset of the FRAC trace are in a ratio of 8:1. This works only in the case of two perfectly identical *intensive* beams, *i.e.* the correlated pulses must have the *same* amplitude. Obviously, for $\tau = 0$ (at *coincidence*) the FRAC function is at maximum, $16|E_o|^4$, while for $|\tau| \gg 0$ (at *far-off-coincidence*) the offset is $2|E_o|^4$. Employing a Gaussian pulse shape (eq. 2.2.18) the FRAC function reads (fig. 3.7)

$$S^{(2)}(\tau) = |E_o|^4\sqrt{\pi\sigma}\left[1+\exp\left(-\frac{\tau^2}{\sigma}\right)(2+\cos 2\omega\tau) + 4\exp\left(-\frac{3\tau^2}{4\sigma}\right)\cos\omega\tau\right] \tag{3.3.23}$$

The FRAC upper ($S_+^{(2)}(\tau)$) and lower ($S_-^{(2)}(\tau)$) envelopes are given, respectively, by the constructive and destructive interference of the two pulses at a given delay τ

$$S_\pm^{(2)}(\tau) = |E_o|^4\sqrt{\pi\sigma}\left[1+3\exp\left(-\frac{\tau^2}{\sigma}\right) \pm 4\exp\left(-\frac{3\tau^2}{4\sigma}\right)\right] \tag{3.3.24}$$

It is common for the FWHM of the upper envelope to be considered as the width of the FRAC function, *i.e.* $S_+^{(2)}(\pm\overline{\Delta t}_{FRAC}/2) = 4|E_o|^4\sqrt{\pi\sigma}$, meaning

$$\overline{\Delta t}_{FRAC} = 2\sqrt{\sigma} \tag{3.3.25}$$

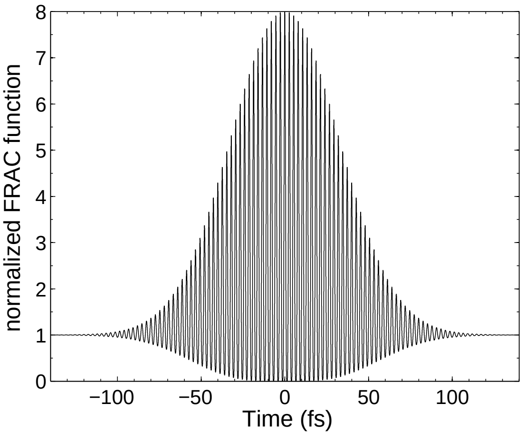

Figure 3.7: *Normalized FRAC function for a 50 fs FWHM pulse with* $\lambda_o = 800$ *nm* ($\omega_o = 2.36$ *fs*$^{-1}$)*. The equal amplitude of the fields leads to the ratio 8:1 between the maximum and the offset.*

So, the pulse width is simply

$$\overline{\Delta t} = \sqrt{\frac{\ln 2}{2}} \cdot \overline{\Delta t}_{FRAC} \simeq 0.589 \cdot \overline{\Delta t}_{FRAC} \tag{3.3.26}$$

In practice, however, it is useful to fit just the normalized upper envelope, $S_+^{(2)}/|E_o|^4\sqrt{\pi\sigma}$, with a Gaussian of the form $\chi \cdot \exp(-t^2/\xi) + \beta$, with $\chi = 7$ and $\beta = 1$. Then, the connection between the FRAC width and the parameter ξ reads

$$\overline{\Delta t}_{FRAC} = 2\sqrt{\xi \, \ln\left(\frac{7}{3}\right)} \simeq 1.841\sqrt{\xi} \tag{3.3.27}$$

while for the pulse width is

$$\overline{\Delta t} \simeq 1.0844\sqrt{\xi} \tag{3.3.28}$$

The things become greatly complicated when employing two different Gaussian pulses with linear chirp (eq. 3.3.11 with $\omega_{o1} = \omega_{o2} \equiv \omega_o$ and $a_1 = a_2 \equiv a$). Calculations of such normalized FRAC lead to

$$\begin{aligned} S^{(2)}(\tau) = 1 + \frac{E_{o1}^2 E_{o2}^2}{A}\sqrt{\frac{2\pi\sigma_1\sigma_2}{\sigma_1+\sigma_2}}\, e^{-\frac{2\tau^2}{\sigma_1+\sigma_2}} \left[2 + e^{-2\frac{\sigma_1\sigma_2}{\sigma_1+\sigma_2}\, a^2\tau^2} \cos\left(2\omega_o\tau - 2\frac{\sigma_1-\sigma_2}{\sigma_1+\sigma_2}\, a\tau^2\right)\right] + \\ + 4\frac{E_{o1}^3 E_{o2}}{A}\sqrt{\frac{\pi\sigma_1\sigma_2}{\sigma_1+3\sigma_2}}\, e^{-\frac{3+\sigma_1\sigma_2 a^2}{\sigma_1+3\sigma_2}\,\tau^2} \cos\left(\omega_o\tau + \frac{3\sigma_2-\sigma_1}{3\sigma_2+\sigma_1}\, a\tau^2\right) + \\ + 4\frac{E_{o1} E_{o2}^3}{A}\sqrt{\frac{\pi\sigma_1\sigma_2}{3\sigma_1+\sigma_2}}\, e^{-\frac{3+\sigma_1\sigma_2 a^2}{3\sigma_1+\sigma_2}\,\tau^2} \cos\left(\omega_o\tau + \frac{\sigma_2-3\sigma_1}{\sigma_2+3\sigma_1}\, a\tau^2\right) \end{aligned} \tag{3.3.29}$$

where

$$A = E_{o1}^4\sqrt{\frac{\pi\sigma_1}{4}} + E_{o2}^4\sqrt{\frac{\pi\sigma_2}{4}} \tag{3.3.30}$$

is the far-off-coincidence offset ($|\tau| \gg 0$). An example is shown in the figure 3.8 where two different linearly chirped pulses, with 50 and 70 fs FWHM, are fringe-resolved autocorrelated. The longer one has also a bigger amplitude which prevents the shape of the FRAC to yield the usual 8:1 ratio. Other effects, like the *wings* (referred previously), in the FRAC experimental signal can be explained by allowing third or higher order terms in the wave-vector expansion (eq. 2.4.34), which translates in a higher-order chirp for the pulses involved. In principle, if one has the spectra of the pulses, it is possible, *numerically*, to reproduce *any experimental* FRAC curve [27]. In the case of a very complicated pulse the *noise* prevents interference from happening so the FRAC looks very much like a spike in the middle of a pedestal, similar as for the IAC. Also, for two pulses with different frequencies the FRAC is giving an IAC-like signal and presents fringes only if the pulses are extremely short (few optical cycles).

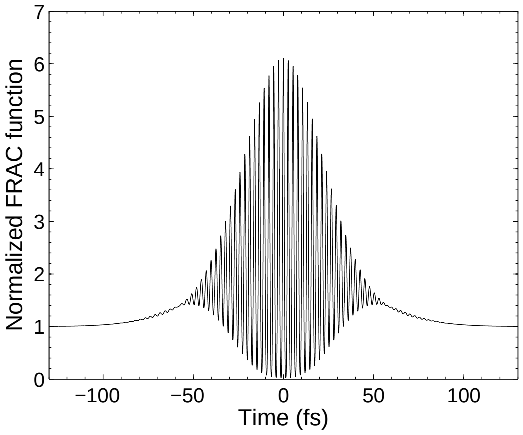

Figure 3.8: *Normalized FRAC function for two pulses of 50 and 70 fs FWHM ($\lambda_o = 800$ nm), the later having a 50% bigger amplitude. The chirp parameter is $a = 0.001$ fs^{-2}. The ratio 8:1 is no longer respected.*

Pulse measurement is usually done with thin SHG crystals. However, there are situations when the SHG crystals can not double the incoming frequency anymore (for far-UV light, as example). In these cases, the methods employed vary with the constrains but they are all based on the two-photon pump-probe technique (two-photon fluorescence, photoionization, photoconductivity, photoemission or absorbtion) [67]. Furthermore, many pump-probe experiments require comparison with the FRAC (or IAC) in order to explain lifetimes or decay times of different effects (like plasmon dephasing in nanoparticles [68, 69], as example).

Despite a tremendous effort for finding a viable algorithm which extracts the pulse uniquely when *all* traces are available (spectrum, IAC and FRAC) [70], there is no clear evidence that this methods are yielding the right information in *all* possible cases. However, it was shown that by including a second FRAC measurement, in which a glass-plate with a known dispersion is placed in one of the interferometer arms, there is enough information to completely characterize the pulse [71, 72]. Unfortunately there are no extensive studies made on the performance of this algorithm. Also, it is very rarely used as it tends to stagnate.

The best method for pulse measurement so far is the *Frequency-Resolved Optical Gating* (FROG), introduced by R. Trebino [73, 74] in 1993, which *gates* the pulse with itself and acquires the information *simultaneously* in the time-frequency domain. It measures the *spectrogram*, meaning series of spectra of all gated parts of $E(t)$ in time [22]. The setup is similar with an IAC but replaces the usual slow detector with a spectrometer while one of the arms contains some well known optical elements (polarizers, filters, etc). It makes use of the fact that the *Fundamental Theorem of Algebra* (which states that the polynomials of one variable can be *factorized*) *fails* for polynomials of two variables. This implies that the two-dimensional phase retrieval is not only possible, but also gives an unique solution in all cases. The FROG algorithm outputs the *exact* field of the pulse $E(t)$, including the *spectral* phase. Essentially, the knowledge of the spectrogram of $E(t)$ is sufficient to completely determine $E(t)$, except for some minor ambiguities like the *total* phase, which is of no interest for most optical applications. There are several known FROG setup variations leading to the same pulse output, some of them even using a *Third Harmonic Generation* (THG) crystal [19, 45] instead of the usual SHG. However, the Polarization-Gate (PG) FROG apparatus is the most intuitive one.

A few years ago the FROG setup was greatly simplified into the so-called *GRating-Eliminated no-Nonsense Observation of Ultrafast Incident Laser Light E-fields* (GRENOUILLE) [75, 76], a device which is very easy to align (needs *no* delay stage) and which produces in real time, directly on a CCD camera, traces that are identical to those of SHG FROG, yielding the *full* pulse intensity and phase (except the direction of time). To date, this *single-shot* FROG is the simplest and the most ingenious method for pulse measurement in the visible range. However, it still relies on the FROG algorithm for the actual pulse information extraction.

3.4 Experimental Pulse Characterization.

Tools for characterizing the pulse shape, spectrum and temporal width are a must in accurate studies of ultrafast processes. In the frequency domain we use a Rees Instruments Laser Spectrometer in order to determine the pulse spectra. These measurements show that the pulses from the MIRA oscillator have a spectral width of about 28 nm (fig. 3.9), meaning that the pulses have a minimum temporal width of 33 fs. In the time domain, we employed first a Michelson Interferometer (as presented before, fig. 3.4) which has two silver mirrors in the arms and a 50% beam-splitter (*p-polarized* [17] beam with $\lambda_o = 800$ nm) for pulse separation. A Hamamatsu 931A Side-on Type Photomultiplier Tube (PMT) with a gain of 10^7 and sharp sensitivity cut-off between 650 and 700 nm was used as detector. The PMT amplification voltage was held at 500 V while the incoming laser beam power was kept far above 10 mW (around 200 mW) in order to preserve the linear response of the device which, despite the sharp wavelength sensitivity cut-off, was still sufficiently strong at 800 nm to mask the second-order 2PPE signal. The delay-stage consists of a computer controlled *piezocrystal* [19] which moves a Newport ball-bearing stage [44] in one of the branches of the interferometer. The *piezoelectric* expansion [19] of the crystal, at maximum $\simeq 65$ μm, can be varied by a high voltage applied on its sides ($0 \leftrightarrow -1000$ V)[1]. The calibration

---

[1] where the -1000 V corresponds to the maximum expansion of $\simeq 65$ μm.

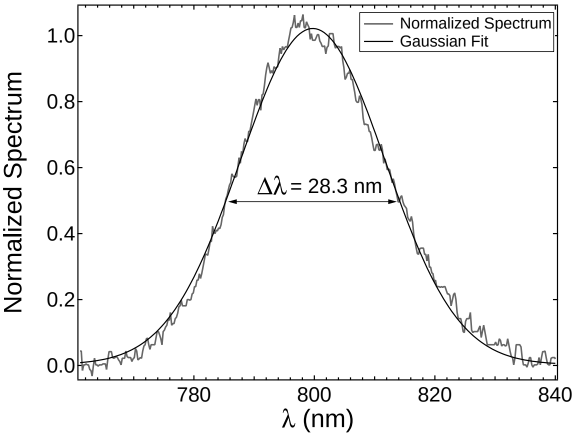

Figure 3.9: *The usual normalized spectrum of the MIRA oscillator pulses* (λ_o = 800 *nm) acquired with the commercial Rees Spectrometer.*

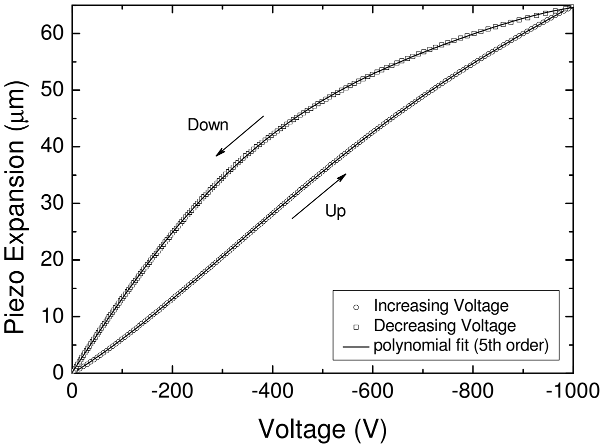

Figure 3.10: *The piezo hysteresis curve. For data acquisition the expansion (**up** curve) was mainly used rather than the constriction (**down** curve).*

measurement, performed by using a He-Ne CW laser, shows a quite strong hysteresis curve between the expansion and constriction of the crystal (fig. 3.10). The piezo voltage can be controlled by a computer or by a simple signal generator for online analysis.

In what follows we will make the assumption that the pulses generated by the MIRA oscillator have Gaussian shape envelope.

The interferogram of the MIRA-seed pulses is shown in the figure 3.11 together with a general fit as provided by the function in eq. 3.3.12. The most important parameters resulting from this fit are $A \simeq 1900$ fs^2, which gives the temporal width of the interferogram $\overline{\Delta t_{int}} \simeq 73$ fs, and the linear chirp $\alpha \simeq 3 \times 10^{-4}$ fs^{-2}. The pulse temporal width must be greater than the coherence length

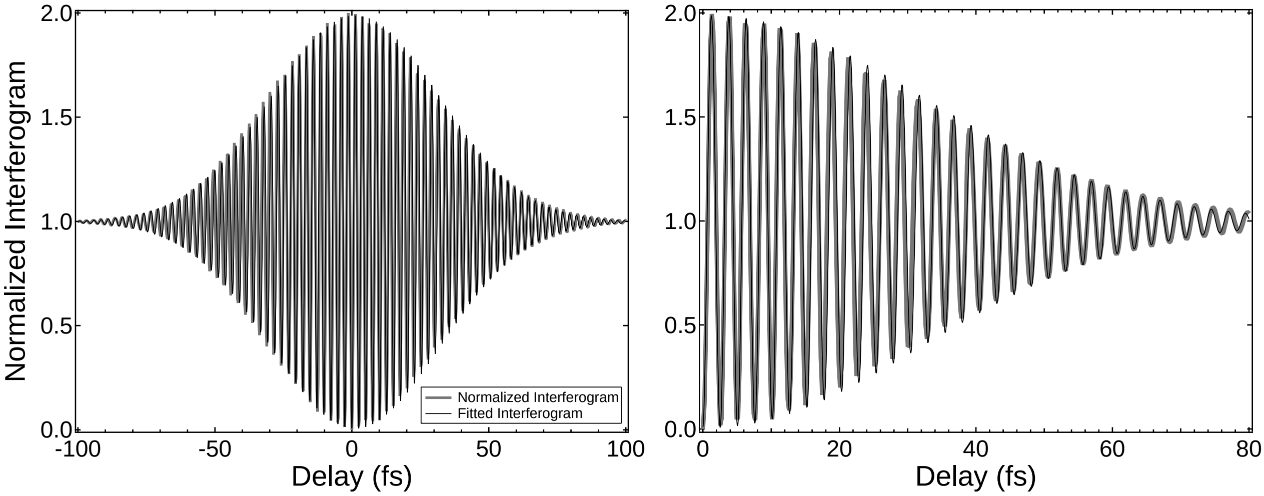

Figure 3.11: ***Left Graph**: The Interferogram of the oscillator pulses. The function in eq. 3.3.12 produces a very good fit of the data: the width parameter* $A \simeq 1900$ *fs*^{2} *and the chirp parameter* $\alpha \simeq 3 \times 10^{-4}$ *fs*$^{-2}$*. Data from ref. [77].* ***Right Graph**: Zoom on the delay region 0 to 80 ps.*

$\overline{\Delta t}_{int}/2 \simeq 36$ fs as implied by the eq. 3.3.15. Further, one can recall the fact that the Fourier transform of the interferogram leads to the spectrum of the pulse. Using eq. 3.3.16 a frequency spectral width $\overline{\Delta\omega} = 0.0879$ fs^{-1} is obtained. The conversion to the wavelength spectral width is done simply by the relation

$$\overline{\Delta\lambda} \simeq \frac{\lambda_o^2}{2\pi c}\,\overline{\Delta\omega} \tag{3.4.31}$$

which yields a spectrum $\overline{\Delta\lambda} \simeq 30$ nm, very close to the spectrometer measurement (fig. 3.9).

It is well known that the pulse temporal width can not be determined without employing nonlinear optics. Therefore we added a lens with 76 mm focal length and a 0.5 mm thin BBO crystal (with sufficient phase-matching bandwidth) before the PMT detector in order to reproduce the FRAC setup (fig. 3.6). In the normalized data, presented in the figure 3.12, one can see that the wings are quite prominent while the ratio 8:1 condition is still fulfilled, meaning that the pulses have a higher order chirp and that their amplitudes are equal, respectively. The fit was done with the normalized FRAC function, as shown in eq. 3.3.29, in which the obvious assumptions $\sigma_1 = \sigma_2 \equiv \sigma$ and $E_{o1} = E_{02} \equiv E_o$ have been made. The resulting pulse width and linear chirp parameter are $\overline{\Delta t} \simeq 81$ fs and $a \simeq 3.6 \times 10^{-4}$ fs^{-2}, respectively. One observation is that the FRAC data are not *perfectly symmetric* around the coincidence time 0. This can be assigned to the nonlinear *expansion behavior* of the piezo crystal which is not *completely reproducible*. Therefore, it is rather difficult to relate *exactly* each point from the experimental data with the actual corresponding time delay between the pulses. Also, as mentioned before, the wing magnitudes, at the sides of the FRAC, are not reproduced by the theoretical FRAC function because the higher order chirp is not considered. Usually one can directly fit the upper envelope of the FRAC data-set with a Gaussian and extract from its width the time duration of the pulse, as shown in eqs. 3.3.26-3.3.28. A pulse width of 64 fs

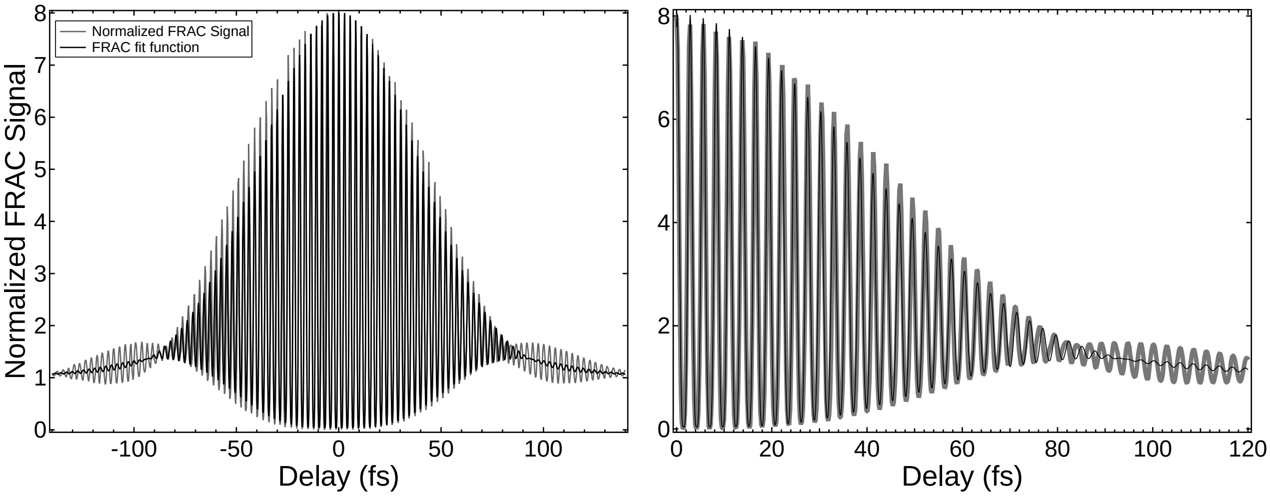

Figure 3.12: ***Left Graph**: The normalized FRAC data as recorded in our setup. The fit is done with the function in eq. 3.3.29. The signal was filtered with a blue-pass filter and normalized to the far-off coincidence background. The wings are not reproduced by the fit because the higher-order chirp is not considered. Data from ref. [77]. **Right Graph**: Zoom on the delay region from 0 to 120 ps.*

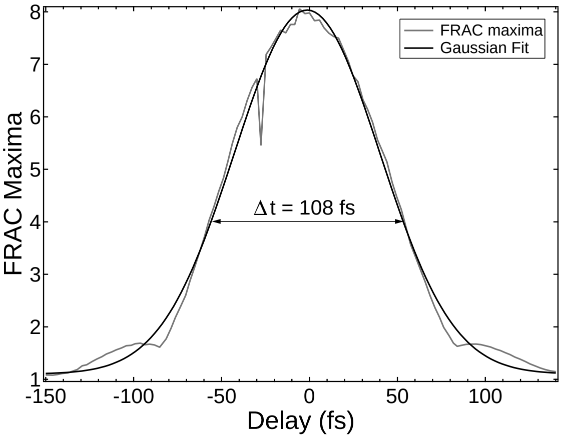

Figure 3.13: *The normalized FRAC upper envelope data is fitted with a Gaussian. The width is determined by the intersection with the 4 and not the 4.5 level as one may think from the simple Gaussian FWHM consideration.*

was calculated which is significantly smaller than the value of 81 fs extracted from the full FRAC data. The reason for this difference is that the pulses have an important chirp, visible in the wings of the FRAC data. As mentioned in the previous chapter, the more complex a pulse is the simpler the FRAC function becomes, *i.e* a spike on a pedestal. In our case the upper envelope is no longer just a function of the pulse width but also of the coherence length. Paradoxically, when the chirp increases, the main curve is becoming a measure of the coherence length while the wings show the actual pulse width. In the figure 3.13 one can observe that the wings extend quite farther than the actual fit, which is mostly related to the main curve. Therefore it is reasonable to assume that the value of 81 fs is the actual time duration of the MIRA-seed pulses after the FRAC setup.

To further elucidate the above issue, the FRAC setup was changed into a IAC one, as shown in the figure 3.5, by adding a mirror in each of its arms (in order to spatially separate the beams before the BBO crystal while keeping them parallel) and by removing the remnant fundamental light with an appropriate filter. The data was recorded with the same PMT used in the previous configurations. A Gaussian function fits rather well the IAC trace and, under the assumption that the two interfered pulses have the same properties, outputs a pulse width of about 81 fs (eq. 3.3.19), identical with the one obtained from the general FRAC fit (fig. 3.12). The 2PPE experiment on a clean polycrystalline silver surface, presented in detail the chapter 6, brings even more support for this value. It will be shown that with pulses of two different frequencies ($\lambda_{01} = 800$ nm and $\lambda_{02} = 400$ nm) one can perform an IAC (eq. 3.3.21) by using a surface that has no resonant electronic transition as nonlinear medium. In figure 2.6, for example, the initial blue pulse was retrieved to be about 83 fs from the IAC trace recorded from a silver polycrystalline surface. The slight deviation from symmetry around the delay 0 can barely be observed at the top of the curve. The effect can be neglected as it is far less obvious than the one in the case of the FRAC data.

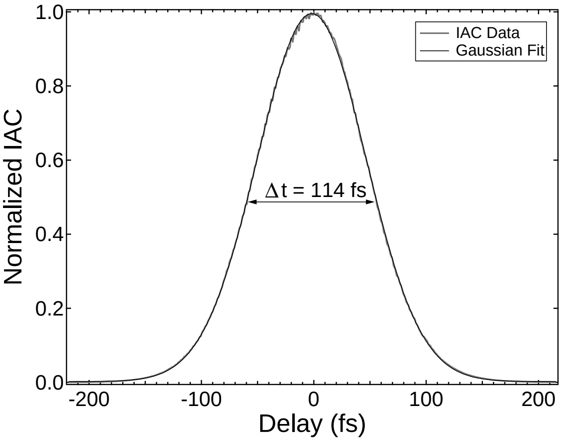

Figure 3.14: *The normalized IAC data fitted with a Gaussian. The extracted time duration of the interfered pulses is about 81 fs.*

Since the actual MIRA-seed pulse, measured at the output of the oscillator with a commercial autocorrelator, is 55 fs, it can be stated that our measurements have introduced several errors. First, the used BBO crystal was fairly thick (0.5 mm) thus producing a temporal broadening of the SHG generated pulse through both limiting bandwidth and positive GVD. Second, the use of optical components which were not perfectly suited for the pulse center wavelength λ_o (like the silver mirrors) further increased the time duration of the measured pulses.

Later on, the FRAC setup was simplified by replacing the BBO and the PMT detector with a photodiode which has a bandgap of $2\hbar\omega_o$, thus providing both the linear detection and the nonlinear optic effect. Also, the increase of the chirp and time duration was clearly observed when a piece of glass was placed in the path of the initial beam.

Our goal was to build an autocorrelator capable of online analysis. Hence, the setup was able to function at high scan rates allowing for optical paths and pulse compression stages to be optimized in real-time. However, the fast scans have the disadvantage of lower reproducibility of the piezo expansion in each data acquisition cycle. Also, the nonlinear crystal (β-BBO) used for the SHG had a width of 0.5 mm which translated into an energy bandwidth of 43 meV for the 'ooe' phase matching condition ($\omega_{800}+\omega_{800} = \omega_{400}$). As the fundamental pulses ($\lambda_o = 800$ nm) had a bandwidth of more than 55 meV the SH blue pulses generated in the BBO had a shorter spectrum than the complete possible SHG spectrum of the red pulses. In principle, judging from the square dependence of the SHG intensity on the fundamental intensity, the SHG spectrum ought to have a width of the form

$$\overline{\Delta\lambda}_{2\omega_o} \simeq \frac{1}{2\sqrt{2}}\overline{\Delta\lambda}_{\omega_o} \tag{3.4.32}$$

Thus, the SHG blue spectrum width of a $\simeq$ 28 nm wide red spectrum should be about 10 nm. However, the measurements showed that the width of the blue pulses was close to 5 nm. Therefore, the blue pulses produced in the autocorrelation experiments yielded longer temporal widths than if a thinner BBO had been used.

Chapter 4

Two-Photon Photoemission

4.1 Photoelectron Spectroscopy

The photoelectric effect states that electrons are emitted from matter upon the absorption of electromagnetic radiation which is above a certain threshold frequency, such as ultraviolet radiation (UV) or X-rays. It was correctly described by A. Einstein in 1905 [78], who first connected the kinetic energy of the extracted photoelectrons E_{kin} with the absorbed photon energy $h\nu$, the binding energy E_B and the material work function Φ :

$$E_{kin} = h\nu - E_B - \Phi \qquad (4.1.1)$$

In a simple picture, photoelectron spectroscopy (PES) is a spectroscopic technique which measures the kinetic energy of electrons emitted upon the ionization of a substance by high energy monochromatic photons. A photoelectron spectrum is a plot of the number of electrons emitted versus their kinetic energy. The spectrum consists of peaks due to transitions from the ground state of an atom or molecular entity to the ground and excited states of the corresponding radical cation. Approximate interpretations are usually based on *Koopmans theorem* [79] and yield orbital energies. UPS (UV photoelectron spectroscopy) refers to the spectroscopy using vacuum ultraviolet sources, while XPS uses X-ray sources. Both are important for their specific energy range: UPS for probing the valence electronic structure and XPS for the core levels. These techniques are extensively discussed by several authors (see e.g. [79]). Usually the binding energy scale is preferred in PES because its origin is the Fermi level (chemical potential) and the spectrum peak positions follow naturally the occupied electronic band structure. In principle, one can easily obtain the Fermi level within a given experimental situation from the valence spectrum of a metal (e.g. polycrystalline silver).

A real solid is a complicated many-body system whose electrons interact between themselves. In order to simplify the quantum many-body problem [80] it is useful to introduce the concept of *quasiparticles* (QPs) [81] which refers to a small disturbance in a medium that behaves like a particle entity. In the case of photoemission the QP is related to the photoelectron extracted and the hole left behind which interacts with the solid's electronic system. The QPs possess wavefunctions that fulfill the Schrödinger equation but with complex self energies $\Sigma(\mathbf{k}, E)$ which add to the ground state energy. The real part of the self energy (Σ_R) represents the energy shift of the QP due to the

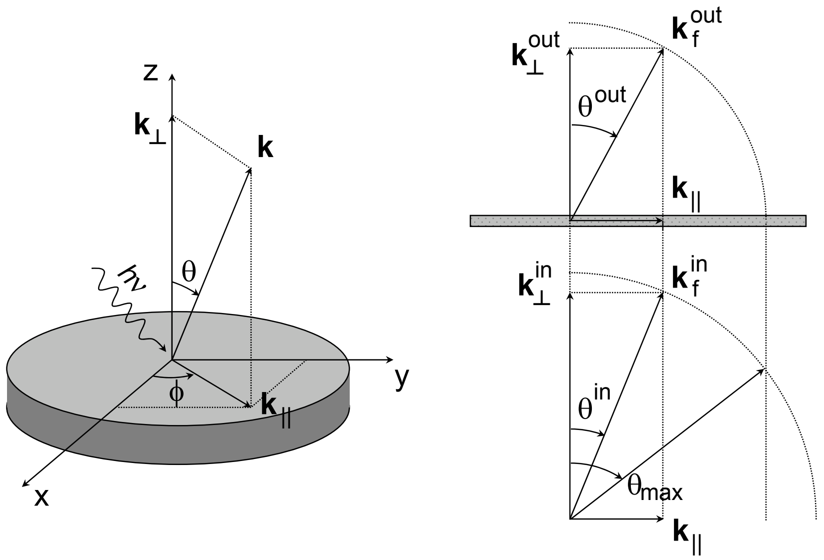

Figure 4.1: *Photoemission geometry.*

screening while the imaginary part (Σ_I) is a result of the inelastic scattering processes. Under the assumption that the photoelectron extraction probability is constant over the energy/momentum range of interest, the distribution of photoelectrons emitted from an electron band with the ground state energy $E_i(\mathbf{k})$ is given by the hole *spectral function* [82–84]

$$A(\mathbf{k}, E_f) = \frac{1}{\pi} \frac{|\Sigma_I|}{[E_f - E_i(\mathbf{k}) - \Sigma_R]^2 + (\Sigma_I)^2} \tag{4.1.2}$$

where E_f is the energy of the electron final state. The self energy adds linearly all the possible interactions which derive from the photoelectron extraction: electron-electron scattering, electron-phonon scattering, hole scattering at sample impurities or defects. In many cases the hole wave-function can be described by an exponential decay in time. This makes such that the spectral function becomes a Lorentzian which is usually called the QP peak. The linewidth of the QP peak, Γ, is given by

$$\Gamma = 2\Sigma_I = \frac{\hbar}{\tau} \tag{4.1.3}$$

where τ is the hole *lifetime.* It should be mentioned that in the spectral function 4.1.2 the QP energy $E_i(\mathbf{k}) + \Sigma_R$ is not the ground state energy [85].

In the simple picture of a noninteracting electron system the connection between the measured spectrum and the initial state of an electron in the solid is described by the *three-step model* [86] which splits the process into three steps: photoexcitation, propagation to the surface and escape into vacuum [79, 87]. In the first step, the electron is excited from an initial state i to a final state

f inside the solid. This process happens with conservation of the energy and momentum

$$\begin{aligned} E_f(\mathbf{k}_f) &= E_i(\mathbf{k}_i) + h\nu \\ \mathbf{k}_f &= \mathbf{k}_i + \mathbf{k}_\gamma + \mathbf{G} \end{aligned} \tag{4.1.4}$$

where $\mathbf{G}$ is a vector of the reciprocal lattice which must be considered due to the very small photon momentum ($\sim 0.1\%$ of a typical Brillouin zone) in the case of UV light. These are called *direct transitions*. The final state is considered to be free electron like and its energy differs from the energy E_{kin} measured in the vacuum by the *inner potential*, V_o, which accounts for the surface effects during the escape of the electron into the vacuum

$$E_f = h\nu - E_B - \Phi + V_o \tag{4.1.5}$$

During the second step, the electrons scatter elastically and inelastically. The elastic scattering effects can be used for mapping of the surface structure by recording core level patterns (XPD) [88, 89]. The inelastically scattered electrons account for the smooth background in the spectrum which increases towards lower kinetic energies. In several materials they can also induce *plasmons* which add a succession of peaks at lower kinetic energy with a periodicity given by the plasmon frequency. The third step conserves only the parallel momentum which can be calculated from the measured kinetic energy E_{kin} of the electrons which are extracted with the polar and azimuthal angles θ^{out} and ϕ with respect to a coordinate system whose z axis is the sample normal while the x and y axes are taken in the sample surface and related to some known crystallographic directions (fig. 4.1):

$$\hbar\mathbf{k}_{||} = \sqrt{2m_e E_{kin}}\,\sin\theta^{out}\,(\cos\phi, \sin\phi, 0) \simeq 0.51232\,\hbar\sqrt{E_{kin}(eV)}\,\sin\theta^{out}\,\mathbf{e}_{r||} \tag{4.1.6}$$

Experimentally it is shown that the momentum in perpendicular direction is provided to a good approximation by the final state energy E_f as [90]

$$\hbar\mathbf{k}_\perp^{in} = \sqrt{2m_e(E_{kin} + V_o)}\,\cos\theta^{in}\,\mathbf{e}_z \tag{4.1.7}$$

As the final parallel momentum inside and outside the solid is conserved one can deduct the polar angle of the electron inside the solid

$$\sin\theta^{in} = \sin\theta^{out}\left(\frac{E_{kin}}{E_{kin} + V_o}\right)^{1/2} \tag{4.1.8}$$

also known as the *electron surface refraction law.* These formulas are useful for calculating the actual electron momentum inside the solid when experimentally measuring the emission angle and kinetic energy outside the solid. Studying two- and one-dimensional systems simplifies the problem because the perpendicular component of the momentum can be most of the time ignored. Experimentally, the single particle spectral function is measured with angle-resolved photoemission spectroscopy (ARPES) [79].

When very small photon energies are used to probe the electronic band structure of a solid, usually, one must negatively bias the sample in order to avoid entering the low transmission region of the

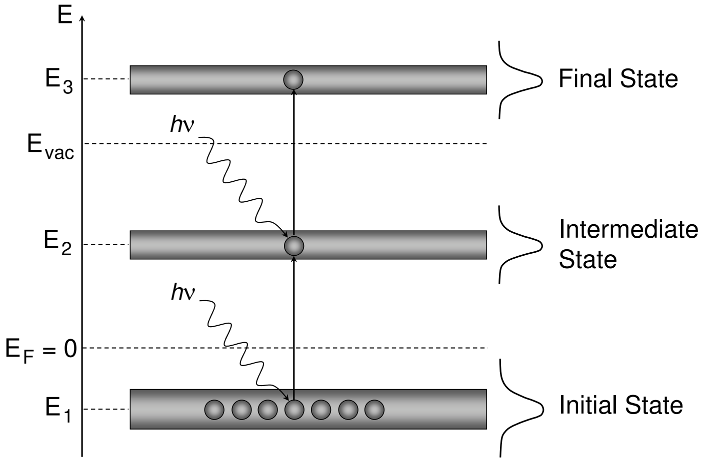

Figure 4.2: *Initial state resonant excitation through 2PPE via an intermediate state.*

analyzer. In such cases, the negative bias induces a lensing effect which modifies the trajectories of the photoelectrons towards the analyzer. While in normal emission the photoelectrons are unaffected, at any other emission angle their trajectories will be bent by the electric field. Therefore the analyzer will record them at an angle different from the one they were actually emitted from the solid. This lensing effect can be compensated within certain situations. For small detected photoelectron angles, θ_{det}, ray tracing calculations show that their real surface angle, θ_{real}, is given by [91]

$$\theta_{real} = a(E_B) \cdot \theta_{det} \tag{4.1.9}$$

where $a(E_B)$ is a coefficient which depends on the binding energy E_B (in eV) as

$$a(E_B) = 1.68 + 0.25E_B + 0.35E_B^2 \tag{4.1.10}$$

for a bias of -10 eV.

4.2 Two-Photon Photoemission (2PPE) Basics

A special case of PES is two-photon photoemission which needs two photons to be absorbed by the crystal in exactly the same time and space in order to extract a photoelectron over the vacuum level. Such situations are met upon shining on a sample with a high-density photon flux, as provided by ultrashort laser pulses. In principle, the excitation induced by a first photon (pump) raises an electron to an intermediate or virtual state. If a second photon (probe) is absorbed in the same location and within a certain time, comparable to the lifetime of the excited state created by the first photon, then the electron can gain enough energy to reach the vacuum. When the delay between the two photons is varied in a controlled way one speaks of time-resolved 2PPE (t-2PPE). Its main purpose is the investigation of the electron density excitation and relaxation of intermediate and final states. Theoretically the 2PPE process is described by the optical Bloch equations [4, 92, 93]. Studies of hot electron dynamics on semiconductor [94] and metal surfaces [4,95], time-resolved spin dependence [96] and dynamics of image-potential states [97, 98] have been performed by making use of the t-2PPE method. Also, 2PPE is an interesting alternative to inverse photoemission [79] for studying unoccupied states. Unfortunately, interpreting the spectra which result from a 2PPE experiment is not an easy matter.

It is rather a delicate problem to assign the peaks appearing in a time-resolved 2PPE experiment to surface or bulk states, to intermediate or initial states if the occupied and unoccupied band structure of the system under investigation is not well known in advance. Therefore, most of the time, the 2PPE data is cross-referenced with other data provided by 'classical' methods like UPS or ARUPS. When considering all possibilities which can yield a peak in a time-resolved 2PPE spectrum, one distinguishes several scenarios:

(*1*) A well defined occupied initial state of energy E can be non-resonantly excited by a pump photon into a virtual state and subsequently probed by another one. The resulting peak in the spectrum will be situated at the energy $E + 2h\nu$ [99], similar with what will be measured in a regular ARPES experiment with a photon energy of $2h\nu$ [100]. The cross-correlation curve at the peak energy, produced when varying the delay between the pump and probe pulses, will be given by the IAC of the two pulses. Usually plasmons are created due to the high photon flux in the laser pulses and therefore, the time duration of the 2PPE excitation can be broader than the simple pulse IAC [68].

(*2a*) If electrons from an initial occupied state (E_1) are resonantly excited into an intermediate state of energy E_2 and further excited into a final state (E_3), the resulting spectrum will present a very intense peak at the energy $E_2 + h\nu$ (fig. 4.2). The peak will shift linearly with the changing photon energy because the second excitation step is dominant. However, detuning the photon energy can lead to a consistent drop of the resonant peak [101].

(*2b*) It is also possible that an intermediate state at energy E_2 is populated by indirect excitations due to scattering of photoexcited hot electrons from the substrate. Even though this indirect transition mechanism will provide the same peak dependence on the photon energy as in the case (*2a*), the two processes can be distinguished following their different dependence on the photon polarization [102].

(*3*) The peaks which appear in a 2PPE spectrum do not necessarily have to originate from an initial state nor must their existence be connected to the existence of an intermediate state. They can simply be the result of 2PPE direct or indirect excitation of electrons into the final state through diffraction effects [103]. The peak positions do not depend on the photon energy and they are usually broad and quite weak. Also, the time duration of the cross-correlation peak can be assigned to the IAC of the pump and probe pulses involved.

4.3 Theoretical Notes of 2PPE

The light-matter interaction problem can not be solved exactly for real systems since they have a very large number of degrees of freedom. Theoretically, the common model is to divide the real system into two parts, a small *quantum system* containing a few energy levels and a macroscopic *thermal bath.* The idea behind such model is that only the quantum system is coupled to light (which decreases considerably the degrees of freedom) but its phase coherence is affected by the coupling with the bath. There are various methods to solve such complex model. The simplest one is referred to as the *Bloch equation* [25, 93] which assumes that the relaxation process does not depend on the history of the system but on its current state and it has been shown to fail for several cases [104–106]. In principle, the quantum system is described by the density operator $\hat{\rho}$ which is assumed to obey the *equation of evolution* [25, 93]:

$$i\hbar\, d_t\hat{\rho} = [H_0, \hat{\rho}]_- + [-\hat{\mu}E(t), \hat{\rho}]_- + i\hbar\, \partial_t\hat{\rho}|_{relax} \tag{4.3.11}$$

where H_0 is the unperturbed Hamiltonian of the quantum system (with $H_0|n\rangle = \hbar\omega_n|n\rangle$), $E(t)$ is the total electric field of the incident femtosecond pulse and $\hat{\mu}$ is the electric dipole operator. The last term represents the interaction with the bath which leads to relaxation. In the Bloch model, the matrix elements of this term are following the relation

$$\partial_t\rho_{nm}|_{relax} = -\Gamma_{nm}(\rho_{nm} - \rho_{nm}^{(0)}) \tag{4.3.12}$$

which leads to an exponential relaxation with a decay rate Γ_{nm} of the corresponding population $\rho_{nm} = \langle n|\hat{\rho}|m\rangle$. Γ_{nm} represents either a dephasing rate or a population relaxation rate if $n \neq m$ or $n = m$, respectively. The density operator at thermal equilibrium, $\hat{\rho}^{(0)}$, is diagonal and, in most of the situations, it is considered that only the ground state is populated ($\rho_{00}^{(0)} = 1$). The equation 4.3.11 is usually solved by assuming that the electric field, $E(t)$, is small enough such that the density operator, $\hat{\rho}(t)$ can be expanded in terms of it. It can be shown that for a two level system case, $|g\rangle$ (ground) and $|e\rangle$ (excited), there are only two relaxation rates which appear: $\Gamma_{ee} = 1/T_1$ with T_1 the population relaxation time and $\Gamma_{eg} = 1/T_2$ with T_2 the dephasing time [25].

The physics underlying t-2PPE are given by the relative time scale among the time duration of the laser pulses $\overline{\Delta t_p}$ and the dephasing time between the initial and the intermediate state (T_2). If $\overline{\Delta t_p} \gg T_2$ then there is no coherent superposition between the polarization of the system and the electromagnetic field oscillations. In this case, the Bloch equation reduces to the *rate equation* [107–110] (*incoherent* effect), which is then appropriate for describing the temporal response of the excited population. Small electron density excitations (single electron excitation) can also be treated as incoherent. For a simple two level system case ($|g\rangle$ and $|e\rangle$), the rate equation for the excited population is derived from the Einstein rate equation which adds a source term proportional to the pump pulse intensity, $I_{pump}(t) = |E_{pump}(t)|^2$ [109]:

$$d_tN_e = RI_{pump}(t) - N_e/T_1 \tag{4.3.13}$$

where R is a fit parameter[a]. Such equation like 4.3.13 can only be solved numerically if $I_{pump}(t)$ does not have a very simple form. Further, the total electron yield outside the sample (N_D) is computed by convoluting N_e with the intensity of the probe pulse (I_{probe}). Actually, in the first

---

[a] physically is given by the cross section of the transition and light intensity at the sample.

t-2PPE experiments the transient electron yield (or count rate, since the measurements are done in a limited time), N_D, was modeled with a simple function:

$$N_D(\Delta t) = A(\Delta t) \cdot \exp\left(-\frac{\Delta t}{T_1}\right) \tag{4.3.14}$$

where Δt is the time delay between the two pulses and $A(\Delta t)$ is their autocorrelation[b]. The above equation is actually a strongly approximated solution of the rate equation 4.3.13. Such function, however, is not yielding a good fit of the data and therefore it is not very often used.

On the other hand, when $\overline{\Delta t_p} \lesssim T_2$, namely when the exciting pulse duration becomes comparable with, or even shorter than the phase relaxation time of the excited medium, and in the presence of pump and probe overlap during dynamical change of photoinduced polarization, the *coherent* effects can no longer be neglected. In this case the electrons are collectively excited in large densities and the model describing this process is again the Bloch equation [93].

In a one-color t-2PPE experiment only one intermediate state can be resonantly pump-probed (if it exists) and the resulting transient electron yield is symmetric around the coincidence between the laser pulses. Further, comparison with the IAC curve of the pulses should indicate the existence and, roughly, the possible lifetime of the intermediate state. On the other hand, the two-color t-2PPE allows for two intermediate states to be simultaneously excited. The electron yield in such situations is no longer symmetric and the information about the lifetimes of the states can be difficult to extract.

In our experimental setup we made use of two different pulse energies (see chapter 4.4). Therefore, a model involving two possible intermediate states had to be employed. Since the experimental transients within our setup were similar to the expected intensity cross-correlation (ICC) of the pulses, the simple rate equation could not be directly used (see chapter 5.4). Instead, a new model was found, which deals with the pump-probing excitation in a classical electrodynamics picture where the 2PPE cross-correlation along the delay between the pump and probe pulses can be estimated by making two simple but reasonable assumptions (fig. 4.3):
(a) The excited electron density in the intermediate or final state are following the temporal profile of the pulse intensity.
(b) The electron density in the unoccupied intermediate state decays exponentially (consider only inelastic scattering).

Let us consider two FTL pulses (denoted by the subscript r and b, with photon energies $h\nu_r$ and $h\nu_b$ respectively) with Gaussian temporal profiles and a sample surface with two intermediate states ($|ir\rangle$ and $|ib\rangle$ with energies E_{ir} and E_{ib}), an initial state ($|i\rangle$ with energy E_i) such that $h\nu_r + E_i = E_{ir}$ and $h\nu_b + E_i = E_{ib}$. Let us also assume that the work function of the sample is sufficiently small such that an electron which acquires the energy $h\nu_r + h\nu_b$ can be extracted from the solid. Summarizing, the two pulses will have an intensity of the electric field profile of the form

$$I_{r,b}(t_o) = |E_{or,ob}|^2 \exp\left[-\frac{(t_o - t_{or,ob})^2}{\sigma_{r,b}}\right] \tag{4.3.15}$$

---

[b] or cross-correlation in case the pulses have different central frequencies, like in a two-color 2PPE.

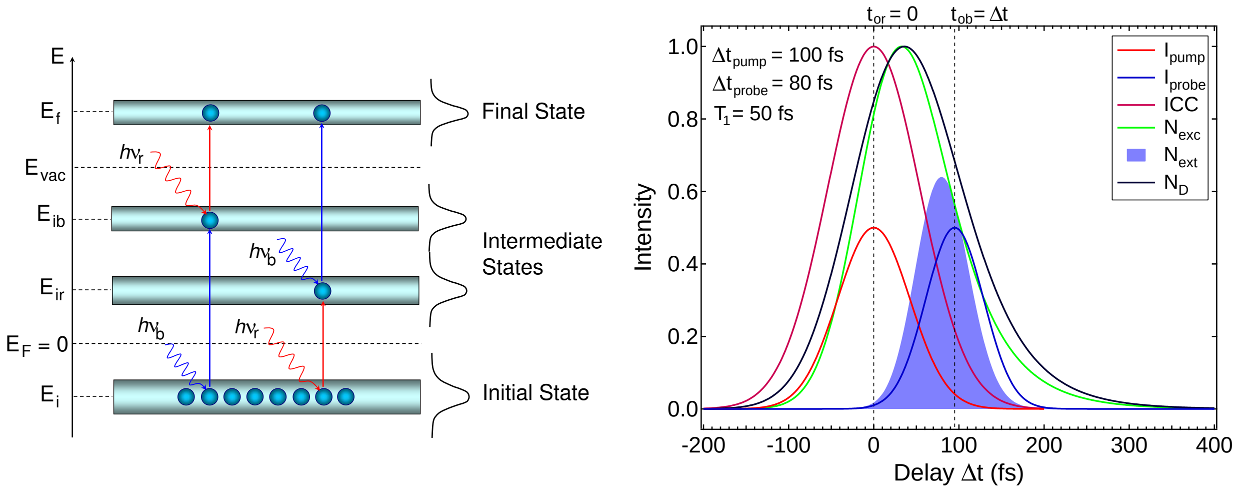

Figure 4.3: ***Left Graph**: The two-channel 2PPE process. In real samples the condition* $E_{ir,ib} = h\nu_{r,b} + E_i$ *is not always fulfilled.* ***Right Graph**: The t-2PPE model applied to system with one initial and one intermediate state. The excitation and extraction processes follow the intensity of the laser pulses* ($|E(t)|^2$)*. The red (pump) pulse envelope centered at* $t_{or} = 0$ *is setting the delay zero (as the origin of the temporal dynamical coordinate system). The population induced in the intermediate state by the red pulse,* N_{exc}*, is represented by the green curve. The instantaneous extracted electron yield,* N_{ext}*, is then simply given by the modulation of the curve* N_{exc} *with the envelope of the blue (probe) pulse intensity. The area of this modulation (blue area) gives one point on the total detected electron yield,* N_D *(dark blue curve), at the time* $t_{ob} = \Delta t$*. All the curves are normalized to unit except the pulses intensities which are normalized to 0.5 for clarity.*

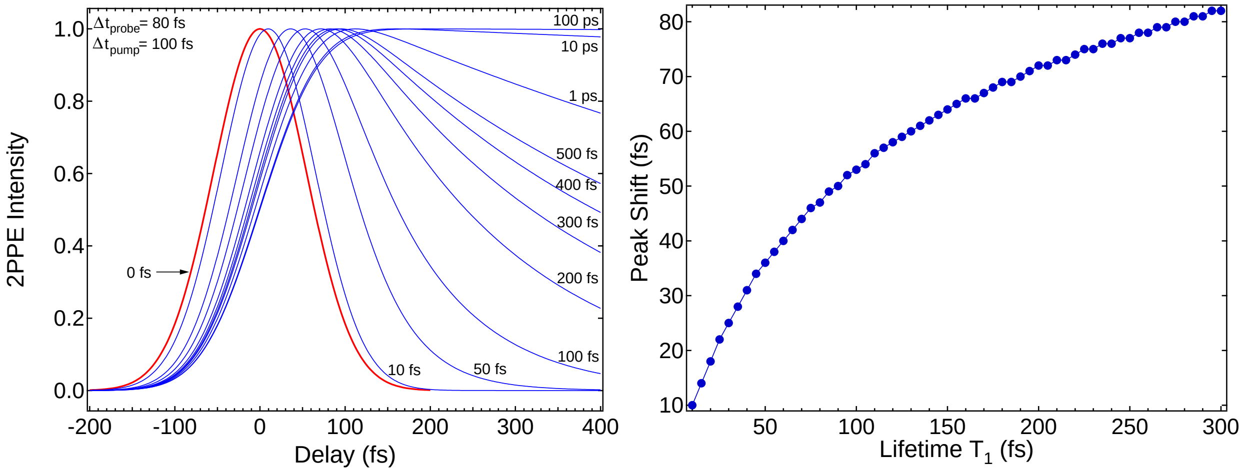

Figure 4.4: ***Left Graph**: Total transient electron yield* (N_D) *dependence of the intermediate state lifetime. If the lifetime of the intermediate state is zero then* N_D *becomes the simple ICC of the pulses, centered at the delay zero.* ***Right Graph**: The* N_D *peak is shifting from the actual delay zero between the pump and probe pulses when traced as a function of the intermediate state lifetime, following a logarithmic-like dependency.*

where $\sigma_{r,b}$ are related to the time widths of the pulses and $t_{o,r}$ are the pulse centers. The assumption (a) states that when one of the two pulses starts to hit the sample the *instantaneous* electron densities excited in the intermediate states will follow their electric field intensities

$$N_{or,ob} \propto I_{or,ob} \exp\left[-\frac{(t_o - t_{or,ob})^2}{\sigma_{r,b}}\right] \tag{4.3.16}$$

Since the *absolute time* can *not* be determined, the above formula is written by taking t_{or} (or t_{ob}, depending which pulse plays the role of the pump pulse) as the *origin* of a *dynamical temporal coordinate system.* With respect to this coordinate system, t_o (the moment when the pump pulse touches the sample), is a *variable* which can take practically any real value. If the population decay times in the two intermediate states are $\gamma_{r,b}$ then at the *instantaneous* time t the electron density in the two states will be

$$N_{exc}(t, t_{or}, t_{ob}) \propto \int\limits_{-\infty}^{t} dt_o \left\{ \alpha_r \exp\left[-\frac{(t_o - t_{or})^2}{\sigma_r} - \frac{(t - t_o)}{\gamma_r}\right] + \alpha_b \exp\left[-\frac{(t_o - t_{ob})^2}{\sigma_b} - \frac{(t - t_o)}{\gamma_b}\right]\right\} \tag{4.3.17}$$

where $\alpha_{r,b}$ are two proportionality constants which depend on the experimental details[c]. The electron density excited in each intermediate state can provide electrons in the final state $h\nu_r + h\nu_b + E_i$ if the subsequent probe pulse hits the sample within a reasonable time interval with respect to the pump pulse. When adding up the two contributions the extracted electron density reads

$$\begin{aligned} N_{ext}(t, t_{or}, t_{ob}) \propto \alpha_r \exp\left[-\frac{(t - t_{ob})^2}{\sigma_b}\right] \int\limits_{-\infty}^{t} dt_o \exp\left[-\frac{(t_o - t_{or})^2}{\sigma_r} - \frac{(t - t_o)}{\gamma_r}\right] + \\ + \alpha_b \exp\left[-\frac{(t - t_{or})^2}{\sigma_r}\right] \int\limits_{-\infty}^{t} dt_o \exp\left[-\frac{(t_o - t_{ob})^2}{\sigma_b} - \frac{(t - t_o)}{\gamma_b}\right] \end{aligned} \tag{4.3.18}$$

Since the instantaneous time t can virtually take any value between $-\infty$ and $+\infty$, the electron count rate (or total transient electron yield extracted for a given delay between the pulses) can be obtained by integrating the extraction electron density N_{ext} over the whole real axis

$$N_D(t_{or}, t_{ob}) \propto f \int\limits_{-\infty}^{+\infty} dt\, N_{ext}(t, t_{or}, t_{ob}) \tag{4.3.19}$$

where f is the pulse repetition rate (80 MHz for MIRA).

In practice, when calculating N_D, one can not obtain an analytical function due to the fact that N_{ext} does not yield a primitive with respect to t. Therefore, the final integration 5.4.3 must be done numerically. This means that the time t will be limited to an interval $(t_1; t_2)$ which is best suited for a given pair of pulse center times $t_{or,ob}$. Also, in reality, the absolute values of the pulse center

---

[c] For example, if the two intermediate states have energies which are not perfectly matching the conditions $E_{ir,ib} = h\nu_{i,b} + E_i$, then the cross-correlation peak around $h\nu_r + h\nu_b + E_i - E_{vac}$ will shift in time depending on which channel contributes more at a given final state energy

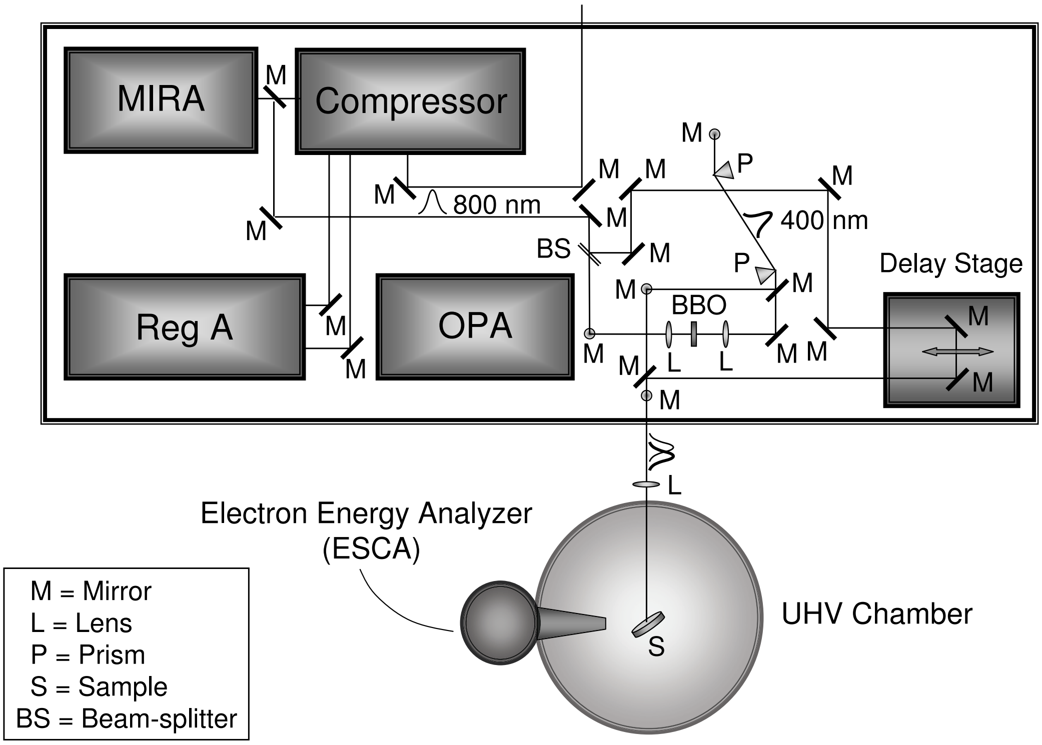

Figure 4.5: *The second 2PPE setup.*

times can not be determined. On the other hand, the *time difference*, Δt, between them (*delay*) can be easily measured. In a simple view, one can choose $t_{ob} = 0$ such that t_{or} becomes $\Delta t = t_{or} - t_{ob}$ (or vice-versa, depending which one plays the role of the pump pulse or choice upon experimental setup) without altering the generality of the result. In this way $N_D(t_{or}, t_{ob}) \equiv N_D(\Delta t)$ and the result can be directly compared with the experimental cross-correlation curves. Single channel excitation can be easily modeled by putting the condition $\alpha_{r,b} = 0$ for one of the intermediate states. If each single channel (only one intermediate state) is considered separately, then the two count rates yielded in the calculations are shifted on the delay time axis.

Unfortunately, since $N_D(\Delta t)$ is not an analytical function there can not be a simple fitting procedure for a cross-correlation curve. The easiest way is to compare the sum squared deviation along the time delay for a calculated N_D curve with respect to the experimental data[d]. In the figure 4.4 (left graph) there is given an example of how one can use this model to compute the total transient electron yield, N_D, for a system with one initial and one intermediate state, where a red pulse is the pump and the blue pulse is the probe. The most interesting result is that the peak of N_D curve shifts with respect to the zero delay as function of the intermediate state lifetime (fig. 4.4, right graph). Such effect was observed experimentally by Hertel *et al.* in ref. [4]. As a remark, the solution of the rate equation 4.3.13 is similar to the equation 5.4.3.

A more realistic model would make use of the fact that there exist at least two relaxation processes

---

[d] the curve $N_D(\Delta t)$ must be first centered on the maximum of the cross-correlation curve.

involved: first, the inelastic electron scattering leading to a population decay in the intermediate state via electron-hole pair creation in the substrate; second, the (quasi)-elastic scattering with phonons and defects which induces a decay of the coherence between the levels involved in the pump-probing [111]. Therefore, the intermediate state population decay is not described by only one exponential decay but by a sum of at least two exponential decays with different decay rates. However, for the system studied, a single exponential decay was basically sufficient to simulate the lifetime of an intermediate state.

4.4 Experimental Setup

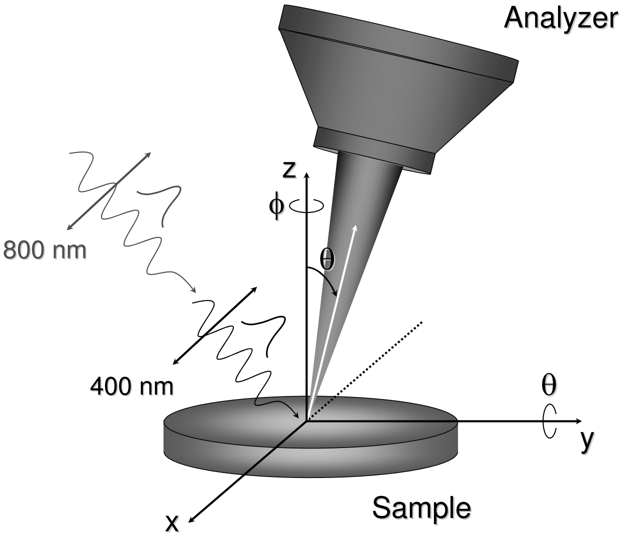

Figure 4.6: *2PPE geometry.*

The experiments were performed in an ultra-high vacuum (UHV) chamber equipped with a modified VG ESCALAB 220 (Vacuum Generators) electron spectrometer with nominal energy and angular resolution of 20 meV and 0.8°, respectively [112,113]. The samples are mounted on a two-axis goniometer which makes possible the measurement of a 2π solid angle. The UHV chamber contains also a low-energy electron diffraction (LEED) detector, several evaporation sources and a scanning tunneling microscope (STM) produced by Park Scientific Instruments (now ThermoMicroscopes) [114]. For 'classic' photoemission experiments three X-ray sources (Mg $K\alpha$, Si $K\alpha$ and Al $K\alpha$) and a monochromatised high-flux He discharge lamp (Gammadata VUV5000) are used. The laser system was presented in chapter 2.6.

The first 2PPE setup was constructed following a standard pump-probe configuration. The fundamental of the oscillator, with 790-800 nm wavelength, 'red', was frequency-doubled in a 0.5 mm thick $\beta-$bariumborate (BBO) crystal (43 meV spectral bandwidth) and the resulting beams were separated by a beam-splitter. The $\sim$400 nm ('blue') pulses were shot directly on the sample while the red pulses were temporally delayed by means of a delay stage. Both beams were focused with

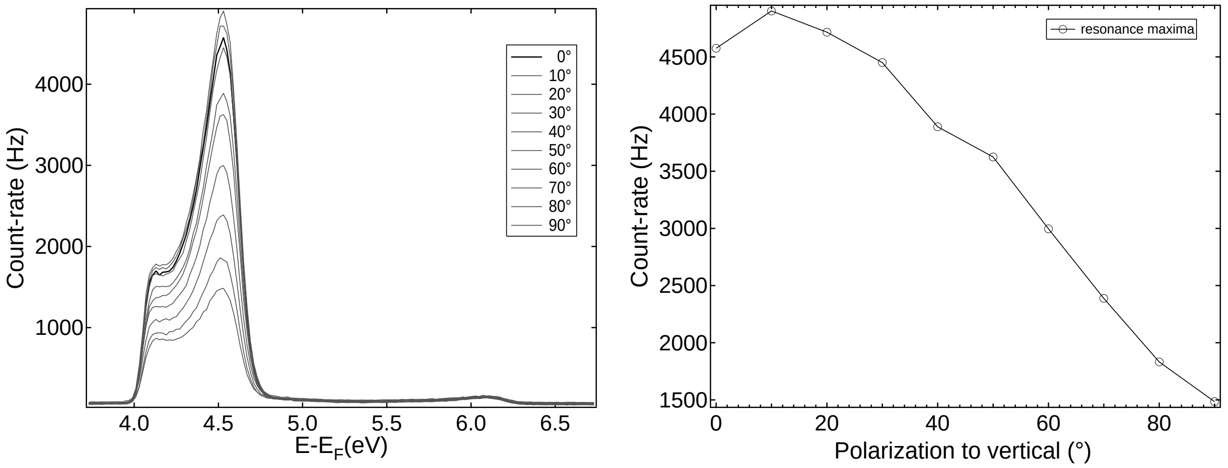

Figure 4.7: ***Left Graph**: Series of 2PPE spectra taken for h-BN/Rh(111) at coincidence of red and blue pulses. The blue pulses were p-polarized while the red pulse polarization was varied from s-* (90°) *to p-polarization* (0°)*.* ***Right Graph**: Maximum cross-correlation peak is observed at* 10° *with respect to the vertical direction. Actually, this corresponds to a p-polarized beam on the sample surface. In the experiments the angle* 0° *had been used which is* 10° *off a fully p-polarized beam.*

the help of a lens which was positioned such that the two spots had the same dimension at the sample surface, less than 0.1 mm. The red and the blue pulses reached energies of 2.1 and 0.4 nJ per pulse, respectively, on the surface. Also, in the red path there was a polarizer-rotator inserted in order to vary the polarization of the red photons. This setup was mainly used to check the dependence of the resonant features observed in the 2PPE spectra on the fundamental photon wavelength. The resulting red and blue pulses at the sample surface had quite long time widths of more than 200 fs, judging from the cross-correlation curves taken from a h-BN/Rh(111) sample.

In the second setup the fundamental of the Coherent MIRA oscillator, with 800 nm wavelength, 76 MHz repetition rate and 60 fs time duration (red pulse), was used as probe and its second harmonic (SHG, blue pulse), generated with a 0.5 mm thick BBO, was used as pump. The spectral bandwidth for the red and the blue pulses was measured to be 58 and 39 eV, respectively. The initial red beam is split into two identical beams by a 50% beam splitter (for p-polarized light). One of the two beams is used to produce the blue beam while the second is going over an in-house built delay stage in order to vary the pump-probe time delay on the sample. The blue pulses were pre-compressed in a prism compressor stage which contains two UV-fused silica prisms cut close to the Brewster angle such that the transmission losses are minimal. The setup such constructed has the advantage of preserving the red pulse quality as close to the oscillator output and the prism compressor can compensate for the chirp acquired by the blue pulse during its propagation (fig. 4.5). The down part is that the blue SHG beam has four times less power than in the first setup due to the half-half splitting of the red beam before the BBO. Experimentally, energies of about 0.1 nJ per blue pulse and 2 nJ per red pulse were measured at the sample surface. However, the pulses are about four times shorter by judging from the cross-correlation curves taken for a h-BN/Rh(111) [12] sample with the two setups. Both provided almost p-polarized beams on the sample for both pump

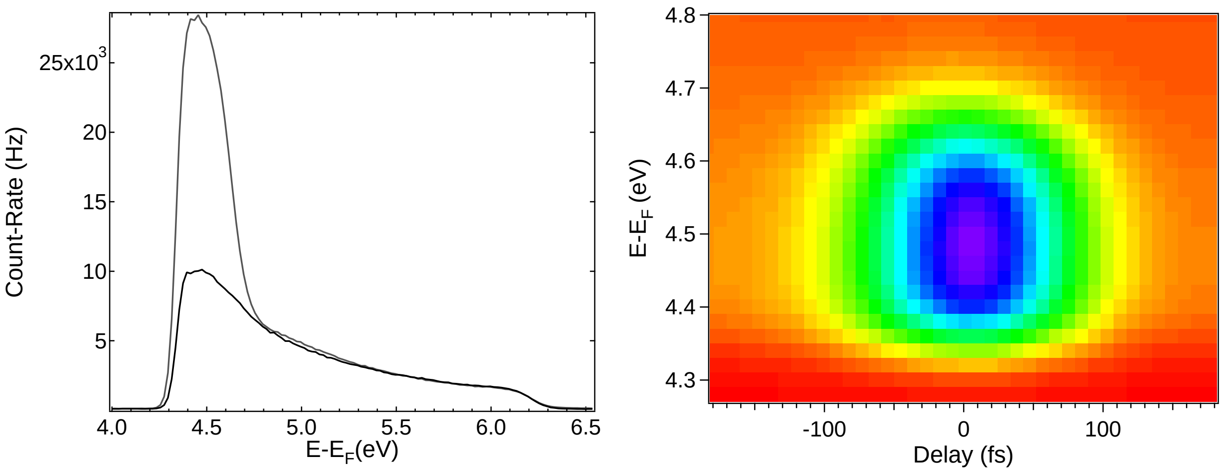

Figure 4.8: ***Left Graph**: In the first setup, the spectrum count rate increases 3 times when the Ag-poly surface is illuminated with red and blue pulses at coincidence (0-delay). **Right Graph**: Series of spectra along the time delay between the red and blue pulses, taken with the second setup, form a so-called spectra-time map or cross-correlation map. The energy is kept to the relevant range from* $3h\nu$ *to* Φ *provided by the two color 2PPE with* $h\nu = 1.5537\ eV$ *fundamental light quanta. Negative values of the time delay mean that the red pulses reach the sample before the blue ones (which fix the 0-delay).*

and probe pulses (fig. 4.7). The red beam polarization has been verified within the first setup such that it yielded the highest electron count rate. Actually, during the experiments, the polarizations used for the blue and red beams were 10° off from a pure p-polarization due to the fact that the geometry of the setup (fig. 4.6) near the entrance to the vacuum chamber was not allowing for a perfect p-polarization. Also, a polarizer-rotator device induces quite a large pulse broadening which does not compensate the minimal gain in electron count rate. The polarization dependence of the maximum CC curve for the h-BN/Rh(111) sample can be explained by the σ character of the initial state involved in the resonant pump-probing [111].

On both setups a bias voltage of -10.00 V was applied to the sample in order to avoid the low transmission region of the analyzer. The delay stage was built with an electric motor driven Newport ball bearing linear stage [44] which can vary the delay between the two pulses with 9.(259) fs increments.

4.5 2PPE on Systems with Virtual States

When performing time-resolved 2PPE experiments in situations without intermediate states, the cross-correlation curve is similar to the IAC of the pump and probe pulses involved. Under the assumption that the space charge and the surface plasmons produced by the two laser pulses are not sufficiently strong to influence the propagation of the photoelectrons to the electron energy analyzer, the time duration of the cross-correlation peak is equal to the time duration obtained in an IAC experiment [68]. One perfect candidate is the silver polycrystal (Ag-poly) surface which is known for not having surface states around the Fermi level (E_F). A clean silver polycrystal surface can also be used to find the Fermi level within an experimental setup.

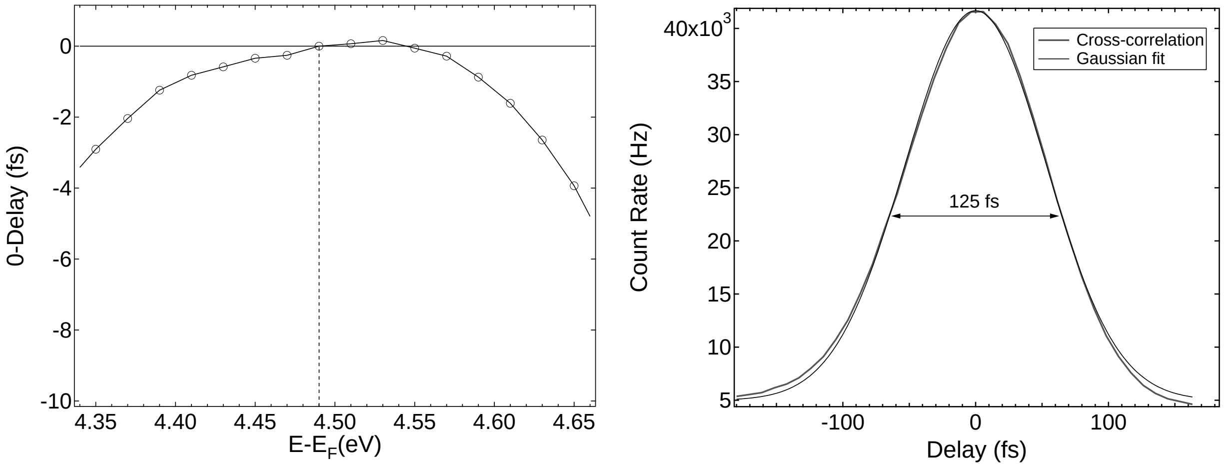

Figure 4.9: ***Left Graph****: The transients maxima variation along the relevant electron kinetic energy. The difference at the sides stays within 4 fs with respect to the overall observed transients maximum.* ***Right Graph****: The cross-correlation peak maximum observed at 4.49 eV final state energy has a duration of about 125 fs.*

The two setups were used to perform time-resolved 2PPE with fundamental red pulses (λ_o = 798 nm) on a clean Ag-poly surface. When red and blue pulses arrive at the same time at the surface (coincidence) one can observe that the intensity increases by about a factor of three at the maximum ($E - E_F = 4.49$ eV) and *uniformly* from $3h\nu$ to Φ energy range. The work function of the Ag-poly sample was measured to be about $\Phi = 4.35$ eV. The spectra-time map (fig. 4.8) shows that the cross-correlation curves are symmetric around the maximum peak observed at $E - E_F = 4.49$ eV (fig. 4.9). The transients maxima varied within 4 fs along the relevant kinetic energy with respect to the maximum of the spectrum. The time duration of the cross-correlation curve at the peak maximum was fitted at about 125 fs. This value can be attributed to an ICC of the red and blue pulses. Under the assumption that the two pulses have the same time duration it yields 88 fs. Since the time duration of one of the pulses is not precisely known it can be stated that the time duration of the 2PPE cross-correlation curve on the Ag-poly sample gives only an estimate of the experimental overall temporal resolution in the second setup. That is because a pump-probe experiment on a metallic surface is expected to yield the shortest possible cross-correlation curve, ideally equal to the ICC of the pulses involved.

Chapter 5

Ultrafast Electron Dynamics at Interfaces

5.1 The Hexagonal Boron Nitride Nanomesh (h-BN/Rh(111))

By exposing an atomically clean Rh(111) surface, which is kept at a temperature of 1070 K, to a borazine ($(HBNH)_3$) vapor pressure of 3×10^{-7} mbar inside an ultrahigh vacuum (UHV) chamber and consecutive cooling down to room temperature (RT) one can produce a highly regular mesh of hexagonal boron nitride (h-BN/RH(111)) [12]. This self-assembled so-called *nanomesh* presents 2 nm diameter holes with a 3.2 nm periodicity, as seen in the scanning tunneling microscopy (STM) images (fig. 5.1). The two formed boron nitride layers cover the surface uniformly, and they are offset in such way that minimum metallic area remains exposed. The lattice mismatch between the rhodium substrate and the boron nitride (BN) film is an important factor for the hole formation. Considering the hole periodicity (3.2 nm) one can define a surface reciprocal lattice constant of 0.227 Å^{-1}.

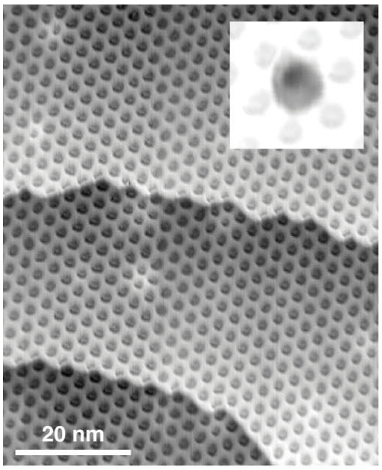

Figure 5.1: *STM large topographic view taken with -1 V bias voltage and 2.5 nA tunneling current.*

From the LEED patterns (fig. 5.2) one can confirm the hexagonal superstructure while from the

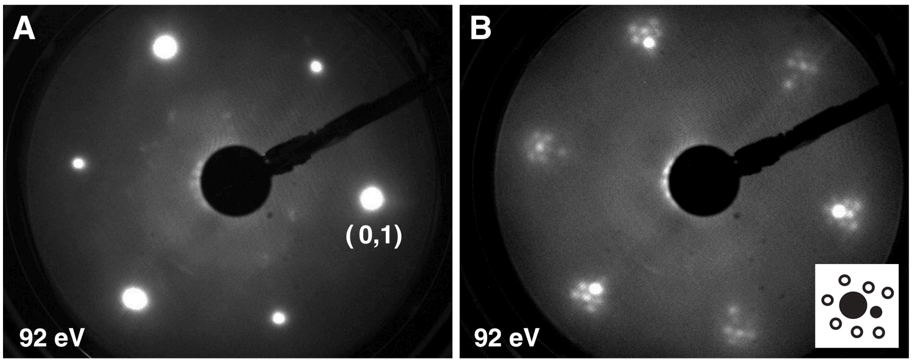

Figure 5.2: *A.) Rh(111) LEED pattern and B.) h-BN/Rh(111) LEED pattern with Rh(111) substrate spot (large filled circle), h-BN principal spot (small filled circle), and nanomesh superlattice spots (small open circles).*

doubling of the bands as observed in photoemission spectra (fig. 5.3) the boron nitride double layer structure is deduced. The ARUPS (fig. 5.4) dispersion for the nanomesh shows that the boron nitride does not contribute to the electronic band structure at binding energies lower than 4 eV. The surface resonance states of the Rh(111) surface present at 0.6 and 2.5 eV are strongly coupled with the bulk d-bands and seem to disappear after boron nitride deposition. Another surface resonance state, situated at 0.1 eV below the Fermi level, reported later for the Rh(111) has its existence still under debate [115]. Most probably any surface state from the Rh(111) surface vanishes upon the boron nitride deposition.

It is well known that the bulk boron nitride has insulating character with a band gap of about 5.2 eV [117]. Therefore, it can be assumed that the electronic band structure of the h-BN/Rh(111) interface has only the bulk rhodium contribution at binding energies below 4 eV. The boron nitride adds two σ bands and one π band, each of them split into two due to the double layer structure (fig. 5.3). The nanomesh has insulating behavior in the sense that there is no evidence for boron nitride bands crossing the Fermi level, so far.

5.2 2PPE on the h-BN/Rh(111) Nanomesh

Due to its insulating character and the very good thermal stability this regular nanostructure can become an interesting template for ordered supramolecular architectures. For further applications, it is necessary to investigate the conduction bands of this insulating bilayer. For this purpose the unoccupied band structure was mapped by means of two-photon photoemission [4,118,119]. Using the fundamental and the second harmonic of our femtosecond Ti:Sa laser, interface states can be populated and subsequently probed. Beside spectroscopic information, this method gives access to lifetimes of intermediate states and coherent excitation dynamics.

In both setups (see chapter 4.4), when illuminated with blue laser pulses (one-color 2PPE, blue-blue (BB)), the sample reveals photoemission spectra with quite low intensities (fig. 5.5, black spectra). The secondary electron peak ($E - E_F = 4.09$ eV) and a peak (C) situated at $E - E_F = 4.56$ eV final state energy display a strong increase (Fig. 5.5, gray spectrum, RB) when the red

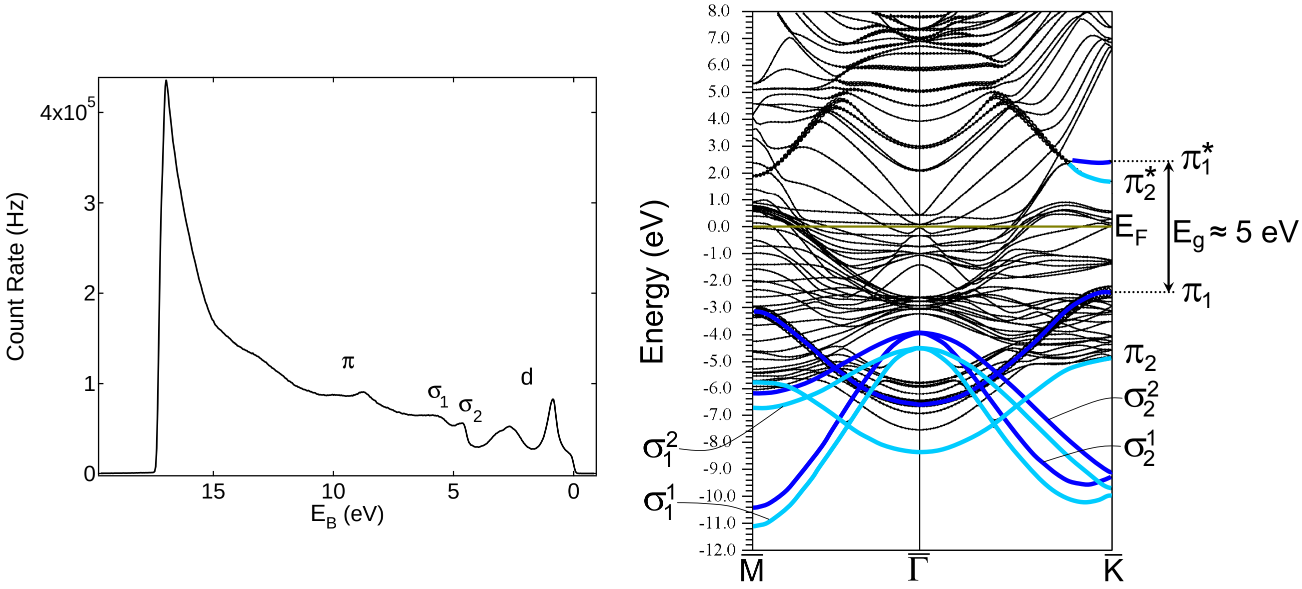

Figure 5.3: ***Left Graph**: UPS spectrum ($h\nu = 21.2$ eV, He Iα) of h-BN/Rh(111) at the $\bar{\Gamma}$ point (normal emission). The boron nitride overlayers add the two σ and the π bands around 5 and 10 eV binding energy. Two rhodium d-bands are visible at at 0.8 and 2.7 eV. **Right Graph**: Calculated band structure for a hypothetical double layer (1×1) h-BN on Rh(111) in the $\bar{\Gamma}\bar{\mathrm{K}}$ and $\bar{\Gamma}\bar{\mathrm{M}}$ directions [13]. The insulating band gap at $\bar{\mathrm{K}}$ point is about 5.3 eV.*

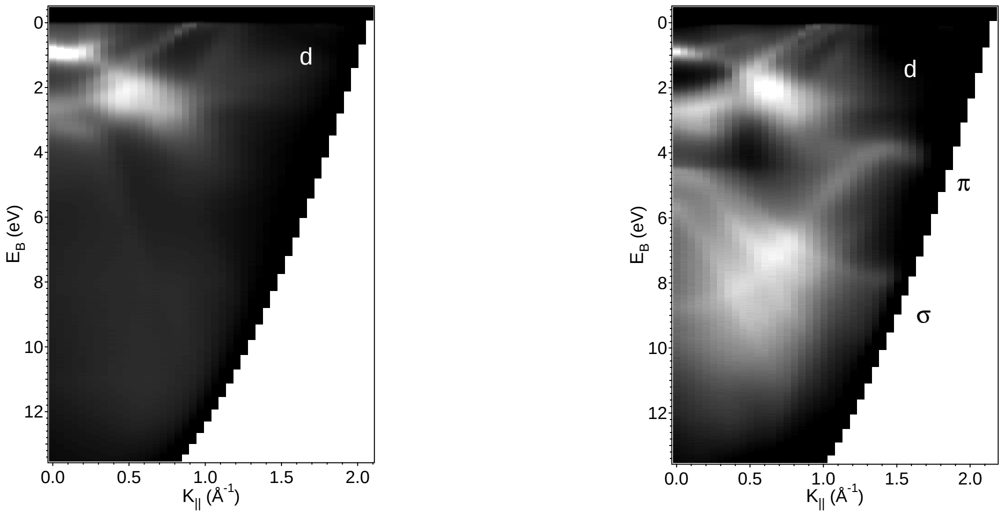

Figure 5.4: ***Left Graph**: ARUPS ($h\nu = 21.2$ eV, He Iα) dispersion data for a clean Rh(111) sample in the $\bar{\Gamma}\bar{\mathrm{M}}$ direction. **Right Graph**: ARUPS dispersion for the nanomesh in the same high-symmetry crystallographic direction. The boron nitride adds the $\sigma_{1,2}$ and π bands (above 4 eV binding energy) but does not induce any visible interface state around the Fermi level.*

and the blue pulses arrive on the sample at the same time (*i.e.* at coincidence or 0-delay). Each spectrum (BB or RB) presents three distinct features which we note A, B, C or A, B and D,

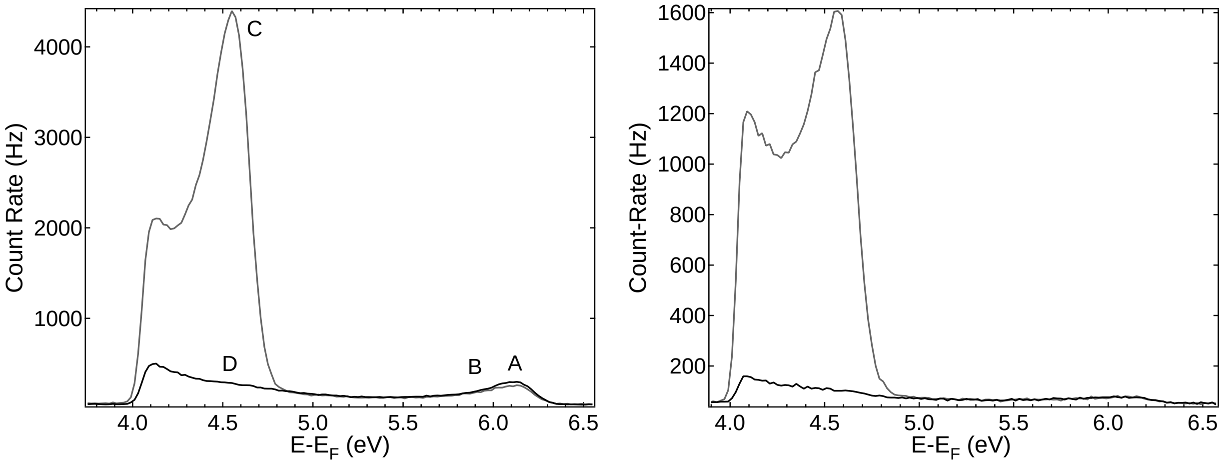

Figure 5.5: ***Left Graph**: Spectra at red plus blue coincidence (grey curve) and 2PPE with only blue pulses (BB) in the first setup. The fundamental wavelength is* $\lambda_o = 798$ *nm* ($h\nu = 1.554$ *eV). One can observe four features denoted A, B, C and D. The peaks A and C are much more prominent.* ***Right Graph**: Spectra at red plus blue coincidence (RB, grey curve) and at off-coincidence (black curve) in the second setup. The 2PPE spectrum with only the blue pulses looks very similar to the one at off-coincidence (black curve).*

depending on the spectrum involved (fig. 5.5). Naturally, the question arises as to what is the origin of these peaks. A first step is to assign the peaks A, B, C and D to initial (occupied) or intermediate (unoccupied) states by tracing their position as function of the fundamental photon energy. In case of initial or intermediate states, the peaks move with the sum of pump and probe photon energies or the probe photon energy only, respectively [118]. In our case, the fundamental wavelength was varied between 790 and 840 nm ($h\nu$ between 1.569 and 1.476 eV) and the resulting experimental peak maxima (peak C) were linearly fitted showing a slope very close to 3 (fig. 5.6, left graph). This means that the cross-correlation peak moves with 3 times the fundamental photon energy, *i.e.* it can be assigned to an initial state. By comparison, a hexagonal boron nitride (1×1) structure formed on Ni(111) (h-BN/Ni(111)) [122–126] reveals a slope of 1.28 when linearly fitting the peak C′ observed within similar experimental condition. Here, this resonant peak is likely to be caused by a contribution of two intermediate states, one of them, the conduction band, being identified in the density functional theory (DFT) calculations by Grad et al. [126]. The other band is considered to be the $n = 1$ image potential state.

The maximum kinetic energy which a photoelectron can have in the BB situation is $E_F^{bb} = 6.215$ eV while for the RB, $E_F^{rb} = 4.661$ eV. Since the peaks A and C lie very close to these values for the BB and RB situation, respectively, it is natural to assume that they originate from the same initial state. Indeed, the peak A moves with four times the fundamental photon energy which means that it belongs to an initial state (fig. 5.7, left graph). So it seems that the nanomesh 2PPE spectra are dominated by initial states. But can we rule out completely the existence of an intermediate (unoccupied) state which can be resonantly pump-probed within our setup (BB or RB)? The answer is no. A first indication that there may be some weak resonance involved is

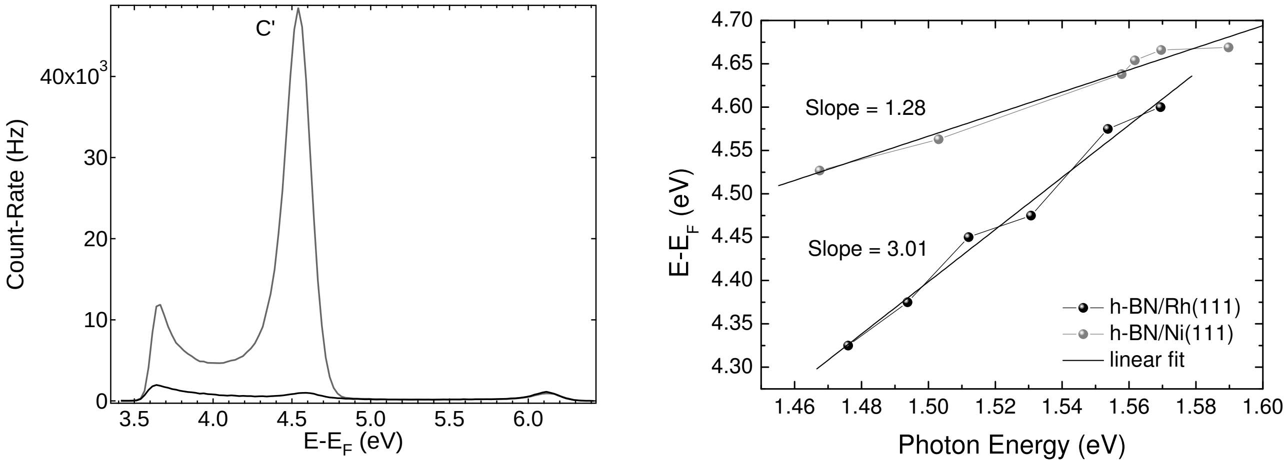

Figure 5.6: ***Left Graph***: *The h-BN/Ni(111) RB spectrum (λ_o = 798 nm fundamental photon wavelength, $h\nu$ = 1.554 eV) at coincidence presents a much stronger peak, C', than in the case of the nanomesh.* ***Right Graph***: *The peak C' from the h-BN/Ni(111) sample has a slope of 1.28 when traced as function of the fundamental photon energy while the peak C from the nanomesh has a slope of 3. Data for the h-BN/Ni(111) was taken from the reference [120] (see also [121]).*

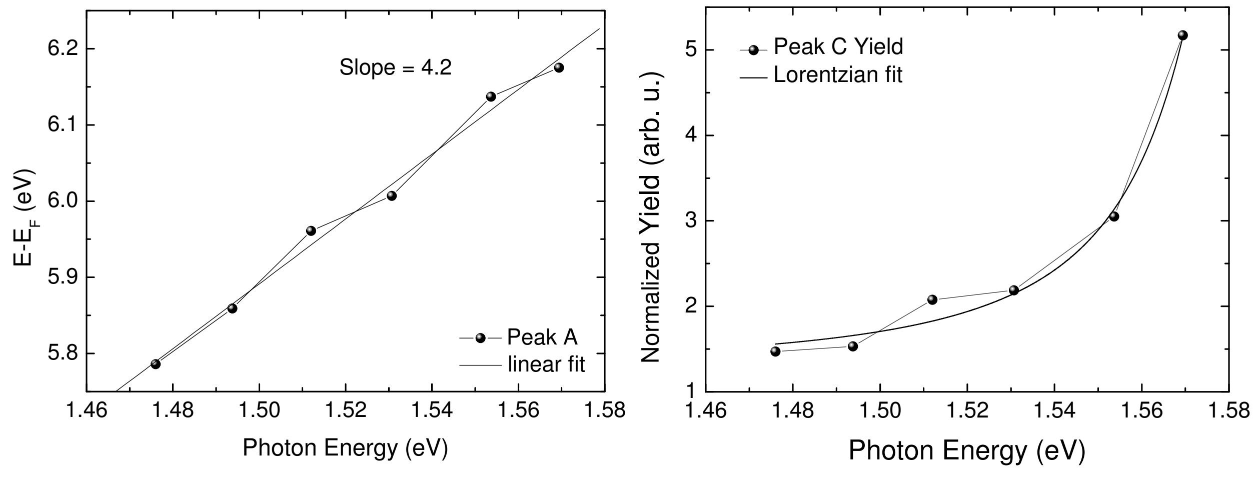

Figure 5.7: ***Left Graph***: *The peak A moves with four times the fundamental photon energy.* ***Right Graph***: *The normalized peak C electron yield increases with the fundamental photon energy.*

given by the normalized electron yield of the peak C which strongly increases with the fundamental photon energy. Assuming that there exists a photon energy close to $h\nu$ = 1.554 eV for which a perfect resonant pump-probing from an intermediate state is possible, one can think of fitting the normalized peak C electron yield[a] as function of photon energy with a Lorentzian (assuming, therefore, an optical resonance with Lorentzian shape). This is provided by the fact that the two bands involved in the process have Lorentzian-like lineshapes[b] (initial and intermediate). The fitted Lorentzian (fig. 5.7, right graph) is centered at 1.6 eV photon energy and has a FWHM $\Gamma = 24.3$ meV which is equivalent with a lifetime[c] $\tau = 27$ fs. So a fundamental pulse centered at $\lambda_o = 774.4$ nm[d] would be able to resonantly pump or probe an intermediate state with a linewidth less than 24.3 meV. The strong increase of the normalized peak C electron yield with the photon energy suggests that there exists at least one unoccupied intermediate state which one can resonantly pump-probe at higher fundamental photon energies than our optical setup can provide. Therefore, it can be stated that, at a pulse wavelength $\lambda_o = 800$ nm ($h\nu = 1.55$ eV), where most of the experiments have been performed, this intermediate state can only be *non-resonantly* excited.

In order to analyze the positions of the peaks A, B, C and D we fit the BB spectrum under the assumption that there are two states roughly at 0.6 and 0.1 eV below the Fermi level. Since the two states lie very close to the Fermi level, the fitting is done with a sum of two Lorentzians cut off by a Fermi function. Also, both the electron energy analyzer and the laser pulses contribute to the linewidth. It was shown that the red pulses have a bandwidth between 50 and 60 meV, the blue pulses around 40 meV. The analyzer has a resolution of about 30 meV.

Ideally, the Gaussian profiles of both pulse and analyzer contributions should be convoluted with the product between the Fermi function at RT and the sum of the two Lorentzians. But such a fitting procedure would be very time consuming and the results not far from a simpler one which assumes that the energy width of the laser pulses and analyzer are a part of the Fermi function and the Lorentzian widths. The actual effective surface temperature, T_{eff}, can then be calculated using an empirical formula[e]

$$4k_B T_{\text{eff}} = [(4k_B T)^2 + (\Delta E)^2]^{1/2} \tag{5.2.1}$$

which connects the actual experimental energy resolution to the RT Fermi function width and the total energy resolution of the analyzer and laser pulses ($\Delta E = [(\Delta E_{an})^2 + (\Delta E_{p1})^2 + (\Delta E_{p2})^2]^{1/2}$). Further, the spectral intensity at a certain energy is influenced by electrons with higher kinetic energy which were inelastically scattered. Therefore, in order to count only the intrinsic electron yield from a particular state, one has to subtract a background which is here taken as a second order polynomial in energy. In our case, since the bands are close to the Fermi level, the background vanishes at E_F. By applying this fitting concept to the BB spectrum within 1 eV below E_F one obtains the positions of the two states A and B at 6.2 and 5.63 eV final state energy ($E - E_F$), respectively (fig. 5.8, right graph), with 20 meV the binding energy of the peak A. The widths of the two peaks were fixed at 540 meV and the Fermi function edge width at about 40 meV in order

---

[a] the RB spectra at coincidence had the BB spectra subtracted in order to keep the real RB electron yield

[b] The convolution of two Lorentzians is a Lorentzian which has the FWHM equal with the sum of the FWHMa of the convoluted Lorentzians.

[c] $\tau(\text{fs}) \simeq 659.1/\Gamma(\text{meV})$

[d] $h\nu(\text{eV}) \simeq 1239.841717/\lambda(\text{nm})$

[e] $k_B = 0.08617342$ meV/K is the Boltzmann constant.

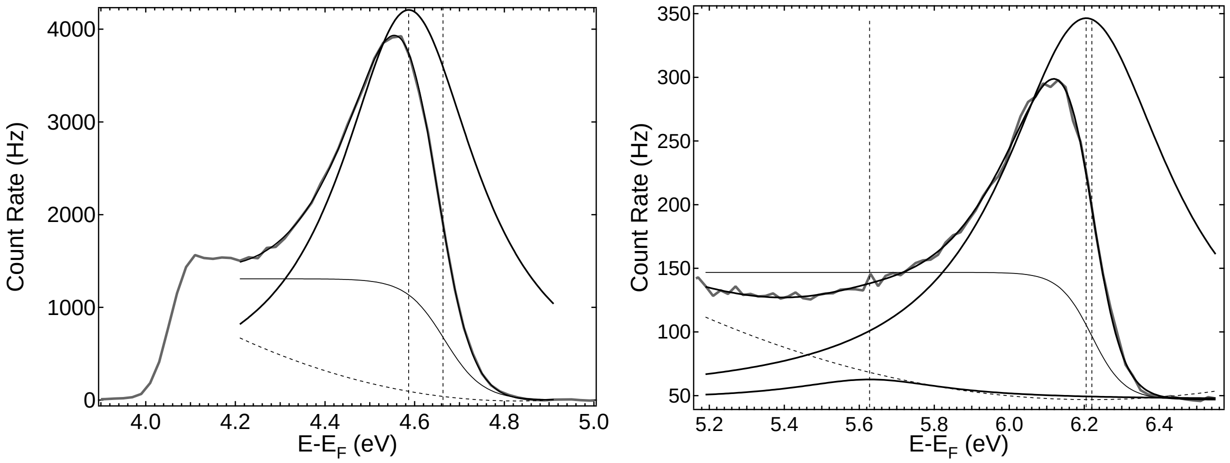

Figure 5.8: ***Left Graph**: Fits of the spectrum at coincidence RB (grey curve) after subtraction of the BB spectrum ($\lambda_o = 798$ nm, normal emission) in the first setup. The vertical dotted lines show the position of the Fermi level (red plus blue) E_F^{rb} and the center of the Lorentzian. The lower dotted line is the second order polynomial function which plays the role of the spectral background. **Right Graph**: Fits of the BB spectrum (grey curve) around the Fermi level. The vertical dotted lines indicate the two Lorentzians and the Fermi positions. The lower dotted line is also the second order polynomial background. The Lorentzians which enter the fit are shown with their actual intensity.*

to stabilize the fitting. Also, the Fermi level was fixed at the experimental value found from the BB spectra taken for a clean silver polycrystal ($E_F = 6.22$ eV).

For the RB spectrum near the coincidence one can fit with the product between the sum of a Lorentzian with the second order polynomial background and a Fermi function. The second Lorentzian is no longer needed as the coincidence peak is much more intense than the other features which may be around. First, the RB coincidence spectrum taken at the same fundamental pulse wavelength ($\lambda_o = 798$ nm or $h\nu = 1.554$ eV) has the BB spectrum subtracted in order to take into account only the electrons which are extracted exclusively by one red and one blue photon. The one-color 2PPE red-red (RR) spectrum can not be excited since the nanomesh work function was found to be 4.03 eV, and three-photon photoemission (3PPE) can be neglected at the fluence employed here. In this way, the second order polynomial background must vanish at the red plus blue Fermi level ($E_F^{rb} = 4.67$ eV). Within the above conditions, the fitting yields the position of the peak C at 4.59 eV final state energy while the actual spectrum maximum lies at 4.57 eV. The line-width of the band was found around 400 meV and the width of the Fermi edge about 40 meV. If an initial state is responsible for the coincidence peak then it should exist at around 80 meV binding energy, roughly in agreement with the upper band (peak A) found in the BB fitting.

There is also the possibility that there exist intermediate unoccupied states which are populated and excited by a red or a blue photon. Their positions should be around 1.48 and 3.03 eV above the Fermi level for a red-blue or blue-red channel, respectively. An energy level diagram is shown in the figure 5.12, right graph, where C^{int} is the hypothetical intermediate state at $E - E_F = 3.03$ eV (as it will be shown later only the blue pulses can be considered as pump). In the same figure, C^{int}_{res} ($E - E_F = 3.2$ eV) is the position of the electronic band which would be resonantly excited

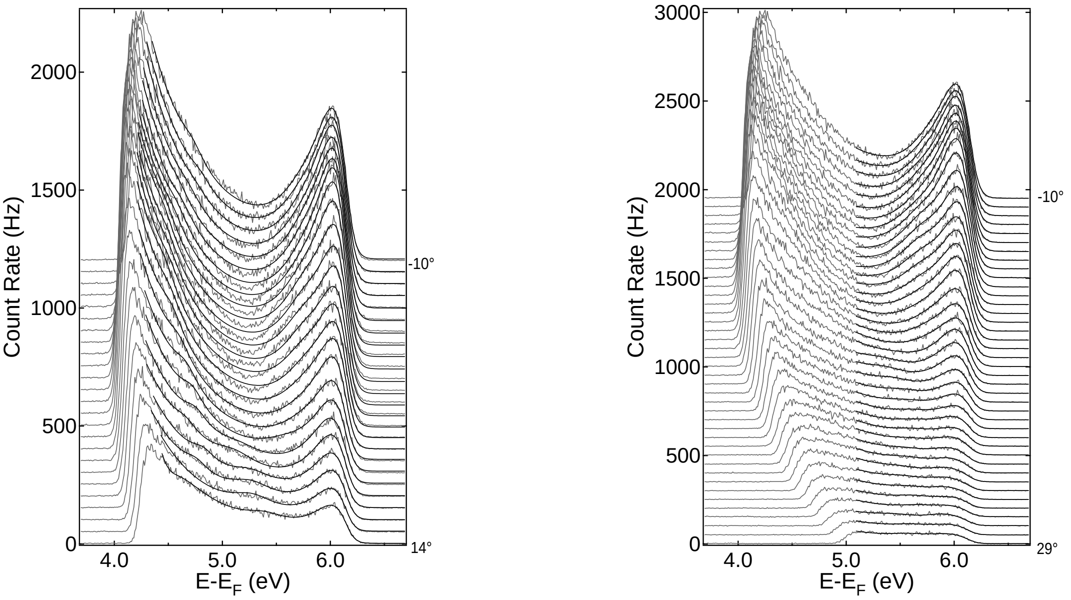

Figure 5.9: ***Left Graph**: Example of fitted angle-resolved 2PPE spectra for BB dispersion in* $\bar{\Gamma}\bar{\mathrm{M}}$ *direction* (λ_o = 800 *nm*, $h\nu = 1.55$ *eV) with three Lorentzians modulated by a Fermi function.* ***Right Graph**: Fitted angle-resolved 2PPE spectra only with two Lorentzians modulated by a Fermi function for the same BB dispersion. The two fits find almost the same dispersion for the bands A and B.*

with a fundamental photon energy of 1.6 eV (actually its second harmonic) from an initial state at 0.08 eV binding energy, as provided by the Lorentzian fit of the peak C normalized electron yield (fig. 5.7, right graph).

The BB dispersion map, in the $\bar{\Gamma}\bar{\mathrm{M}}$ direction (fig. 5.10), at central wavelength $\lambda_o = 800$ nm ($h\nu = 1.55$ eV) presents three features which can be observed up to 0.5 Å^{-1} in parallel momentum. The fitting procedure employed combines two fitting models, one with two Lorentzians plus a second order polynomial background multiplied by a Fermi function which yields the bands A and B with good precision and another one with three Lorentzians plus an exponential background modulated by a Fermi function which traces mainly the band D (fig. 5.9). The fits have a priori the constraints of 40 meV Fermi edge width and 540 meV line-width. The second model is actually able to find the bands A and B quite close to the values obtained with the first model. At $\bar{\Gamma}$, the binding energies of the bands A, B and D are 0.08, 0.49 and 1.68 eV, respectively (fig. 5.10). The first two are in good agreement with the previous fits on the normal emission spectrum analyzed before. The RB dispersion map, in the $\bar{\Gamma}\bar{\mathrm{M}}$ direction, at coincidence, taken in the same conditions as the BB dispersion map, presents a dominant peak, C, which can be fitted with a single Lorentzian, with a second order polynomial background, modulated by a Fermi function.

Since in time-resolved 2PPE the peaks are not necessarily originating from initial states, the *final state* ($E - E_F$) energy representation is the most convenient [5,128]. The bands A, B, D and C at $\bar{\Gamma}$ have final states energies of 6.14, 5.73, 4.53 and 4.61 eV, respectively. On the other hand, the peak C comes from a RB resonant excitation which means that in case an initial state is responsible, it

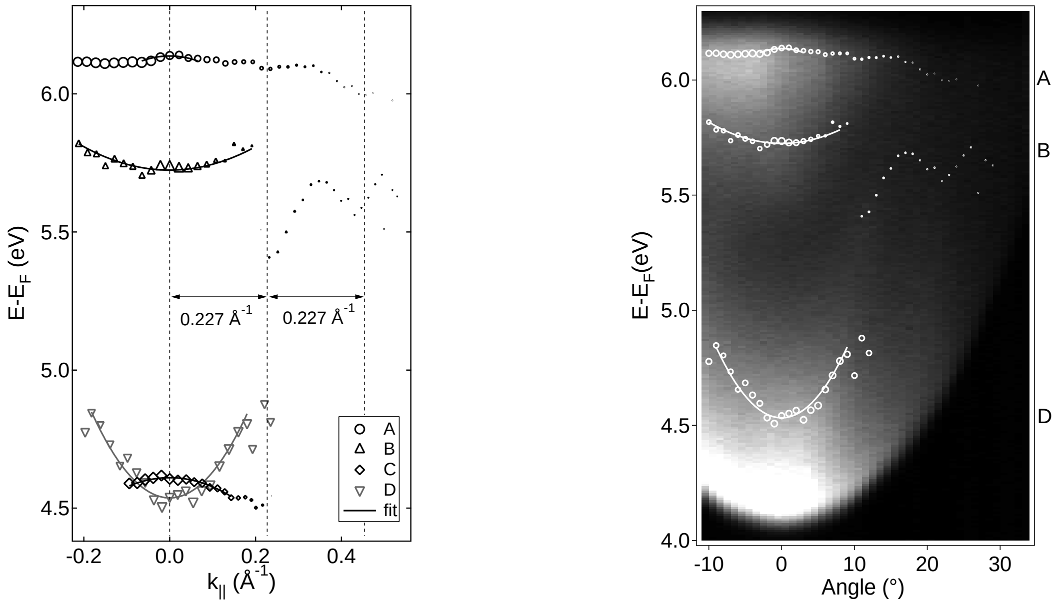

Figure 5.10: ***Left Graph**: The three bands A, B and D are traced quite well by the two fitting procedures ($\lambda_o = 800$ nm, $h\nu = 1.55$ eV). At higher polar angles the peak B finds one band which may be connected to the band D. The band C, obtained from the dispersion in the $\bar{\Gamma}\bar{M}$ at RB coincidence (fig. 5.11), is appended as a guideline. **Right Graph**: The BB dispersion map together with the bands positions.*

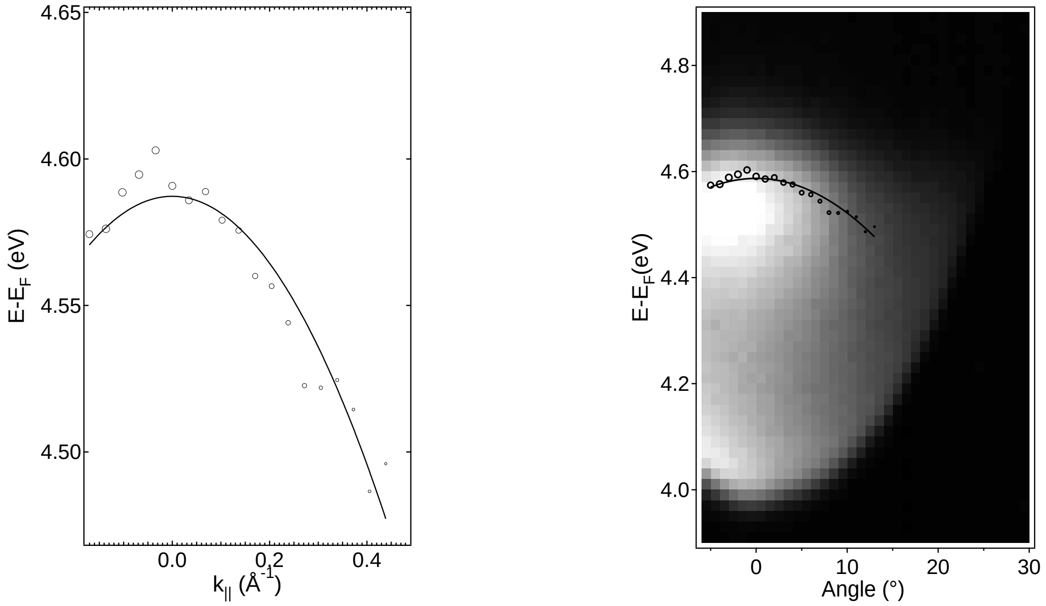

Figure 5.11: ***Left Graph**: The band C is resolved by the single Lorentzian fitting procedures (fig. 5.12, left graph). **Right Graph**: The RB at coincidence dispersion map together with the band positions.*

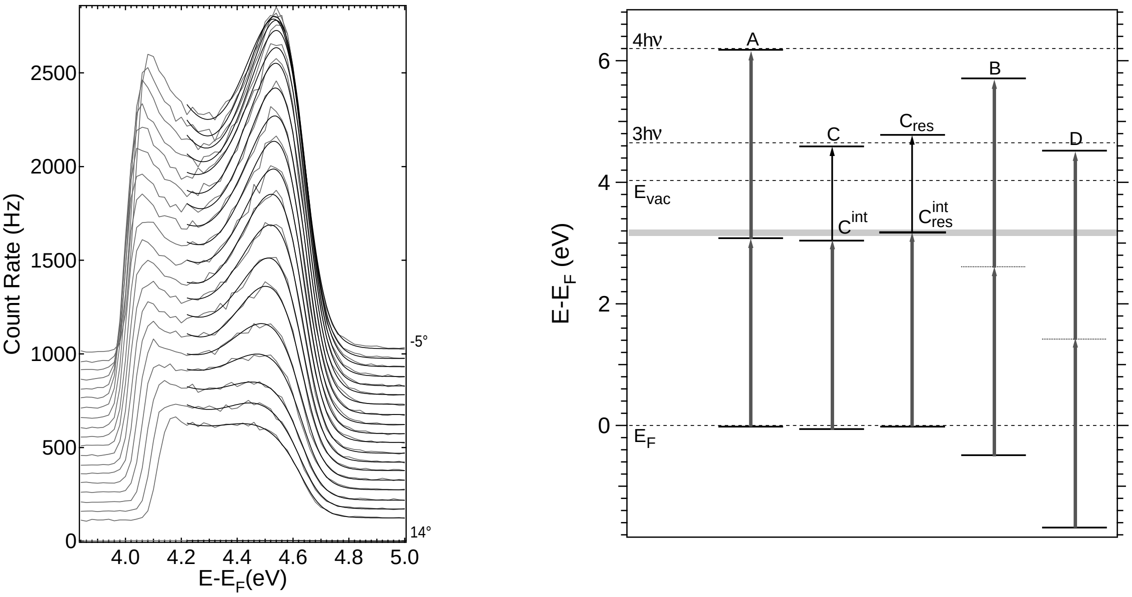

Figure 5.12: ***Left Graph**: Example of the cross-correlation peak fit with a single Lorentzian modulated by a Fermi function procedure for several ADC. **Right Graph**: The electronic energy level diagram. The thicker arrows represent the blue photons while the thinner ones are the red photons involved in the transitions.*

would exist at 0.056 eV binding energy. In direct comparison with the peak A ($E_B = 0.08$ eV), one can think this is a good indication that the RB coincident excitation originates from an initial state at $E_B \simeq 0.08$ eV. However, there are indications of a weak resonance which is pump-probed within our setup.

In the BB situation, when putting the dispersion results together, one can extract the electron effective mass and the band position at $\bar{\Gamma}$ for each of the three bands. The fits show that the peaks B and D have positive effective masses (1.8 m_e and 0.4 m_e, respectively) while A negative (-0.9 m_e). Furthermore, in figure 5.11 one can observe that the peak C disperses similar to the band A (downwards). Its binding energy is 0.056 eV and the absolute value of its effective electron mass (-1.2 m_e) is quite close to the one of the band A which shows that the peaks A and C are likely originating from the same initial band. The slight difference can be explained by the different photon energy used to excite the electrons in the two cases (BB, $h\nu_{\mathrm{BB}} = 6.22$ eV and RB, $h\nu_{\mathrm{RB}} = 4.66$ eV). From the solid state theory [127] it is well known that when fitting the dispersion of E_{kin} with a second order polynom $\alpha_o + \alpha_1 k_{||} + \alpha_2 k_{||}^2$ (with $\alpha_1 = 0$ for an extremum at $\bar{\Gamma}$), the effective mass $m_e^\star = \hbar^{-2}\partial_{k_{||}} E_{kin} = (3.81/\alpha_2) \cdot m_e$, so the coefficient of $k_{||}^2$ which gives the dispersion curvature is inversely proportional to the effective mass.

To make things clearer we employed the bulk rhodium calculations from reference [116] (fig. 5.13). For very low photon energies (like BB or RB, with $h\nu_{BB} = 6.2$ eV and $h\nu_{RB} = 4.66$ eV, respectively), the maximum perpendicular momentum in normal emission is close to the L point of the reciprocal space[f], while for He Iα is close to the Γ point. For a Rh(111) sample ΓL = 1.43 Å^{-1}.

---

[f] For a fcc lattice the ΓL direction in the reciprocal space corresponds to the normal to the (111) plane.

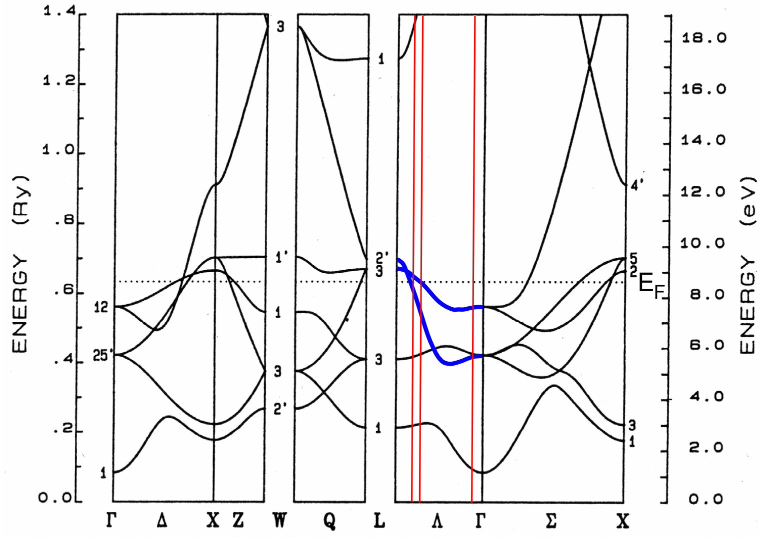

Figure 5.13: *The bulk rhodium band structure as calculated in reference [116]. The red vertical lines represent, in order, from the L point, the maximum perpendicular momentum acquired by an electron excited with RB, BB and He Iα photon energies at normal emission, respectively, represented in the first Brillouin zone.*

By taking the inner potential $V_o = 10.5$ eV [116, 129] and knowing that the binding energy of the initial state which would be responsible for the peaks A and C is about 80 meV, one can compute the maximum perpendicular momenta of a photoelectron excited with the RB or BB photons within the free electron final state approximation. The maximum perpendicular momenta for RB, BB and He Iα are 1.7, 1.82 and 2.69 $\mathring{A}^{-1}$, respectively. These values are marked by the red vertical lines in the figure 5.13, in this order, from the L point. The BB photons can excite electrons from a d-like band at 0.08 eV binding energy while the RB photons probe another band at 0.2 eV binding energy. This values are in good agreement with our observations on the behavior of the peaks A and C. However, these findings suggest that the peaks A and C do not originate from the same initial band. This can also explain why the curvature of the peak C dispersion is smaller than the curvature of the peak A. Looking at the line denoting the momentum of the BB initial state (fig. 5.13), one can observe that it crosses the second band at 1.7 eV binding energy. This value matches almost perfectly the binding energy found for a band which would yield the peak D (fig. 5.10, right graph). However, the peak B can not be identified in the calculations. One possibility is that, being quite small, it is only an artefact from the fitting procedure. With He Iα, the electrons can be excited from 3 bands at 1, 2.8 and 2.9 eV binding energy, in very good agreement with the UPS dispersion maps shown in the figure 5.4.

As a conclusion, the facts presented so far suggest that the peaks A and C originate from two different rhodium bulk bands.

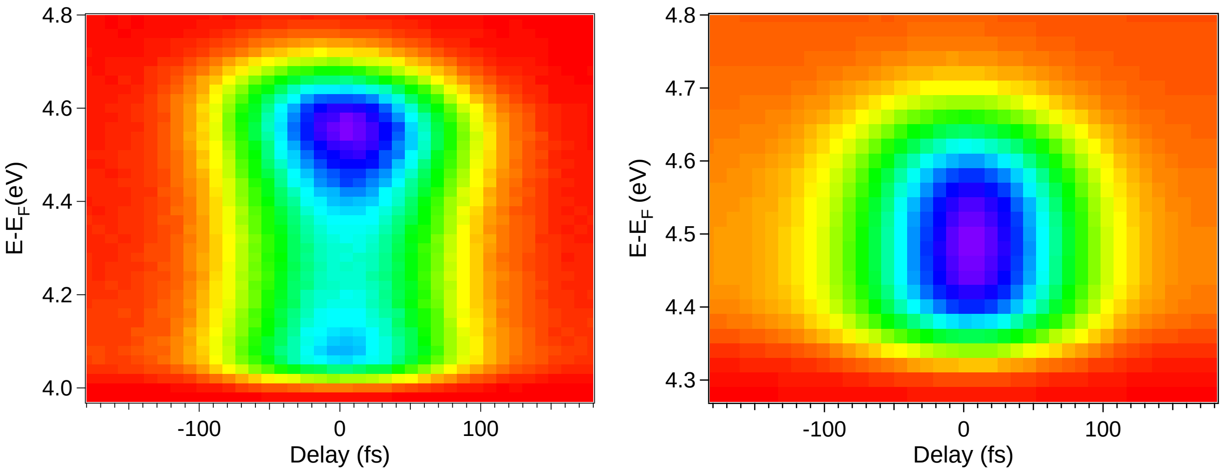

Figure 5.14: ***Left Graph**: Series of nanomesh spectra recorded along the time delay (of the red pulses with respect to the blue pulses) which form a so-called spectra-time map. The energy is kept to the relevant range (up to* $3h\nu$*) provided by the two-color 2PPE with* $h\nu = 1.55$ *eV fundamental light quanta. Negative values of the time delay mean that the red pulses hit the sample before the blue ones (which fix the 0-delay).* ***Right Graph**: The silver polycrystal spectra time-map is quite symmetric around the 0-delay with respect to the nanomesh spectra-time map.*

5.3 Existence of Intermediate States

Time-resolved 2PPE can provide valuable information about lifetimes of intermediate unoccupied states in the assumption that they exist. In the case of the nanomesh recent calculations [130] suggest that the boron nitride overlayer induces a rich band structure between E_F and the vacuum level. Also, band structure calculations (fig. 5.13) predict the existence of two unoccupied Rhodium bulk bands around the L point at about 0.8 and 0.5 eV above the Fermi level [116]. In the time-resolved RB experiment taken in the second setup (see chapter 4.4) the transient nanomesh total electron yield presented a time duration of 129 fs (fig. 5.15). Experimentally, the first indication that there may be an intermediate state which is resonantly pumped and probed arises from the comparison between the cross-correlation (CC) curves for nanomesh and clean silver polycrystal (fig. 5.14) taken under identical experimental conditions. For the later, the maximum CC peak was found at 4.49 eV final state energy and its time width (*i.e.* the temporal resolution) of about 124 fs was related to an Intensity Cross-Correlation (ICC) function which, however, can only provide an upper limit for the time duration of the correlated red and blue pulses. When looking at the differences between the CC maps of the Ag-poly and nanomesh, one can observe that there is a slight asymmetry of the nanomesh CC map around the maximum. Moreover, the direct comparison between the two maxima shows that the CC peak of the silver polycrystal is about 5 fs (FWHM) shorter than the CC of the nanomesh (fig. 5.15). Generally, it is observed that the transients on the Ag-poly are always shorter in the relevant energy range for the two samples (fig. 5.16). This suggests that, in the 2PPE process on the nanomesh, the simple ICC of the two pulses is accompanied by another effect which prolongs the transients.

In spite of the strong indication for a nonexistent intermediate state (at least not available for

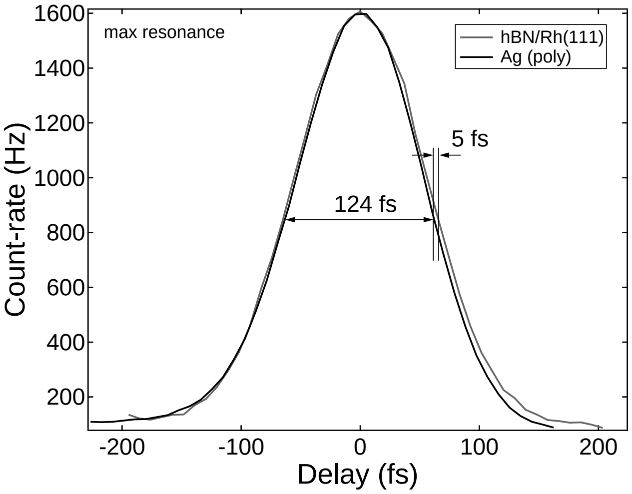

Figure 5.15: *The transient maximum cross-correlation curve for the nanomesh (gray curve) and from a silver polycrystalline sample within the same pump-probe conditions. The two curves are centered on their maxima (0-delay). The time duration of the nanomesh excitation is 129 fs, which is 5 fs longer than the one of the Ag polycrystal. Negative values along the delay mean that the red pulses arrive before the blue pulses at the sample surface.*

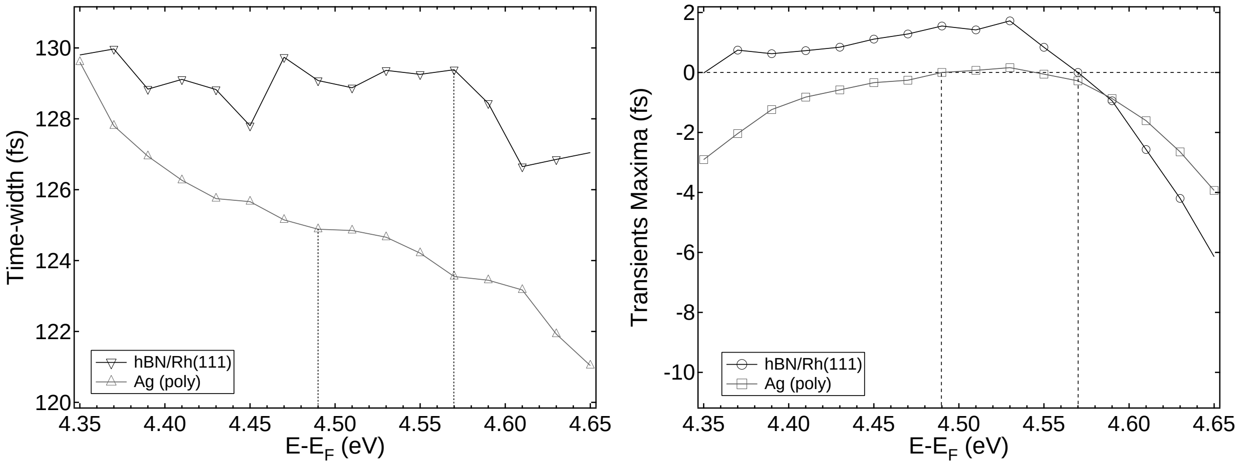

Figure 5.16: ***Left Graph**: The time duration of the cross-correlation curve for the nanomesh is always longer than for the Ag polycrystal in the relevant kinetic energy range. The silver sample has a work function of 4.36 eV, the nanomesh one of 4.035 eV. The two vertical dotted lines mark the maximum cross-correlation peak position for the two samples **Right Graph**: The transients maxima as function of kinetic energy for nanomesh and silver polycrystal.*

resonant pump-probing with the photon quanta at hand) due to the factor 3 dependence of the peak C on the fundamental photon energy, the asymmetry of the nanomesh CC map raises several questions regarding the origin of this peak. First, the existence of a nanomesh initial state around 0.1 eV binding energy is demonstrated by comparing the BB and the RB spectra at coincidence. As the RB spectra near coincidence present a *nonuniform*[g] increase in the electron energy range[h] from E_F^{rb} to Φ_{nm}, the clear peak appearing can only be related to an electronic state, either occupied or unoccupied. Second, the time width of the nanomesh CC peak is longer than the CC widths of Ag-poly. Surely, this situation can be explained by assuming that virtual hot electrons thermalize in a slightly shorter time than for the nanomesh around the Fermi level. However, since the Ag-poly CC map is symmetric around the 0-delay one can easily confirm that the asymmetry of the nanomesh CC map is not a result of some unknown chirp of the laser pulses. A coherent pump-probe excitation of a surface is done by exciting electrons directly into the final state. This can happen only if there is no intermediate state available for resonant pump-probing. By contrary, an incoherent excitation makes use of an intermediate state lifetime, thus producing a real hot electron distribution [128]. These electrons can decay by electron-electron (e-e, inelastic) and electron-phonon (e-p, elastic) scattering or be detected by absorbing another photon. Therefore, it can be stated that the existence of an intermediate state implies that the time duration of the CC curve is longer than the CC duration of a system without intermediate states. Since Ag-poly is metallic there should exist a continuous unoccupied band structure above the Fermi level, provided by the silver bulk band structure projected onto the surface. Therefore, the transients at different electron kinetic energies should have their maxima at perfectly equal delay times (0-delay), as it can be considered that the lifetimes of the photoelectrons in the unoccupied region is the same for a small energy variation. However, these maxima were found to move slightly (within 4 fs) around the energy of the maximum transient curve observed. On the other hand, the nanomesh transients

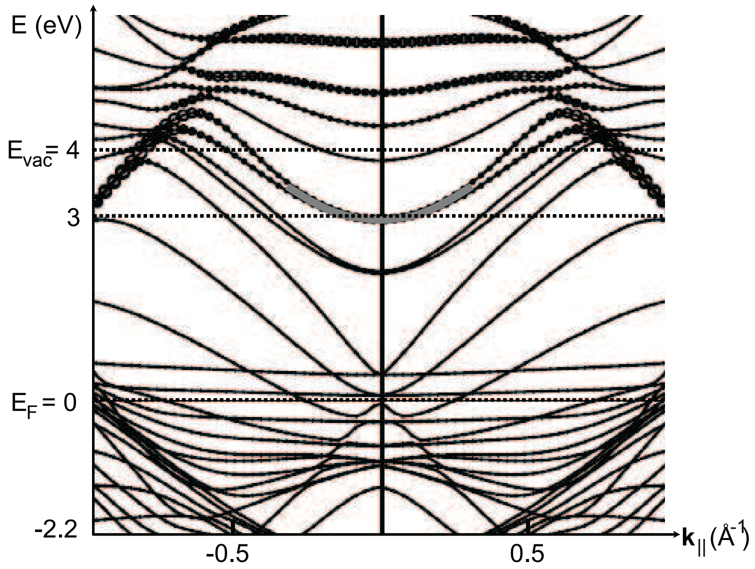

Figure 5.17: *The DFT calculations in $\bar{\Gamma}\bar{\text{M}}$ direction of a system consisting of 7 layers of Rh(111) between 4 layers of BN (2 on each side).*

---

[g] a sample with no initial and intermediate states should yield a RB spectrum at coincidence which adds up in the range $E_F^{rb} - E_{vac}$ uniformly to the BB spectrum, as in the case of the Ag-poly

[h] Φ_{nm} is the work function of the nanomesh, measured at 4.03 eV

maxima present a clear asymmetry around a similar transient map maximum. Comparing the Ag-poly and nanomesh results, one can sustain the hypothesis that the nanomesh possesses at least one intermediate state which can be resonantly pump and probed by the photons involved. The final argument in favor of the existence of the intermediate state is the DFT calculation [130] of a slab consisting of 7 Rh(111) layers and 4 BN-layers (2 on each side of the Rh), separated by a vacuum region (fig. 5.17). The occupied π and σ bands of the nanomesh are well related to this calculations which also predict the existence of 2 unoccupied bands at about 3 eV above E_F, exactly where the resonant blue-red (BR) pump-probing can be performed. Also, when looking at the figure 5.15, one can observe that the slight asymmetry of the nanomesh transient curve is appearing only for delays where the blue pulses arrive before the red pulses at the sample surface. This suggests that there exists an intermediate state which can be *nonresonantly* pumped by a blue pulse and subsequently probed by a red one.

5.4 Nanomesh Ultrafast Interface Quasiparticle Dynamics

Even though there exists quite a strong argument against the resonant pumping of an intermediate state (factor of 3 linear dependence of the CC peak maximum with the fundamental photon energy) one can still consider the off-resonant pumping of an intermediate state as a possible situation. With this assumption calculations provided by the simple model presented in section 4.3 lead to a best set of values for the blue and red pulses as well as for the lifetime of the involved unoccupied state.

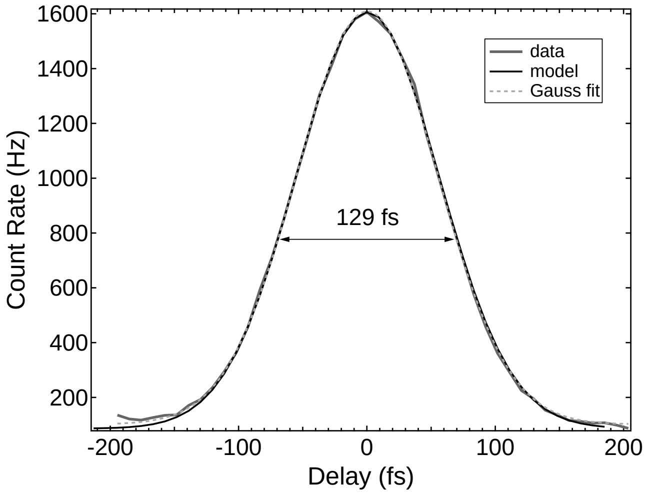

Figure 5.18: *Calculations show that the simple model introduced in the section 4.3 fits better the CC curve than a Gaussian. The data is taken in the experimental conditions of the second setup (see chapter 4.4) from a fresh prepared nanomesh.*

Since the DFT calculations predict two very close unoccupied bands around 3 eV above E_F at $\bar{\Gamma}$ one should consider the model only with the blue pulse as initial excitation and red pulse as probe.

The instantaneous electron density is then simply

$$N_{ext}(t, t_{or}, t_{ob}) \propto \alpha_b \exp\left[-\frac{(t-t_{or})^2}{\sigma_r}\right] \int_{-\infty}^{t} dt_o \exp\left[-\frac{(t_o-t_{ob})^2}{\sigma_b} - \frac{(t-t_o)}{\gamma_b}\right] \tag{5.4.2}$$

and the detector signal follows

$$N_D(t_{or}, t_{ob}) \propto f \int_{-\infty}^{+\infty} dt\, N_{ext}(t, t_{or}, t_{ob}) \tag{5.4.3}$$

where f is the pulse repetition rate (80 MHz for MIRA) and the subscripts 'r' and 'b' refer to the red and blue pulses respectively. The fittings were done by minimizing the vertical mean square deviation for different input values of the parameters involved. The calculated curve was centered on the maximum of the CC data curve while keeping identical number of points in order to produce a viable variation in the given interval of time. In this way the surface minimum of the parameters was found. The model has been applied for the nanomesh data taken with the second setup. The fit finds the best values at $\overline{\Delta t_r} = 97$ fs, $\overline{\Delta t_b} = 85$ fs for the red and blue pulses, respectively, and $\gamma_b = 10$ fs for the lifetime of the unoccupied state. The Gaussian which fits well the data has a temporal width of 129.3 fs while the ICC's width, formed with the two pulses $\overline{\Delta t}_{ICC} = (\overline{\Delta t}_r^2 + \overline{\Delta t}_b^2)^{1/2} = 129$ fs. The difference is close to zero which means that the lifetime of the assumed unoccupied state does not have a great influence in the resonant process. However, typical e-e decays (inelastic scattering) in such fast photoemission processes are of the order of 10 fs close to the Fermi level [5]. Therefore, it can be very well possible that a real intermediate state actually does exist in the BR case.

Moreover, a fitting series with two intermediate states (blue-red and red-blue) resulted in a larger minimum mean square deviation as in the case of the single intermediate state (blue-red), confirming the existence of only one intermediate state at around 3 eV above the Fermi level.

5.5 Conclusions

The results indicate that, within our setup, the peaks which appear in the 2PPE spectra originate from initial states. Comparison with bulk rhodium band structure calculations (fig. 5.13) suggest that in the BB and RB situations the peaks A and C originate from two different states very close to the Fermi level. Also, the peak D is found in very good agreement with these calculations.

However, a comparison with the t-2PPE data for the silver polycrystal indicates that there may be an interface state involved in the 2PPE process, due to the fact that the transient intensity is asymmetric around its maximum in contrast to the symmetric cross-correlation curve obtained from polycrystalline silver. Also, the time width of the transients for the nanomesh are clearly larger than the ones of the Ag-poly over the relevant kinetic energy. This suggests that in the RB situation the photons (red or blue) are non-resonantly exciting an unoccupied intermediate state. DFT calculations of a slab consisting of 7 Rh(111) layers and 4 BN-layers (2 on each side of the Rh), all separated by vacuum regions, confirm the existence of an interface state at 3 eV above the

Fermi level which can be non-resonantly excited within our setup (fig. 5.17). Also, the electron yield of peak C displays a strong increase with the fundamental photon energy which suggests that there exists a sharp (under 24 meV linewidth) unoccupied state which can be resonantly excited if the fundamental photon quanta is increased to 1.6 eV. This state should exist either around 3.2 eV above the Fermi level (if we consider the initial excitation from the Fermi sea close to the Fermi level) or 2.8 eV above the Fermi level (if we consider the initial excitation from a bulk rhodium band close to the Fermi level, as implied by the use of the 1.6 eV photon quanta in the calculations shown in figure 5.13). Our calculations involving a 2PPE model similar to a rate equation, give evidence that this unoccupied state should have a lifetime greater than 10 fs.

These findings are remarkably different to with the results for the h-BN/Ni(111) system, where resonant excitation into two intermediate states for RB and BR 2PPE processes appear to be relevant. Since initial states from the underlying metal bulk states seem to be involved in both cases, this different behavior arises most likely due to the different bulk band structures and the different energetic positions of the unoccupied h-BN conduction band states. This result is intriguing because He Iα-excited photoemission spectra are quite similar apart from the doubling of the bands. Further 2PPE experiments over a wider range of photon energies will be required in order to reveal the complete conduction band structure of the boron nitride nanomesh.

Chapter 6

Time-Resolved LEED (t-LEED)

6.1 Low-Energy Electron Diffraction (LEED)

Low-Energy Electron Diffraction (LEED) is a well implemented method for probing the periodicity of surfaces [131]. In principle, when electrons with energies up to several hundreds of eV coming from an electron gun hit a surface with periodic arrangement of atoms, they are partially diffracted in the backwards direction. From the latter, if only the elastically scattered electrons are collected on a fluorescent screen, a so-called LEED pattern will emerge. It is shown that this diffraction pattern images the reciprocal space[a] of the well ordered surface upon investigation [132]. As in X-ray diffraction, the constructive interference happens only when the momentum change $\Delta\mathbf{k} = \mathbf{k} - \mathbf{k}_0$ matches a reciprocal lattice vector $\mathbf{G}$ (*Laue* condition). The directions of the elastically scattered electrons can be found with the construction of the Ewald sphere (fig. 6.1). For a given momentum $\mathbf{k}_0$ of the impinging electrons normal to an ordered surface, the momentum transfer in the surface plane can only take discrete values which must be equal to a surface reciprocal vector $G_{||}$. The direction of the elastically backscattered momentum can be found by intersecting the Ewald sphere with the surface reciprocal lattice extended in three dimensions[b].

The LEED pattern of a well-ordered surface consists of spots with different intensities produced by the diffracted electrons. It can provide information about the periodicity of the surface lattice but not directly about the atomic arrangement. The actual positions of the atoms inside the unit cell can be determined by dynamical LEED which yields the so-called I(V) curves for the intensity of a given Bragg spot as a function of the electron energy. These curves are then compared with the scattering calculations for different model structures [8]. One other aspect of LEED is the temperature effect on the intensity of the Bragg spots. It is shown that thermal vibrations of the scatterers lead to an attenuation of the scattered amplitude of an electron beam. In other words, the intensity of the Bragg spots depends on the temperature of the surface under investigation. This phenomenon is also known as the *Debye-Waller effect* [133]. Mathematically, the diffracted

---

[a] The LEED pattern displays diffraction *Bragg* spots and represents the Fourier transform of the surface which produced it.

[b] It consists of vertical rods which originate in the actual two-dimensional surface reciprocal lattice vectors.

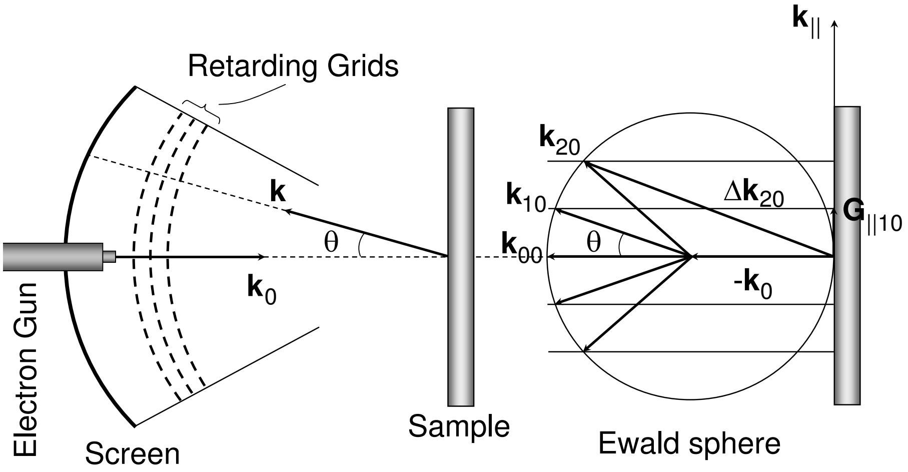

Figure 6.1: *The LEED setup together with the corresponding Ewald construction.*

beam intensity from a lattice at temperature T has the form

$$I(T) = I_o\, e^{-2M(T)} \tag{6.1.1}$$

where I_o is the spot intensitiy of a rigid lattice and

$$M(T) = \frac{6h^2}{m\,k_B} \cdot \left(\frac{\cos\theta}{\lambda}\right)^2 \cdot \frac{T}{\Theta_D^2} \tag{6.1.2}$$

with m the mass of the atoms, k_B the Boltzmann constant, Θ_D the Debye temperature and θ the scattering angle of the electrons with wavelength λ. The main result of this expression is that the intensity of a Bragg spot decreases exponentially with both the increase of temperature and electron energy. As an example, we tried to determine the Debye temperature of an In/Si(111)-(4 × 1) superstructure obtained by indium deposition on a clean silicon (7 × 7) surface [134–137]. The substrate consists of a vicinal p-doped Si(111) sample with a 2° miscut in the $[11\bar{2}]$ direction, which has the ohmic heater contacts placed along $[1\bar{1}0]$ in order to avoid step bunching during resistive heating. Well-ordered (7 × 7) surfaces (fig. 6.2) were produced by fast flashes up to 1450 K for 10-15 seconds, followed by annealing at about 1120 K and slow cool down. Indium deposition at a rate of 0.05 ML/min while keeping the Si(7 × 7) substrate at 720 K resulted in a triple-domain 4 × 1 reconstruction for a ≃ 1 ML In coverage (fig. 6.2). This surface has been shown to consist of well-defined In nanowires [137]. The Debye-Waller analysis of the (3,3)-spot revealed a Debye temperature Θ_D of about 117 K, as shown in the right side of fig. 6.2.

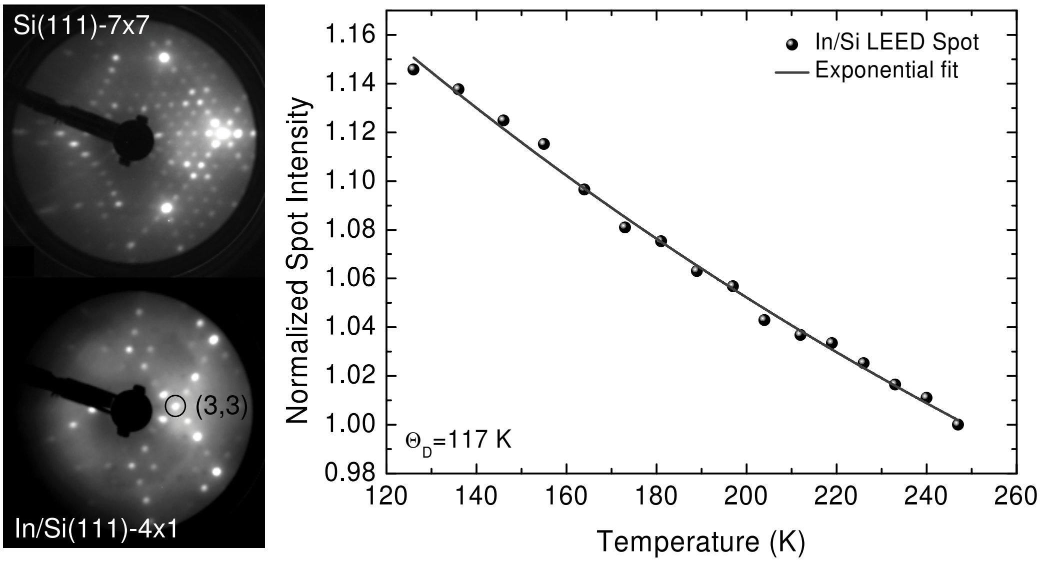

Figure 6.2: ***Left side:*** *LEED pattern of a Silicon(111)-(7×7) surface collected at 66 eV electron energy and of an In(4×1)/Si(111) superstructure at 100 eV.* ***Right side:*** *The In/Si(111)-(4×1) nanowires (3,3) spot intensity analysis, as a function of temperature, shows a quite low Debye temperature. The LEED patterns for these data were recorded at 65 eV electron energy.*

6.2 What is t-LEED?

The goal of time-resolved low-energy electron diffraction (t-LEED) is ultrafast real-time observation of surface structural modifications. It is a combination of LEED and ultrafast laser pump-probing technique. A laser pulse induces a transient excitation (temperature increase) on a surface which is then probed by a low-energy electron pulse. The LEED patterns produced by the electron pulses are then recorded as a function of the time delay between the laser and electron pulses. The main reasons for choosing LEED as a tool for surface structural analysis are the simplicity of data interpretation, as one can easily relate a LEED pattern to its corresponding surface structure (at least for a known structure), and high surface sensitivity for all incoming electron beam angles, provided by a high elastic scattering cross-section and a small inelastic mean free path. The transient surface temperature rise induced by the laser pulses is traced by looking at the spots of the LEED pattern along the delay (Debye-Waller effect). In other words the LEED pattern becomes an ultrafast thermometer. While in principle this experiment seems simple, in reality things are much more complicated. Just to mention some of the problems that may arise: first, one has to achieve the temporal and spatial overlap of the two pulses; second, the low energy of the electron pulses makes that the space-charge effects produced by the laser pulses are strong with respect to the actual Debye-Waller effect (one needs to find a way to separate the space-charge signal from the structural one). Also, there are stability problems like laser fluctuations or sample ageing. In connection to this last issue usually the experiment is chopped in order to ensure the experimental data stability by a normalization procedure.

The electron pulses are produced by laser pulses at the surface of a metallic cathode of an electron gun. During the experiments three different electron guns have been used. Two of them will be presented later on, namely a so-call LEED gun which was designed to output low-energy electron pulses and a MEED gun which is able to operate at a few thousand volts but was used in the low energy range. The third gun is referred to elsewhere [11].

The first requirement when performing a t-LEED experiment is that the laser and electron pulses are spatially overlapped and that their temporal coincidence is established. For this purpose, a simple method for cross-correlation of electron and laser pulses has been implemented (see chapter 6.4).

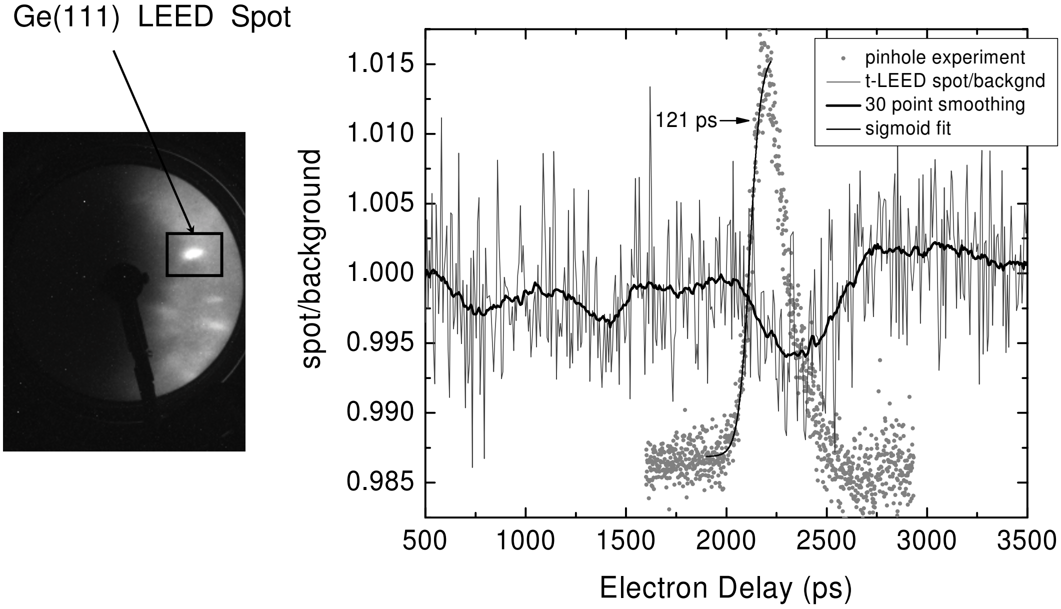

Figure 6.3: ***Left Graph**: A LEED pattern from the Ge(111)-c(2 × 8) surface produced by the MEED gun at 250 eV electron energy in almost normal incidence. The integration time was about 2 minutes. **Right Graph**: The normalized integrated LEED spot traced along the delay between the laser and electron pulses. The effect reads about 0.5% and has a time width of 200 ps. The transmission of the electron yield through a pinhole with a size of 0.5 mm diameter as function of the pulses delay was added for showing the coincidence between the pulses (see chapter 6.4). This curve gives the experimental resolution, about 120 ps in the case of the MEED gun.*

6.3 t-LEED on Ge(111)-c(2×8)

A stable clean Ge(111) surface exhibits a $c(2 \times 8)$ structure [138]. Due to its large absorption coefficient (over 50%) and low penetration depth ($\sim 0.3\,\mu$m) at light wavelength of 800 nm, it was thought to be good candidate for the t-LEED proof of principle. The experiments were performed with red laser (λ_o = 800 nm) pump power of about 10 nJ per pulse (at 45° incident angle) on the sample and probe electron pulses with count rates of about 10 kHz (at 85° incident angle). Even though a very good temporal and spatial overlap between the pump laser pulses and the probe electron pulses was established, the effect observed by comparing the LEED patterns with the pump pulses on the sample to those without showed at best a 0.5% effect (fig. 6.3). Taking into account the specific heat of germanium, $C_V = 0.31$ J/gK, and the laser spot size of 0.5 mm diameter and 10 nJ deposited energy per pulse, one can estimate a surface temperature increase of less than 1 K which translates into a Debye-Waller effect of less than 0.05%. Since such a small effect is virtually impossible to be observed we concluded that the effect observed in the measurements is produced by the transient space charge which builds up at the surface due to the high laser pump power. Further development made use of the fact that adding an overlayer to a known surface is reducing its Debye-Waller factor. For this purpose a In/Si(111)-(4×1) surface was used for t-LEED experiments but the results were inconclusive. It appears that the Debye-Waller effect was too weak to be observed in comparison with the space charge produced by the pump laser [11].

6.4 Paper: ElectronPhoton Pulse Correlator Based on Space-Charge Effects in a Metal Pinhole

A. Dolocan, M. Hengsberger, H.J. Neff, M. Barry, C. Cirelli, T. Greber and J. Osterwalder
Physik-Institut, Universität Zürich, Winterthurerstr. 190, CH-8057 Zürich, Switzerland

Jpn. J. Appl. Phys. **45** (1A), 285 (2006)

6.4.1 Abstract

A new procedure is demonstrated for cross-correlating light and electron pulses in a time-resolved surface diffraction experiment using low-energy electrons: Ultrashort laser pulses produce a space charge that modulates the transmission of the electron pulses across a pinhole. The proposed method is easily implemented into present pump-probe setups and represents a simple means for establishing spatial and temporal overlap of light and electron pulses on the sample. Moreover, the ultrafast space-charge dynamics allow the temporal resolution of the electron pulses to be characterized down to a time scale of less than 20 ps.

6.4.2 Introduction

Over the last several years, time-resolved electron diffraction proved to be an excellent tool for obtaining information about structural dynamics in molecules and in condensed matter [6,52,139–146]. The basic experimental setup is common to all these studies: ultrashort laser pulses are split into two parts, one of them being used for initiating the process under investigation, while the second one generates the electron pulse on a back-illuminated metallic thin-film cathode. The temporal delay between the two is varied by controlling the optical path length. The bias potential of the cathode with respect to the potential of the sample defines the electron energy at the sample.

In surface science the necessity of high sensitivity to a few atomic layers and the Debye-Waller effect, suppressing diffraction intensities of diffraction spots with increasing temperature and electron momentum transfer, set constraints for electron energy and scattering angles. As a consequence, two main energy ranges are exploited: high kinetic energies typically ranging from about 15 to 100 keV where surface sensitivity is achieved by grazing incidence of the electrons onto the sample (RHEED), and low energies of 20 to about 300 eV (LEED). In the latter range, scattering angles are large and the low kinetic energy allows for spectroscopic analysis of the backscattered electrons. In conjunction with vast theoretical efforts for modeling LEED intensities [8] the technique has been by far the most successful structural tool in surface science. The achievement of ultra-high temporal resolution, however, is largely hampered by the low electron velocity and the increasing importance of space-charge effects within single electron pulses as well as path length differences (see e.g. refs. [10, 147]). While at high energies the temporal resolution can be pushed into the range of a few hundreds of femtoseconds [6, 148], only theoretical estimates based on special gun designs can be found so far for low energies [10].

Several practical problems arise when conducting time-resolved electron scattering experiments: First, spatial overlap has to be established between the pump light and the probing electron pulses precisely at the center of interaction, *i.e.*, on the sample surface. This is a considerable task since the electron currents are of the order of pico- or even femtoamperes. Second, the coincidence time needs to be found, *i.e.*, the delay of the two laser pulses for which electron and light pulses hit the surface at the same time. Both, spatial and temporal overlap should be established independently of the experiment itself. Furthermore, the electron pulse width, which usually limits the temporal resolution, has to be measured. Based on the forces exerted on the electronic charge by the vector potential of the light, one might think about a direct electron-light correlation experiment. In this way, one could take advantage of the femtosecond light pulse in order to map the electron pulse shape to a high degree of accuracy. In practice, however, such “slicing” experiments require a long interaction path and small velocity mismatch in order to obtain observable signal intensities. Such requirements are met in synchrotron storage rings [149, 150]. In time-resolved electron scattering experiments, however, interaction volumes have to be kept small in order to maximize the temporal resolution owing to the high velocity mismatch [151].

In gas-phase experiments, it was shown previously that the shape of the electron spot in high-energy diffraction experiments is changed due to Coulomb interaction of the electrons with plasma created by intense light pulses via photoionization [140]. In that case the plasma produced a positive electron-optical lens which focused the electron beam. Maximizing this effect allowed the spatial and temporal overlap of electron beam and pump light to be established inside the gas jet with an accuracy corresponding to the beam waist and to about 2 ps, respectively [140, 141]. The temporal width of the electron pulses is then measured by streaking techniques which translate the time into a spatial dimension by deflecting the electron beam in a fast varying electric field [141].

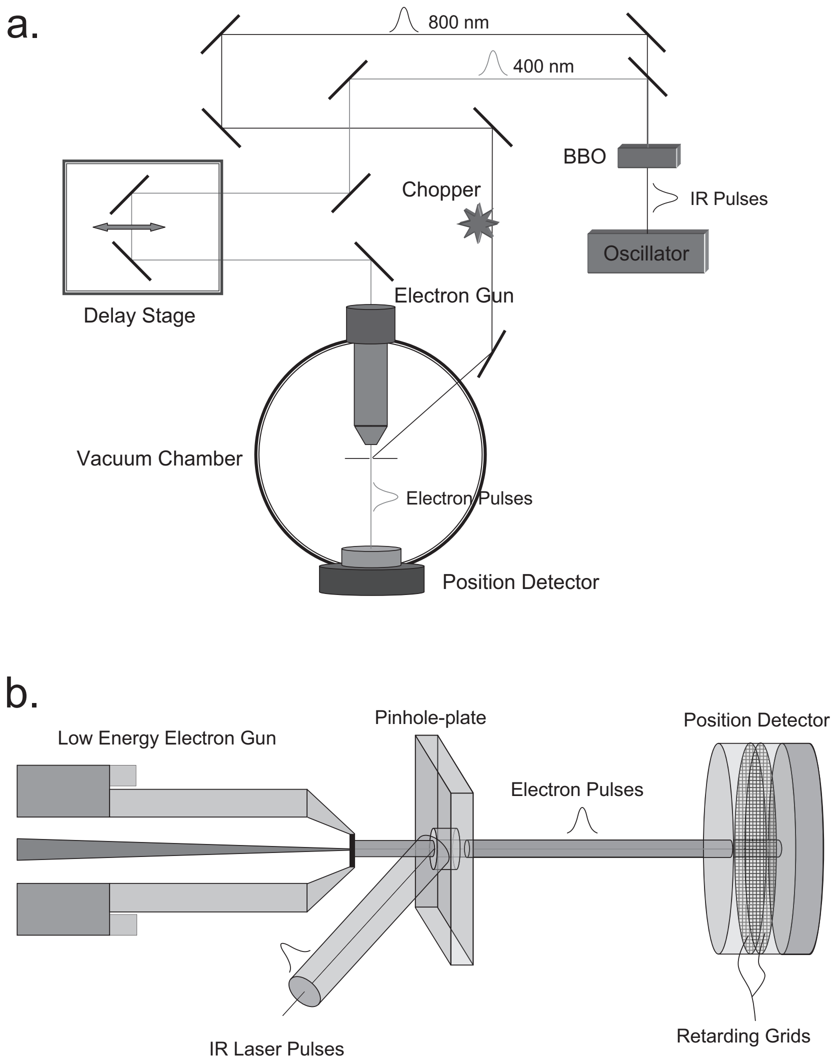

Figure 6.4: *a) Experimental setup of the electron-photon correlation experiment. b) Detailed view of the setup in the vacuum chamber with electron gun, pinhole plate, and electron detector.*

Due to the difficulties in implementing the streak camera close to the center of interaction, the actual pulse width has to be inferred from streak measurements and numerical simulations of the pulse broadening during the electron drift [152] or else from the experimental results themselves.

The purpose of this paper is to demonstrate that spatial and temporal overlap can routinely be found in a very simple experiment similar to the procedure used previously [140], but now applicable in a surface science experimental setup with no gas jet. Briefly, an aluminum plate is mounted beside the sample and at precisely the same distance from the electron gun. The electron beam is threaded through a pinhole in the plate and detected in transmission by a single-electron detector. The pump beam is focused into the pinhole and produces a short-lived electronic space charge by multi-photon photoemission [153]. In coincidence, the flux of electrons transmitted through the pinhole changes due to the Coulomb interaction between the electrons in the pulses and the space charge. While the spatial overlap is determined by the pinhole itself, temporal coincidence is obtained by recording the transmitted electron yield as a function of the pulse delay. Moreover, the fastest feature observed in the transient transmission can be used to set an upper bound for the electron pulse duration, only limited by the surprisingly short lifetime of the space charge and irrespective of the electron energy.

6.4.3 Experimental Setup

The complete setup consists of two separate parts, the femtosecond laser system and the actual electron scattering experiment in an ultra-high vacuum chamber [Fig. 6.4a]. The heart of the laser system is a Coherent Mira Seed Ti:sapphire oscillator providing 800 nm pulses of 55 fs duration. The pulses are stretched and amplified by a regenerative amplifier (Coherent RegA 9050) and finally recompressed to about 65 fs (assuming Gaussian pulse shape) by means of a grating compressor. At the output of the compressor, the pulse energy is about 5 μJ at a repetition rate of 250 kHz. Part of the light is frequency-doubled in a β-bariumborate (BBO) crystal and separated from the residual pump light by a dichroic mirror. It is used for producing the electron probe pulse on a back-illuminated metal cathode. The residual light is delayed in order to compensate for the electron flight time and focused to a size of about 200 μm into the pinhole (pump pulse), as shown in Fig. 6.4b. The pump beam is chopped with a frequency of about 1 Hz. This allows the data taken with pump light to be normalized to those taken without pump light. The length of the light path of the probe pulse and, thereby, the arrival time of the probe pulse with respect to that of the pump pulse is varied by means of a computer–controlled delay stage.

The vacuum system, with a base pressure in the low 10^{-9} Pa range, is equipped with standard surface science preparation and characterization facilities. Samples and the pinhole plate are mounted on a two-axes goniometer, described in detail in ref. [113]. By simple linear motion the pinhole plate can be moved to the position of the sample for time-resolved electron diffraction experiments such that the pinhole entrance is precisely at the same distance from the gun as the sample. The plate is made out of 1 mm thick aluminium and contains pinholes which are 300 μm, 500 μm, and 1 mm in diameter. Behind the pinhole plate, a position-sensitive resistive-anode detector is mounted. The input signal of the detector is amplified by a double-microchannel-plate assembly that was demonstrated to be sensitive to single electrons from the gun [10]. A biased grid in front of the detector works as high-pass filter and prevents low-energy secondary electrons from reaching the detector. The assembly is shown in Fig. 6.4b.

The intense pump pulse produces electrons in the pinhole via the photoelectric effect. For the given combination of low photon energy (1.55 eV) and high work function of the material (4.15 eV), multiphoton absorption is required [153]. The energy distribution of these photoelectrons was measured in a separate experiment, the results being shown in Fig. 6.5. The spectrum is characterized by a sharp onset at low energies and a broad structureless tail ranging up to 70 eV in kinetic energy. It has to be noted that the large space charge photoemitted by the intense laser pulse produces a electric dipole close to the surface, which shifts the spectrum to lower kinetic energies by a few hundreds meV. The kinetic energy zero was chosen such that it coincides with the onset measured in this spectrum. The average velocity of the photoelectrons was found to be 1.2×10^6 m/s for

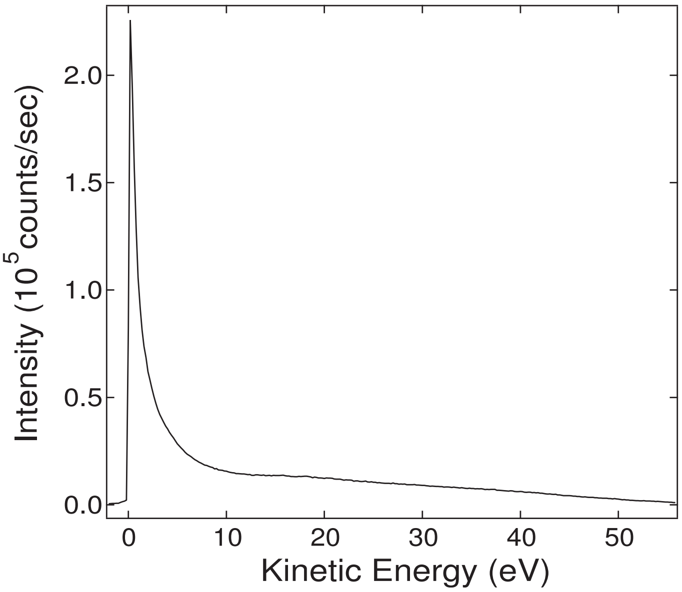

Figure 6.5: *Energy distribution of photoelectrons emitted from polycrystalline aluminium by multi-photon absorption at a photon energy of 1.55 eV. The work function was measured to be 4.15 eV. The sample was biased at -10 V, the kinetic energy scale is referenced to the vacuum level. The fluence of the light is about 10 mJ/cm*^{2} *in this case. The average velocity of the electrons in vacuum was determined to be* $\langle v \rangle \approx 1.2 \times 10^6$ *m/s.*

a fluence of about 10 mJ/cm^2, the total photocurrent was $\approx 8 \times 10^4$ electrons per laser shot or ≈ 3 nA. The resulting quantum efficiency, defined as the average number of photoelectrons per impinging photon amounts to $\eta \approx 4 \times 10^{-9}$ for this process.

The experiments were carried out with two different pulsed electron sources. The first one, referred to hereafter as LEED–gun, was developed for electron diffraction with high temporal resolution (5 ps) at low kinetic energies [10, 154]. The head of this gun contains a gold film cathode on a mica substrate, which is separated from the anode through a kapton thin film spacer of $d = 75\,\mu$m thickness. The anode is an 800 μm thick microchannel plate, held on ground potential, which acts as collimator for the electrons. The distance between the cathode and the sample (here the pinhole) is about 4 mm which leads to an electron flight time of about 500 to 1000 ps for kinetic energies of the order of 100 eV. The electron beam diameter is $\approx 400\,\mu m$. The theoretical time spread of the electron pulses was calculated to be below 5 ps for an initial energy distribution of 1.2 eV, which is determined by the work function of gold and the employed photon energy of 3.1 eV [10].

The second gun, referred to as MEED–gun, was originally designed for high- and medium-energy electron diffraction [155, 156] and was operated here at low energy with re-optimized lens settings. The electrostatic lenses were adjusted using ray-tracing calculations [157] such that the electrons were accelerated to high kinetic energy (3 keV) directly after emission from the cathode and decelerated to their final kinetic energy at the exit of the gun. The total flight time of the electrons over the distance of roughly 34 cm from the cathode to the sample was, thereby, reduced from 44 to 27 ns. Based on the ray-tracing calculations, the final temporal spread of the electron pulses from the MEED–gun at the sample or pinhole plate was estimated to be of the order of 150 ps for

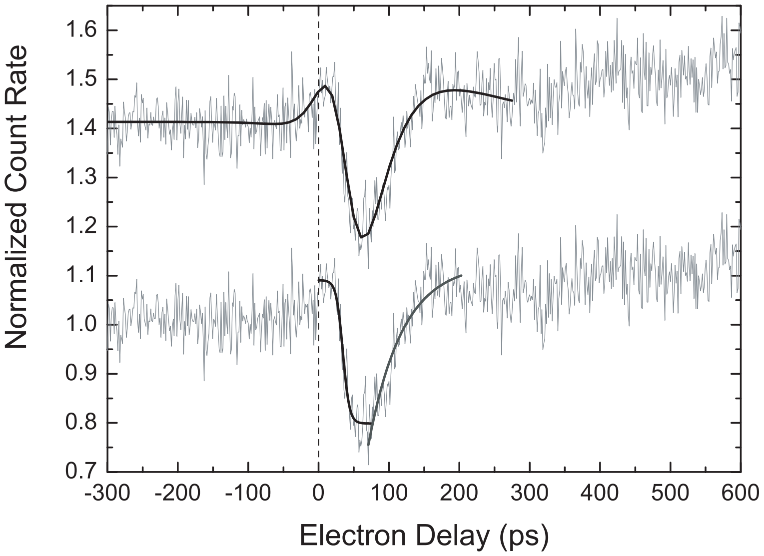

Figure 6.6: *Electron-photon correlation curve for electron pulses of 250 eV kinetic energy produced with the LEED-gun. The red laser power impinging on the 500 μm diameter pinhole was ≃0.9 W. The data have been normalized for each delay by the corresponding count rate without pump light on the pinhole. The same measurement is plotted twice in order to illustrate two different fitting functions for describing the correlation signal (see text). The upper curve has been simply offset.*

excitation of electrons from the silver cathode using photons of 3.1 eV energy.

6.4.4 Experimental Data

In Fig. 6.6 an electron-photon correlation curve for electron pulses of 250 eV kinetic energy produced with the LEED-gun is shown. As long as the electron pulses arrive at the pinhole before the red laser pump pulses, the count rate measured behind the pinhole is constant (normalized to unity). Near the coincidence point we see a sharp drop by about 20% of the electron count, a slightly slower recovery, and a weaker, more extended ringing for longer electron delays. This demonstrates clearly that we observe an interaction between the pump light and the electron pulses mediated by the transient space charge in the pinhole.

The curves were fitted in two different ways (see Fig. 6.6) in order to quantify time scales (bottom curve), or to get further insight into the interaction processes of the electron pulses with the space charge (top curve). In the first approach, the leading edge is fitted by a step function of the Fermi-Dirac type. The rise time (or here rather 'drop time') Δt is defined as the time interval over which the Fermi-Dirac function drops from 90% to 10% of its maximum step height. For this particular data set we obtain a value of $\Delta t \leq 20$ ps, which is the shortest feature ever observed in our experiments. The count rate recovery is fitted with a simple exponential of negative amplitude, from which a recovery time τ of 50 ps results. The weak oscillations at longer delays have not been further analyzed. Since the measured drop time Δt results from a nontrivial convolution (in space and time) of the electron pulse shape and the temporal profile of the space charge formation, the value of 20 ps gives an upper limit for both.

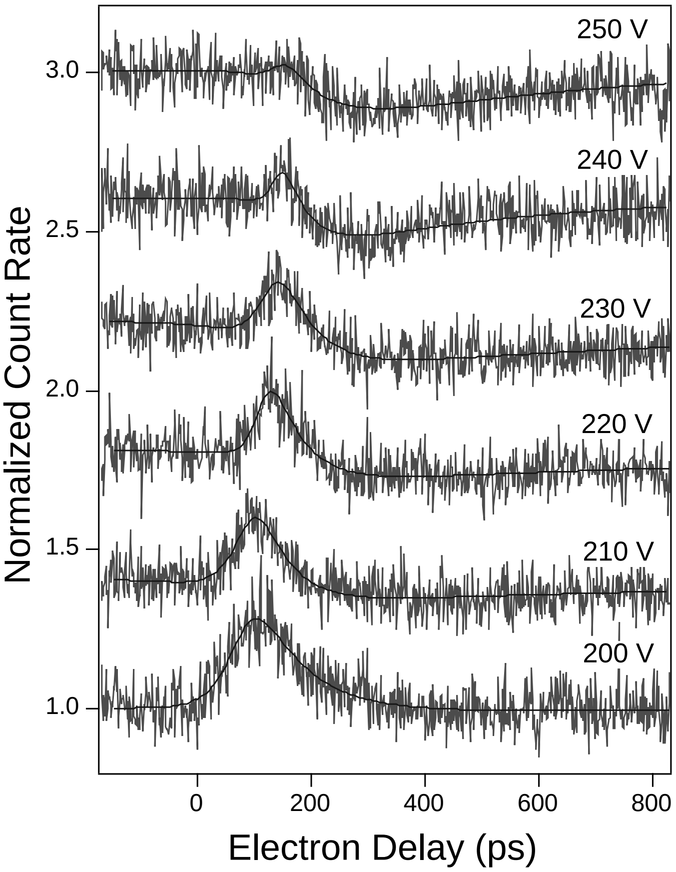

Figure 6.7: *Electron-photon correlation curves for electron pulses of 200 to 250 eV kinetic energy produced with the LEED-gun. The pinhole diameter was 300 μm, the red laser power $\simeq$0.5 W. The delay times are referenced to some arbitrary but fixed position of the delay line. All curves except for the lowest one have been offset by an increasing amount. The fits represented by the solid lines are discussed in the text.*

For a simple model of the space charge dynamics, we use the value for the mean velocity $\langle v \rangle \approx 1.2 \times 10^6$ m/s of the electrons produced by the pump pulse. Again, this has to be taken as upper limit since kinetic energy is redistributed within the space charge during the flight owing to Coulomb interaction between the electrons [152]. Since this effect broadens the energy spectrum, the initial energy distribution is expected to be piled up at lower kinetic energies. The value of the average velocity given above corresponds to the velocity of the center of gravity of the space charge in one dimension[c]. During the maximum space-charge build-up time (taken as $\Delta t = 20$ ps) the electrons travel with this energy a distance of 23 μm, which means that they have only the time to form a ring of charge around the 500 μm diameter pinhole[d]. During the recovery time of 50 ps they

---

[c] Employing a simple one-dimensional model here is justified because all relevant length scales are smaller than the lateral size of the beamwaist of the pump laser.

[d] For reasons of tractability, we assume in this discussion a cylindrical symmetry around the pinhole axis, neglecting the strong perturbation of this symmetry by the oblique incidence of the pump beam onto the pinhole.

travel an additional 58 μm. If one assumes that the electron cloud forms half a torus centered on the pinhole axis, the thickness of which grows with time (with a volume $V(t) = \pi^2[r(t)]^2 R$, where $R = 250\,\mu$m is the radius of the pinhole) then one can compute the mean electron density as a function of time: $1.8 \times 10^{-2}\,C/m^3$ ($r = 23\,\mu$m) after the 20 ps space-charge build-up time and $1.5 \times 10^{-3}\,C/m^3$ ($r = 81\,\mu$m) after the 50 ps relaxation. The density is about one order of magnitude higher after the build-up part which shows that the electron cloud disperses quite fast over a time scale of 50 ps. From our data we conclude that the electrostatic potential built by the space-charge has a maximum influence on the electron beam when it is concentrated on a radius of about 50 μm around the pinhole edge.

Before the second approach to fitting the correlation curve (top curve of Fig. 6.6) is discussed, we show in Fig. 6.7 the electron-photon correlation curves for different electron energies, i.e. cathode potentials in the LEED-gun. All curves show a correlation signal, but the shape changes dramatically with the electron energy. While there is again a marked drop ($\simeq$-11%) of electron transmission through the pinhole at 250 eV, an effect we term *shielding*, the opposite behavior is observed for 200 eV electrons: the transmission increases by $\simeq$+27% near the coincidence point. Accordingly, we term this effect *lensing.* There is a gradual change from lensing to shielding behavior with increasing energy. Likewise, there is a gradual shift of the onset of the leading edge to later delay times. This latter effect is related to the increasing speed of the electrons. In order to coincide with the red laser pump pulse (which fixes the delay axis) at the pinhole, faster electrons must be produced later at the photocathode, i.e. there is a right-shift of the onset with increasing energy.

The observation of both shielding and lensing effects in the correlation curves raises the question as to how the shape and the dynamics of the space-charge cloud influences the electron trajectories and thus the transmission of the electron beam. In §IV it is briefly discussed that reasonable static space-charge distributions can be constructed to produce either shielding or lensing. We take this as a justification for introducing a pragmatic model for the space-charge dynamics and its effects on the pinhole transmission, leading to the second type of fitting function to the correlation curves (Fig. 6.6, upper curve). Let $\rho_L(\mathbf{r})$ be a static charge distribution at the pinhole that leads to lensing and $\rho_S(\mathbf{r})$ one that leads to shielding. Let us further assume that $\rho_L(\mathbf{r})$ and $\rho_S(\mathbf{r})$ can be found such that the actual space-charge cloud $\rho(\mathbf{r}, t)$ can be represented for any time t as a linear combination of the two: $\rho(\mathbf{r}, t) = c_L(t)\rho_L(\mathbf{r}) + c_S(t)\rho_S(\mathbf{r})$. Due to the linearity of Poisson's equation and the equations of motion, this charge distribution should, to first order, produce the observed combination of lensing and shielding effects observed in our experiment. The model neglects truly dynamical effects arising due to time-dependent electric fields. The time-dependent coefficients are represented by a leading edge, represented as a Fermi-Dirac function (τ_1^L, τ_1^S), multiplied by an exponential decay (τ_2^L, τ_2^S), providing an excellent description of the shielding (lensing) case alone (Fig. 6.7, top and bottom curves). The complete fitting function for the normalized electron transmission through the pinhole, where $N_0 + \Delta N(t)$ and N_0 are the numbers of transmitted

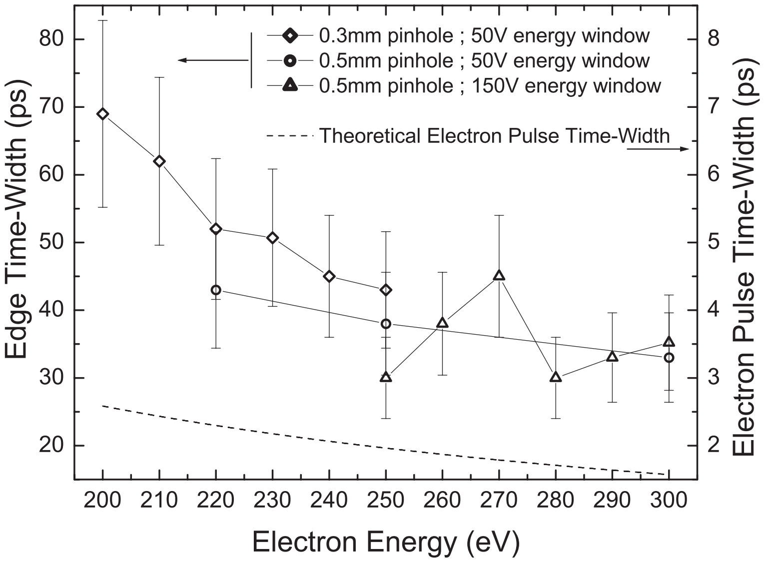

Figure 6.8: *Compilation of the leading edge temporal widths from most of the electron-photon correlation data measured for the LEED-gun. As indicated by the legend, some curves have been measured with a 300 µm diameter pinhole (◇), some with 500 µm (○, △). In the former case, the detector energy window (see text) was 50 eV, in the latter case either 50 eV (○) or 150 eV (△). The error bars reflect the scatter of values obtained in repeated measurements. The dashed line indicates the theoretical value for the expected temporal spread of the electron pulse due to the non-monochromaticity ($\Delta E = 1.12$ eV) of the beam.*

electrons in the presence or absence of pump beam pulses, respectively, is then:

$$\begin{aligned}\frac{N_0 + \Delta N(t)}{N_0} &= A_L c_L(t) - A_S c_S(t) + 1 = \\ &= \frac{A_L\, e^{-(t-t_0)/\tau_2^L}}{1 + e^{-(t-t_0)/\tau_1^L}} - \frac{A_S\, e^{-(t-t_0)/\tau_2^S}}{1 + e^{-(t-t_0)/\tau_1^S}} + 1\end{aligned} \tag{6.4.3}$$

with A_L and A_S describing the amplitude of the lensing and shielding effect, respectively. t_0 defines the rising/falling edge position. In order to limit the number of free parameters, one common parameter t_0 is used for both effects.

As is evident from Figs. 6.7 and 6.6 (upper curve) this function provides an excellent description of all data. For the data of Fig. 6.7 the resulting fitting parameters can be used to analyze the interaction of the electron beam with the space charge. From a linear regression to values of the edge position t_0 versus the inverse of the electron velocity we obtain a slope of 5.21 mm, which relates to the electron drift distance from the photocathode to the pinhole plate. It is in good agreement with the geometrical distance of about 4 mm, considering that this analysis neglects the acceleration of the electrons between cathode and anode. Over the voltage range from 200 to 250 eV, the lensing amplitude A_L drops from about 0.51 to 0.28, while A_S increases from 0.01 to 0.25. Since the lensing and shielding functions are not normalized, these amplitudes do not reflect the visual impression that at 250 V there is essentially shielding only. Unfortunately, it is found that the characteristic times τ_1^L, τ_2^L, τ_1^S, τ_2^S are rather interdependent and do not allow for an unambiguous description of the space charge dynamics. The most stable of these parameters is τ_1^L which describes the width of the leading lensing edge. It is found to decrease gradually from 21 to about 13 ps over the measured voltage range. This narrowing of the edge reflects the change of the temporal width of the electron pulse that probes the space charge region and the time (and distance) over which this pulse is affected by the space charge.

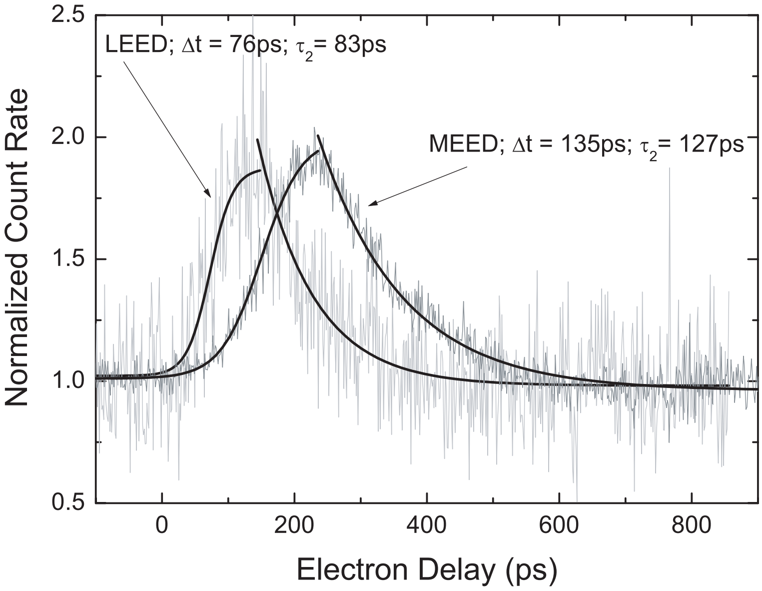

Figure 6.9: *Comparison of electron-photon correlation curves for electron pulses of 200 eV energy produced by the LEED-gun or by the MEED-gun, using the 300 μm diameter pinhole. The red-laser pump power was 0.9 W in both cases, the detector energy window was set to 50 eV and 5 eV for the LEED-gun and MEED-gun, respectively. The simple edge-fitting method was applied in order to extract the characteristic temporal parameters.*

Due to the interdependence of the characteristic times in this model we revert to the simpler edge-fitting procedure described earlier (Fig. 6.6, bottom curve) for a discussion of the fastest temporal change appearing in the curves around the coincidence point, i.e. the leading edge, and its dependence on various experimental parameters. Note that the edge time-width Δt for the 90 - 10% drop time of a Fermi-Dirac function (proportional to $1/(1+\exp-(t-t_0)/\tau_1)$) corresponds to about $4.4 \times \tau_1$. In Fig. 6.8 we give these width Δt as a function of electron energy. There is a systematic narrowing of the edge with increasing energy suggesting that the edge width is an indicator for the electron pulse width. The large scatter in these values show how sensitive the correlation curves are to the spatial alignment of the pump and probe pulses with respect to the pinhole and to each other. Reproducibility was thus a serious issue in these experiments, which is indicated in the figure by the large error bars. Another issue is that the edge widths are larger than the pulse widths theoretically expected for the LEED-gun by more than an order of magnitude. In taking into account only the effect of non-monochromaticity of the electrons ($\Delta E = 1.12eV$ [10]) we expect a time spread

$$\Delta t \approx \frac{\sqrt{m}}{2eV_0}\left(\frac{d}{\sqrt{2E}} + \frac{L}{\sqrt{2eV_0}}\right)\Delta E, \tag{6.4.4}$$

from which we obtain pulse widths as indicated by the dashed curve in Fig. 6.8. Here, d and L are the cathode-anode distance and the drift distance to the sample, respectively, V_0 is the cathode (or acceleration) voltage and E is the initial energy at the photocathode, here taken as $E = \Delta E/2$ =0.56 eV, and m is the electron mass. Expression (6.4.4) holds for $\Delta E \ll eV_0$. The measured edge widths are much larger than the theoretically expected ones, though they follow the expected energy dependence. The edge width depends in a complex way on the time constants of the transient electric field produced by the space charge in the pinhole and the pulse width of the electron pulse. Further experiments and numerical simulations will be needed to disentangle these time broadening effects. Owing to the energy dependence of the observed edge width, it is likely that the electron gun makes the dominant contribution to the temporal resolution. Nevertheless, it has to be emphasized that this is the first time that such high temporal resolution has been achieved with electrons at low kinetic energy.

Energy resolution on the detection side is an efficient means for increasing the temporal resolution. This can be seen by analyzing correlation curves measured with different potentials at the retarding grids of the two-dimensional detector. For 250 eV electrons the edge width drops from $\sim$ 120 ps at 50 V retarding potential to $\sim$ 200 ps at 230 V. In the latter case, the energy window seen by the detector is reduced to 20 eV and most of the inelastically scattered and secondary electrons, produced either in the LEED-gun or in the pinhole, are suppressed.

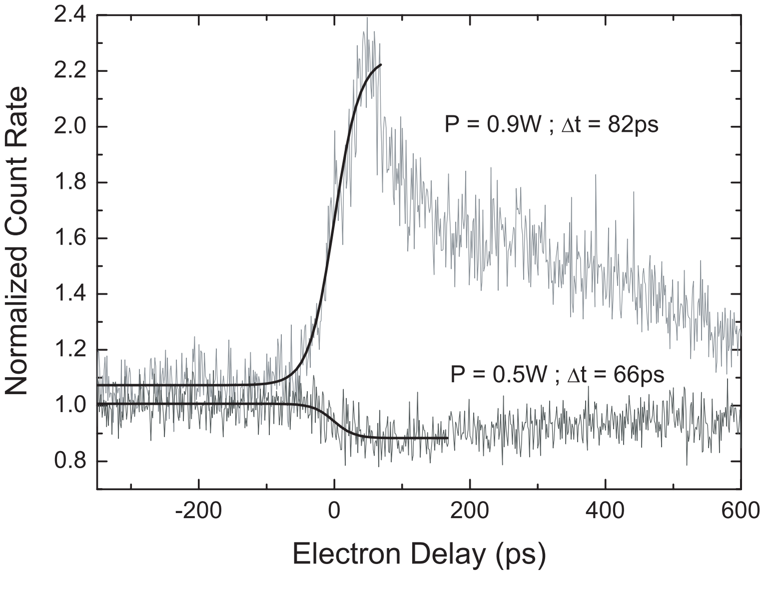

Figure 6.10: *Influence of the red laser pump power on the electron-photon correlation curve for LEED-gun pulses of 250 eV energy. The two curves were measured back to back, with pump powers of 0.9 W (upper curve) and 0.5 W (lower curve) on the 300 μm diameter pinhole. The leading edges were fitted with Fermi-Dirac functions to determine the 90 to 10% drop (rise) times* Δt.

In order to create a situation where the time scale of the correlation signal is clearly dominated by the width of the electron pulses, we carried out similar experiments with the MEED-gun that produces much longer electron pulses when used in the low-energy range. In Fig. 6.9 correlation curves for the two guns are compared for an electron energy of 200 eV. Due to the much higher beam current of the MEED-gun, the detector window could be reduced to 5 eV in this case. Nevertheless, the edge width for these pulses is significantly larger than that from the LEED-gun. At least in the leading edge, the curve provides a good measure of the temporal profile of the electron pulses. The width of the rising edge is $\Delta t = 135$ ps which is in good agreement with a value of 144 ps obtained from ray tracing calculations for the MEED-gun. The rise-time Δt and the decay time τ_2 are very similar suggesting that the electron-photon correlation function is dominated by the time resolution of the MEED-gun. When the electron energy of the MEED-gun pulses is varied, similar effects are observed as those seen with the LEED-gun (Fig. 6.7): with increasing energy the leading edge shifts to later delays and the edge width narrows, and the general behavior transforms from lensing to shielding. The temporal shifts are much larger in this case due to the long electron path lengths in this gun.

One means for manipulating the space charge and its dynamics is to vary the power of the red pump pulses. As Fig. 6.10 shows impressively, the correlation curve changes dramatically when the pump power is roughly doubled. The behavior shifts from shielding to lensing, with a strong increase of the overall effect (+110% versus -11%), and with a slight increase in the edge width. Increasing the pump power not only multiplies the number of electrons in the space charge cloud, it also increases the effective pump-beam cross section at the pinhole, and thus the volume of the space charge. The mechanism leading to the drastic changes in the correlation curves is not clear. It cannot be elucidated without a detailed modeling of the space charge dynamics and its effects on the electron beam trajectories, which is beyond the scope of this paper. However, these strong effects must be responsible for the large scatter and poor reproducibility of correlation curves that we have seen in the course of these experiments.

In a pragmatic sense we can give the following recommendations for the use of this pinhole-based electron-photon pulse correlator: By maximizing the overall effect that the electron pulses see from the pinhole, one can optimize the spatial overlap of red laser pump and electron probe pulses and find the temporal coincidence time at the pinhole. At least down to the time scale of the order of 20 ps, as demonstrated here, the temporal profile of the electron pulses can be characterized. Replacing the pinhole-plate with a sample by a simple linear translation, one can perform other electron-photon correlation experiments, such as e.g. time-resolved LEED, with the significant advantage of having previously established spatial and temporal overlap on the sample surface. Even though the temporal profile of the electron pulses cannot be characterized as precisely as with a streak-camera, the information is sampled at the position of interest and not after some distance where further temporal spread occurs that has to be taken in consideration for the retrieval of the true pulse width. We also would like to emphasize that the space charge following the absorption of intense laser pulses in pump-probe experiments may also occur in electron scattering experiments. This effects should thus be considered carefully during the analysis of any time-resolved experiments involving electrons.

6.4.5 Theoretical Notes and Simulations

The non-trivial combinations of lensing and shielding effects seen in the correlation experiments are not easy to understand in detail. They are obviously related to the energy and to the temporal spread of the electron pulses as well as the space-charge dynamics, the details of which are beyond the scope of this work. Nevertheless we attempt to have some insight into the mechanisms for the two effects from simple electrostatic arguments. The simplest way to put the problem is to consider the space-charge as an infinitely thin circular charge distribution with radius R at the pinhole entrance. The potential along the pinhole axis z is then easily calculated as

$$\Phi(z) = \frac{Q_0}{4\pi\epsilon_0\sqrt{R^2+z^2}}. \tag{6.4.5}$$

Here, Q_0 is the total amount of charge on the circle that can be approximated by the total charge excited by one red laser pump pulse, which was estimated to be 8×10^4 electrons for aluminium as the pinhole material (see Section 6.4.3).

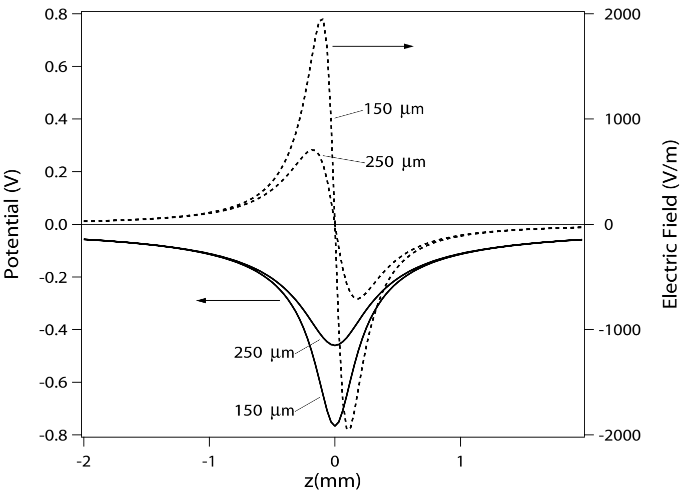

Figure 6.11: *Calculated potential and electric field for R=150 and* 250 *µm (with* Q_0 *estimated from the aluminium spectrum of Fig. 2.4).*

Fig. 6.11 shows the potential as well as the electric field along the central axis for the 300 μm and the 500 μm diameter pinholes. The potential values reached on the axis are less than 1 V. At electron energies of the order of 200 eV we thus expect the main effects arising at the fringes of the pinhole, not at the center. This is confirmed by ray tracing calculations using cylindrical symmetry and a similarly simple charge distribution at the pinhole entrance that produces a focussing of the beam near the pinhole axis while trajectories near the rim are rejected that would pass through the pinhole in the absence of an electric field (thus *shielding*). However, these simulations cannot explain the large magnitude of the shielding effect (up to 20%).

The lensing effect is even harder to explain. In this simple potential geometry, the only way to obtain lensing in ray tracing calculations was by threading the beam with some tilt angle relative to the axis through the pinhole. Basically, the space charge potential can then help to steer electrons through the pinhole. In the real experimental geometry the situation arises more likely due to some lateral misalignment of the electron beam with the pinhole, and due to the oblique incidence of the pump beam onto the pinhole. Situations can then be constructed where the repulsive space charge potential pushes more electrons into the pinhole (thus *lensing*).

Overall, the large magnitudes observed for both lensing and shielding effects can only be understood as a consequence of a strong perturbation of axial symmetry of the space charge geometry arising from the oblique incidence of the pump beam onto the pinhole. Subtle changes in the alignment of electron and pump beam with respect to each other, and to the pinhole, thus lead to dramatic changes in electron transmission, explaining also the difficulty in reproducing exactly the same correlation curves in repeated experiments. Since this alignment is likely changed by small amounts in varying parameters like electron energy or pump beam power, systematic changes in the shape of the correlation curves, like those observed in Figs. 6.7 and 6.10, must not necessarily reflect significant changes in the space charge dynamics but more trivial geometrical effects. Nevertheless, the time scale provided by the leading edge should still be a measure for the electron pulse width and the space charge build-up time.

6.4.6 Conclusions

A device based on electron transmission through a pinhole is demonstrated for establishing temporal and spatial correlation for low-energy electron pulses and laser pulses. It is easily implemented in a pump-probe electron diffraction experiment and can be used for electron beam characterization at the site of the sample in a surface diffraction chamber. Down to a time scale of 20 ps the leading edge in the temporal correlation curve for electron transmission through the pinhole versus pump-probe delay provides information about the pulse width of the electron beam.

It is anticipated that this simple experiment may have further applications. As an example, the spatial intensity distribution and the beam divergence of the electron beam can easily be measured by using the pinhole as an aperture and recording the transmitted intensity as a function of transverse and longitudinal position of the pinhole with respect to the electron gun. As a more far-reaching application, one might even take advantage of the lensing effect by slightly misaligning a *continuous* electron beam with respect to the pinhole and to create picosecond electron bunches behind the pinhole by slicing the beam due to interaction with the short-lived space charge produced by the laser pulse.

Moreover, the two-dimensional electron detector used in this experiment lends itself for further characterization of the electron beam, but it can easily be replaced by a single channeltron detector for this type of correlation experiments, making the whole setup cheap and simple.

6.5 t-LEED Setup Improvements

The t-LEED data collected for various samples by spot intensity analysis along the pulse delay showed inconclusive results. At the most, we were able to observe a 0.5% effect on a germanium (111)-c(2×8) reconstructed surface by recording the full integrated LEED spot intensity along the delay (see section 6.3). This effect was assigned to the pump-laser induced space charge which

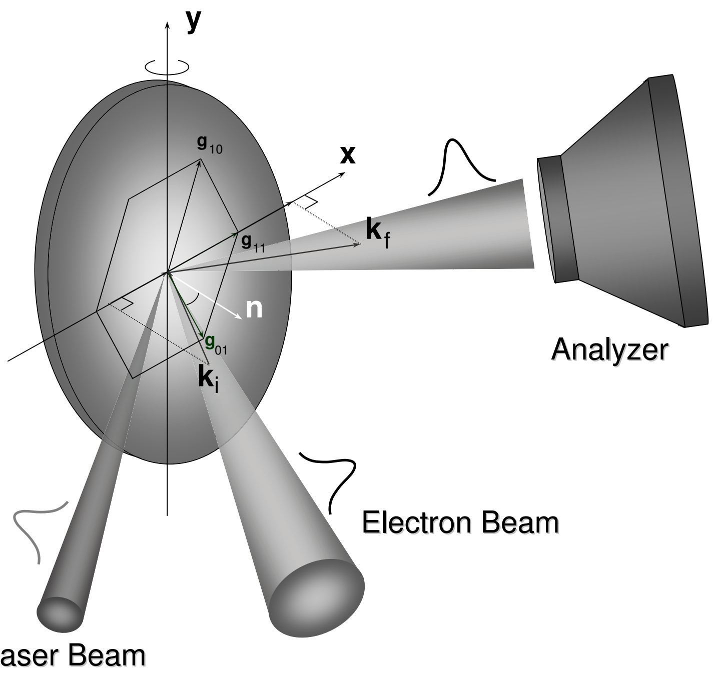

Figure 6.12: *The new setup makes use of an electron energy analyzer.*

builds up at the surface. Finally, it became obvious that a LEED detector could not bring the required sensitivity for separating the Debye-Waller process from the observed space-charge effect. Also, the pulsed low-energy electron gun was yielding a very low electron flux which made long integration times (∼15 minutes) necessary for a decent LEED image. Therefore, depending on the temporal resolution required, the overall duration of an experiment was often beyond 12 hours, affecting the experimental stability (sample ageing, laser fluctuations, electron beam fluctuations, etc).

Recently, a new pulsed low-energy electron gun has been constructed in our group, which adds an electrostatic lens after the anode for beam collimation. Moreover, in order to increase the experimental sensitivity, we implemented an electron energy analyzer (fig. 6.12). By means of the two-axis sample goniometer, individual LEED spots can be directed into the analyzer by rotating the sample. This detection scheme has certain advantages over a LEED detector: better time resolution, as it can energy resolve the LEED spots, and faster data acquisition. Most recent data show very interesting results, but more experiments and better analysis is still required as the actual Debye-Waller effect must be extracted from the observed transient effect [11].

Chapter 7

Conclusions and Outlook

Pump-probe experiments are the basic tool for real time observation of fast microscopic processes. During this thesis, electronic and structural dynamics of different surfaces were investigated. A strong accent was placed onto the characterization of ultrashort pulsed lasers since they are instrumental for studies of ultrafast dynamics. As a result, the main methods for laser pulse diagnostics were reviewed and applied for the case of our laser system.

One of the most intriguing nanostructures discovered in the last few years, the so-called *nanomesh* [12], was studied by means of time-resolved two-photon photoemission (t-2PPE). Due to its insulating behavior and high degree of stability at room temperature and even in open air, this regular nanostructure has the potential of becoming a template for supramolecular constructions. Under certain conditions, tow-photon photoemission (2PPE) can successfully replace the standard methods, like inverse photoemission, when mapping the unoccupied states of a given surface. Two-color t-2PPE experiments performed on the nanomesh revealed that there are two initial states (about 0.1 eV binding energy) and one intermediate state (around 3 eV above the Fermi level) which can be excited within our experimental conditions. The lifetime of the quasiparticle excited in the intermediate state was found to be about 10 fs. Comparison with the DFT calculations of a hypothetical double layer (1×1) h-BN on Rh(111) [13] finds a good agreement for the position of the intermediate state. The information obtained in the t-2PPE experiments on the nanomesh can be used as input for further calculations.

Low-energy electron diffraction (LEED) is a well established tool in surface science which gives access to long-range order of different surfaces. Emerging as a new method for investigation of fast surface structural modifications, time-resolved LEED (t-LEED) makes use of short low-energy electron pulses. These pulses are produced by laser pulses at the cathode of an electron gun through photoeffect. During this thesis we used three electron guns [9–11]. Since the temporal and spatial overlap between the laser and electron pulses is a crucial step in performing t-LEED, a new simple method for correlating the laser and electron pulses was developed [14]. This method gives also an estimation for the upper limit of the electron pulses. The t-LEED experiments were performed on several systems. Among them, the surfaces Ge(111)-c(2×8) and In/Si(111)-(4×1) are presented. Unfortunately, due to the strong space charge built at the sample surface by the pump red laser pulses, the overall effect (less than 0.5%) could not be attributed to the Debye-Waller effect.

Bibliography

[1] M. Muntwiler, Ph.D. thesis, University of Zürich (2004).

[2] M. Drescher, M. Hentschel, R. Kienberger, M. Uiberacker, V. Yakovlev, A. Scrinzi, Th. Westerwalbesloh, U. Kleineberg, U. Heinzmann and F. Krausz, Nature **419**, 803 (2002).

[3] A. Zewail, J. Phys. Chem. A **104**, 5660 (2000).

[4] T. Hertel, E. Knoesel, M. Wolf and G. Ertl, Phys. Rev. Lett. **76**, 535 (1996).

[5] H. Petek and S. Ogawa, Prog. Surf. Sci. **56**, 239 (1997).

[6] B. J. Siwick, J. R. Dwyer, R. E. Jordan and R. J. D. Miller, Science **302**, 1382 (2003).

[7] T. E. Felter, R. A. Barker and P. J. Estrup, Phys. Rev. Lett. **38**, 1138 (1977).

[8] J. B. Pendry,*Low Energy Electron Diffraction*, Eds.: G.K.T. Conn and K.R. Coleman, Academic Press (1974) *Techniques of Physics Series.*

[9] H. Neff, Ph.D. thesis, University of Zürich (2002).

[10] R. Karrer, H. J. Neff, M. Hengsberger, T. Greber, and J. Osterwalder, Rev. Sci. Instrum. **72**, 4404 (2001).

[11] C. Cirelli, Ph.D. thesis, University of Zürich (2006).

[12] M. Corso, W. Auwärter, M. Muntwiler, A. Tamai, T. Greber, J. Osterwalder, Science **303**, 217 (2004).

[13] T. Greber and P. Blaha, private comunications.

[14] A. Dolocan, M. Hengsberger, H. J. Neff, M. Barry, C. Cirelli, T. Greber and J. Osterwalder, Jpn. J. Appl. Phys. **45**, 285 (2006).

[15] J. D. Jackson, *Classical Electrodynamics*, 3rd edition, J. Wiley & Sons (1999).

[16] M. Born, E. Wolf, *Principles of Optics*, 7th edition, Cambridge University Press (2002).

[17] E. Hecht, *Optics*, 4th edition, Addison Wesley (2002).

[18] E. Hecht, Am. J. Phys **38**, 1156 (1970).

[19] C. C. Davis, *Laser and Electro-Optics*, reprint, Cambridge (2000).

[20] B. E. A. Saleh, M. C. Teich, *Fundamentals of Photonics*, J. Wiley & Sons (1991).

[21] T. H. Maiman, Nature **187**, 493 (1960).

[22] R. Trebino, *Frequency-Resolved Optical Gating*, Kluwer Academic Publishers (2000).

[23] P. Hamm, *Laser spectroscopy course notes*, unpublished (2002).

[24] J.-C. Diels, R. Wolfgang, *Ultrashort Laser Pulse Phenomena*, Academic Press (1996).

[25] C. Rullière, *Femtosecond Laser Pulses*, Springer (1998).

[26] W. Greiner, *Quantum Mechanics*, 4th edition, Springer (2001).

[27] T. D. Donnelly and C. Grossman, Am. J. Phys. **66**, 677 (1998).

[28] F. Krausz, M. E. Fermann, T. Brabec, P. F. Curley, M. Hofer, M. H. Ober, C. Spielmann, E. Wintner and A. J. Schmidt, IEEE J. Quantum Electr. **28**, 2097 (1992).

[29] L. E. Hargrove, R. L. Fork and M. A. Polock, Appl. Phys. Lett. **5**, 4 (1964).

[30] O. G. Peterson, S. A. Yuccio and B. B. Snavely, Appl. Phys. Lett. **17**, 245 (1970).

[31] E. P. Ippen, C. V. Shank and A. Dienes, Appl. Phys. Lett. **21**, 348 (1972).

[32] P. F. Moulton, J. Opt. Soc. A. B **3**, 125 (1986).

[33] D. E. Spence, P. N. Kean and W. Sibbett, *Sub-100 fs Pulse Generation from a Self-Mode-Locked Ti:sapphire Laser*, Conference on Laser and Electro-Optics (Opt. Soc. of Am., Anaheim, 1990) paper CPDP-10-1, p.619 .

[34] M. Piché, Opt. Comm. **86**, 156 (1991).

[35] H. Haus, J, G. Fujimoto and E. P. Ippen, IEEE J. Quant. Electr., **28**, 2086 (1992).

[36] G. Steinmeyer, D. H. Sutter, L. Gallmann, N. Matuschek and U. Keller, Science **286**, 1507 (1999).

[37] J. P. Heritage and R. Jain, Appl. Phys. Lett. **32**, 101 (1978).

[38] W. H. Knox, R. L. Fork, M. C. Downer, R. H. Stolen. C. V. Shank and J. A. Valdmanis, Appl. Phys. Lett. **46**, 1120 (1985).

[39] W. H. Knox, IEEE J. Quant. Electr. **24**, 388 (1988).

[40] R. L. Fork, C. H. B. Cruz, P. C. Becker and C. V. Shank, Opt. Lett. **12**, 483 (1987).

[41] P. M. Paul, E. S. Toma, P. Breger, G. Mullot, F. Auge, Ph. Balcou, H. G. Muller and P. Agostini, Science **292**, 1689 (2001).

[42] M. Hentschel, R. Kienberger, Ch. Spielmann, G. A. Reider, N. Milosevic, T. Brabec, P. Corkum, U. Heinzmann, M. Drescher and F. Krausz, Nature **414**, 509 (2001).

[43] Y. Silberberg, Nature **414**, 494 (2001).

[44] *Newport Resource Catalog 2004*, Newport Inc. (2004), `www.newport.com` .

[45] V. G. Dmitriev, G. G. Gurzadyan, D. N. Nikogosyan, *Handbook of Nonlinear Optical Crystals*, 3rd edition, Springer (1999).

[46] E. B. Treacy, IEEE J. Quant. Electr. **5**, 454 (1969).

[47] F. J. Duarte and J. A. Piper, Opt. Comm. **43**, 303 (1982).

[48] R. L. Fork, O. E. Martinez and J. P. Jordan, Opt. Lett. **9**, 150 (1984).

[49] G. D. Reid, K. Wynne, *Ultrafast Laser Technology and Spectroscopy*, from *Encyclopedia of Analytical Chemistry* (p.13644), J. Wiley & Sons (2000).

[50] Coherent Inc., Santa Clara, CA, USA.

[51] C. V. Shank, R. Yen and C. Hirlimann, Phys. Rev. Lett. **50**, 454 (1983).

[52] S. Williamson and G. Mourou, Phys. Rev. Lett. **52**, 2364 (1984).

[53] C. Rose-Petruck, R. Jimenez, T. Guo, A. Cavalleri, C. W. Siders, F. Ráksi, J. A. Squier, B. C. Walker, K. R. Wilson and C. P. J. Barty, Nature **398**, 310 (1999).

[54] P. A. Franken, A. E. Hill, C. W. Peters and G. Weinreich, Phys. Rev. Lett. **7**, 118 (1961).

[55] A. Yariv and P. Yeh, *Optical Waves in Crystals*, J. Wiley & Sons (2003).

[56] N. Boeuf, Opt. Eng. **39**, 1016 (2000).

[57] M. Maier, W. Kaiser and J. A. Giordmaine, Phys. Rev. Lett. **17**, 1275 (1966).

[58] W. Demtröder, *Laser Spectroscopy*, 2nd edition, Springer (1998).

[59] K. L. Sala, G. A. Kenney-Wallace and G. E. Hall, IEEE J. Quant. Electr. **16**, 990 (1980).

[60] C. Chen, B. Wu, A. Jiang, G. You, Scienta Sinica, Ser. B **28**, 235 (1985).

[61] R. Trebino, E. K. Gustafson and A. E. Siegman, J. Opt. Soc. Amer. B **3**, 1295 (1986).

[62] R. W. Gerchberg and W. O. Saxton, Optik **35** 237 (1972).

[63] J. Peatross and A. Rundquist, J. Opt. Soc. Amer. B **15**, 216 (1998).

[64] J.-C. Diels, J. J. Fontaine and F. Simoni, *Proceedings of the International Conference on Lasers*, STS Press: McLean VA, p.348 (1983).

[65] P. O'Shea, M. W. Kimmel, X. Gu and R. Trebino, Opt. Express **7**, 342 (2000).

[66] A. M. Weiner, IEEE J. Quant. Electr. **19**, 1276 (1983).

[67] J. I. Dadap, G. B. Focht, D. H. Reitze and M. C. Downer, Opt. Lett. **16**, 499 (1991).

[68] B. Lamprecht, A. Leitner and F. R. Aussenegg, Appl. Phys. B **64**, 269 (1997).

[69] B. Lamprecht, A. Leitner and F. R. Aussenegg, Appl. Phys. B **68**, 419 (1999).

[70] K. Naganuma, K. Mogi and H. Yamada, IEEE J. Quant. Electr. **25**, 1225 (1989).

[71] J.-C. Diels, J. J. Fontaine, N. Jamasbi, M. Lai and J. Mackey, *Femto-nitpicker*, in *Digest of Conference on Lasers and Electro-Optics*, Opt. Soc. Amer., paper MD3 (1987).

[72] C. Yan and J.-C. Diels, J. Opt. Soc. Am. B **8**, 1259 (1991).

[73] R. Trebino and D. J. Kane, J. Opt. Soc. Amer. A **10**, 1101 (1993).

[74] R. Trebino, K. W. DeLong, D. N. Fittinghoff, J. N. Sweetser, M. A. Krumbgel and D. J. Kane, Rev. Sci. Instrum. **68**, 3277 (1997).

[75] C. Radzewicz, P. Wasylczyk and J. S. Krasinski, Opt. Commun. **186**, 329 (2000).

[76] P. O'Shea, M. Kimmel, X. Gu and R. Trebino, Opt. Lett. **26**, 932 (2001).

[77] M. Allan, Advanced Laboratory Work, University of Zürich (2005).

[78] A. Einstein, Ann. Phys. **37**, 666 (1905).

[79] S. Hüfner, *Photoelectron Spectroscopy*, 3rd edition, Springer (2003).

[80] A. L. Fetter and J. D. Walecka, *Quantum Theory of Many-Particle Systems*, Dover Publications (2003).

[81] L. D. Landau, Soviet Phys. JETP. **3**, 920 (1957).

[82] D. E. Eastman, D. A. Knapp and F. J. Himpsel, Phys. Rev. Lett. **41**, 825 (1978).

[83] N. V. Smith, P. Thiry and Y. Petroff, Phys. Rev. B **47**, 15476 (1993).

[84] R. Matzdorf, Surf. Sci. Reports **30**, 153 (1998).

[85] F. Manghi, V. Bellini, J. Osterwalder, T. J. Kreutz, P. Aebi and C. Arcangeli, Phys. Rev. B **59**, R10409 (1999).

[86] C. N. Berglund and W. E. Spicer, Phys. Rev. **136**, A1030 and A1044 (1964).

[87] J. Osterwalder, Surf. Rev. Lett. **4**, 391 (1997).

[88] J. Osterwalder, P. Aebi, R. Fasel, D. Naumovic, P. Schwaller, T. Kreutz, L. Schlapbach, T. Abukawa and S. Kono, Surf. Sci. **331-333**, 1002 (1995).

[89] T. Greber, J. Wider, E. Wetli and J. Osterwalder, Phys. Rev. Lett. **81**, 1654 (1998).

[90] P. Aebi, J. Osterwalder, R. Fasel, D. Naumovic, L. Schlapbach, Surf. Sci. **307-309**, 917 (1994).

[91] J. Osterwalder, private comunications.

[92] M. J. Weida, S. Ogawa, H. Nagano, H. Petek, J. Opt. Soc. Am. B **17**, 1443 (2000).

[93] S. Mukamel, *Nonlinear Optical Spectroscopy*, Oxford University Press (1995).

[94] J. Bokor, R. Storz, R. R. Freeman, P. H. Bucksbaum, Phys. Rev. Lett. **57**, 881 (1986).

[95] M. Aeschlimann, S. Pawlik, M. Bauer, Ber. Bunsenges. Phys. Chem. **99**, 1504 (1995).

[96] M. Aeschlimann, M. Bauer, S. Pawlik, W. Weber, R. Burgermeister, D. Oberli, H. C. Siegmann, Phys. Rev. Lett. **79**, 5158 (1997).

[97] K. Giesen, F. Hage, F. J. Himpsel, H. J. Riess, W. Steinmann, Phys. Rev. Lett. **55**, 300 (1985).

[98] T. Fauster, M. Weinelt, J. Elecrton Spectrosc. Relat. Phenom. **114-116**, 269 (2001).

[99] N. Pontius, V. Sametoglu, H. Petek, Phys. Rev. B **72**, 115105 (2005).

[100] S. Pawlik, R. Burgermeister, M. Bauer, M. Aeschlimann, Surf. Sci. **402-404**, 556 (1998).

[101] K. Giesen, F. Hage, F. J. Himpsel, H. J. Riess, W. Steinmann, Phys. Rev. B **33**, 5241 (1986).

[102] M. Wolf, A. Hotzel, E. Knoesel, D. Velic, Phys. Rev. B **59**, 5926 (1999).

[103] M. Bovet, V. N. Strocov, F. Clerc, C. Koitzsch, D. Naumovic, P. Aebi, Phys. Rev. Lett. **93**, 107601 (2004).

[104] M. S. Pshenichnikov, K. Duppen and D. A. Wiersma, Phys. Rev. Lett. **74**, 674 (1995).

[105] S. Weiss, M.-A. Mycek, J.-Y. Bigot, S. Schmitt-Rink and D. S. Chemla, Phys. Rev. Lett. **69**, 2685 (1992).

[106] D.-S. Kim, J. Shah, T. C. Damen, W. Schäfer, F. Jahnke, S. Schmitt-Rink and K. Köhler, Phys. Rev. Lett. **69**, 2725 (1992).

[107] H. Ueba, Surf. Sci. Lett. **334**, 719 (1995).

[108] H. Ueba, personal webpage `http://surfst00.eng.toyama-u.ac.jp /~ueba/works/time-resolved-2ppe.html`

[109] C. D. Lindstrom, Daniel Quinn and X.-Y. Zhua, J. of Chem. Phys. **122**, 124714 (2005).

[110] X.-Y. Zhu, Surf. Sci. Rep. **56**, 1 (2004).

[111] E. Knoesel, A. Hotzel and M. Wolf, J. Electr. Spec. and Rel. Phen. **88-91**, 577 (1998).

[112] T. Greber, T. J. Kreutz and J. Osterwalder, Phys. Rev. Lett. **79**, 4465 (1997).

[113] T. Greber, O. Raetzo, T. J. Kreutz, P. Schwaller, W. Deichmann, E. Wetli and J. Osterwalder, Rev. Sci. Instrum. **68**, 4549 (1997).

[114] W. Auwärter, M. Muntwiler, J. Osterwalder and T. Greber, Surf. Sci. **545**, 735 (2003).

[115] W. Di, S. Dhar, K. E. Smith and S. D. Kevan, Phys. Rev. B **49**, 4821 (1994).

[116] D. A. Papaconstantopoulos, Handbook of the Band Structure of Elemental Solids, Penum Press (1986).

[117] C. Tarrio and S. E. Schnatterly, Phys. Rev B **40**, 7852 (1989).

[118] W. Steinmann, Appl. Phys. A **49**, 365 (1989).

[119] U. Höfer, I. L. Shumay, C. Reu, U. Thomann, W. Wallauer and T. Fauster, Science **277**, 1480 (1997).

[120] M. Hengsberger *et al.*, to be published.

[121] M. Muntwiler, M. Hengsberger, A. Dolocan, H. Neff, T. Greber and J. Osterwalder, submitted to PRB (2006).

[122] A. Nagashima, N. Tejima, Y. Gamou, T. Kawai and C. Oshima, Phys. Rev. Lett. **75**, 3918 (1995).

[123] Y. Gamou, M. Terai, A. Nagashima and C. Oshima, Sci. Rep. Res. Inst. Tohoku Univ. **A44**, 211 (1997).

[124] W. Auwärter, T. J. Kreutz, T. Greber and J. Osterwalder, Surf. Sci. **429**, 229 (1999).

[125] M. Muntwiler, W. Auwärter, F. Baumberger, M. Hoesch, T. Greber and J. Osterwalder, Surf. Sci. **472**, 125 (2001).

[126] G. B. Grad, P. Blaha, K. Schwarz, W. Auwärter and T. Greber, Phys. Rev. B 68, 085404 (2003).

[127] M. S. Rogalski and S. B. Palmer, *Solid State Physics*, Gordon and Breach Science Publications (2000).

[128] S. Ogawa and H. Petek, Surface Science **357-358**, 585 (1996).

[129] D. G. Castner, G. A. Somorjai, J. E Black, D. Castiel and R. F. Wallis, Phys. Rev. B **24**, 1616 (1981).

[130] R.Laskowski, P.Blaha, T.Gallauner and K.Schwarz, *Boron notride nanomesh on metal surfaces*, 21st Workshop on Novel Materials, Planneralm, Austria, 11-18.2.2006 (TUW).

[131] C. Davisson and L. H. Germer, Phys. Rev. **30**, 705 (1927).

[132] A. Zangwill, *Physics at Surfaces*, Cambridge University Press (1996).

[133] M. P. Marder, *Condensed Matter Physics*, J. Wiley & Sons (2000).

[134] T. Abukawa, M. Sasaki, F. Hisamatsu, T. Goto, T. Kinoshita, A. Kakizaki and S. Kono, Surf. Sci. **325**, 33 (1995).

[135] O. Bunk, G. Falkenberg, J.H. Zeysing, L. Lottermoser, R.L. Johnson, M. Nielsen, F. Berg-Rasmussen, J. Baker and R. Feidenhans'l, Phys. Rev. B **59**, 12228 (1999).

[136] C. Kumpf, O. Bunk, J.H. Zeysing, Y. Su, M. Nielsen, R.L. Johnson, R. Feidenhans'l and K. Bechgaard, Phys. Rev. Lett. **85**, 4916 (2000).

[137] O. Gallus, T. Pillo, M. Hengsberger, P. Segovia and Y. Baer, Eur. Phys. J. B **20**, 313 (2001).

[138] D. J. Chadi and C. Chiang, Phys. Rev. B **23**, 1843 (1981).

[139] X. Zeng and H. E. Elsayed-Ali: Phys. Rev. B **64**, 085410 (2001).

[140] M. Dantus, S. B. Kim, J. C. Williamson and A. H. Zewail, J. Phys. Chem. **98**, 2782 (1994).

[141] J. C. Williamson, J. Cao, H. Ihee, H. Frey and A. H. Zewail, Nature **386**, 159 (1997).

[142] H. Ihee, J. Cao and A. H. Zewail, Chem. Phys. Lett. **281**, 10 (1997).

[143] H. E. Elsayed-Ali and G. A. Mourou, Appl. Phys. Lett. **52**, 103 (1988).

[144] H. E. Elsayed-Ali and J. W. Herman, Appl. Phys. Lett. **57**, 1508 (1990).

[145] X. Zeng, B. Lin, I. El-Kholy and H. E. Elsayed-Ali, Phys. Rev. B **59**, 14907 (1999).

[146] C. -Y. Ruan, F. Vigliotti, V. A. Lobastov, S. Chen and A. H. Zewail, Proc. Nat. Acad. Sci. **101**, 1123 (2004).

[147] J. R. Thompson, P. M. Weber and P. J. Estrup, Proc. SPIE **2521**, 113 (1995).

[148] H. Ihee, V. A. Lobastov, U. M. Gomez, B. M. Goodson, R. Srinivasan, C. -Y. Ruan and A. H. Zewail, Science **291**, 458 (2001).

[149] A. A. Zholents and M. S. Zolotorev, Phys. Rev. Lett. **76**, 912 (1996).

[150] R. W. Schoenlein, S. Chattopadhyay, H. H. W. Chong, T. E. Glover, P. A. Heimann, C. V. Shank, A. A. Zholents and M. S. Zolotorev, Science **287**, 2237 (2000).

[151] J. C. Williamson and A. H. Zewail, Chem. Phys. Lett. **209**, 10 (1993).

[152] B. J. Siwick, J. R. Dwyer, R. E. Jordan and R. J. D. Miller, J. Appl. Phys. **92**, 1643 (2002).

[153] J. G. Fujimoto, J. M. Liu, E. P. Ippen and N. Bloembergen, Phys. Rev. Lett. **53**, 1837 (1984).

[154] R. Karrer: Diploma Thesis, University of Zürich, Switzerland (2000) [in German].

[155] M. Aeschlimann, E. Hull, J. Cao, C. A. Schuttenmaer, L. G. Jahn, Y. Gao, H. E. Elsayed-Ali, D. A. Mantell and M. R. Scheinfein, Rev. Sci. Instrum. **66**, 1000 (1995).

[156] M. Aeschlimann, E. Hull, C. A. Schmuttenmaer, J. Cao, Y. Gao, D. A. Mantell and H. E. Elsayed-Ali, Proc. SPIE **2521**, 103 (1995).

[157] SIMION 3D 7.0 software package, Idaho National Engineering Laboratory, EG&G Idaho Inc., Idaho Falls.

Acknowledgments

Since I first met Prof. Jürg Osterwalder I was fascinated by his astonishing capacity of pointing people in the right direction even in the most difficult situations. Thanking him is simply not enough to show my gratitude for his continuous help and understanding. I have no doubt that his strong character and brilliant scientific insight will be the guiding model for many generations of students. With his enthusiasm and hard work Prof. Thomas Greber is keeping the group connected. He has always been there for me when I needed help and he never sized to amaze me with his ingenious ideas. My supervisor, Matthias Hengsberger (Matze), was my officemate for almost two years. Most of my experimental and theoretical knowledge is a result of his guiding and teachings. We shared also the same passion for sports and computers. Above all, he was a friend in the true sense of the word. Hansjörg Neff deserves my special thanks since he was my guide during the first steps I took in the Laser Lab. His fascinating teachings will never be forgotten. Being around him and Matze was a great experience, a true life lesson. My officemate in the last year, Jorge Lobo is one of the funniest persons I have ever met. His joyful character was the perfect help when I was feeling down. Together with him and Taichi Okuda, a visiting postdoc from Japan, we enjoyed many coffees and interesting discussions. Nevertheless, Taichi deserves my gratitude for introducing me to the group of Prof. Shigekawa and for helping me in many other ways.

I received a lot of help in the ESCA from Martina Corso who introduced me to her beautiful *nanomesh*. Most of my 2PPE experiments would not have been possible without her magic hands. Claudio Cirelli was my lab-mate for three years. Almost all my experiments in the Laser Lab benefited from his enthusiasm. With both of them I also shared the teaching pleasures of the experimental labs. Nevertheless, it was a great pleasure to work with all the other colleagues from the surface physics group: Matthias Muntwiler, Willi Auwärter, Felix Baumberger, Moritz Hoesch, Simon Berner, Carine Galli Marxer, Anna Tamai, Mike Barry, Martin Morscher, and many other who I apologize for omitting. They accepted me and made me feel like I belonged to the group even though I did not always answered them in the same way.

Many problems I had in the Laser Lab were solved after enlighting discussions with Prof. Peter Hamm from the Chemical Physics Department. His door was always open for me and I thank him for his continuous guiding.

Most of my technical problems were solved fast and elegant by Werner Deichmann and Martin Klökner. Also, the devices our in-house workshop built for me were at the highest quality level. For that, I give my special thanks to Bernhard Schmid and Kurt Bösiger.

In the end, I would like to thank my family for their continuous support and understanding, especially my parents, my aunt Laura and my girlfriend Raluca.

Curriculum Vitae

Name	Andrei D. Dolocan
Birth	07.09.1977 in Bucharest, Romania
Nationality	Romanian

Education

1992 - 1996	Theoretical High School *Ion Creanga*, Bucharest, Romania
Jun 1996	Bacalaureat Diploma
1996 - 2001	University of Bucharest, Faculty of Physics, specialization Technological Physics
Oct 1999 - Mar 2000	SOCRATES-ERASMUS student in the Institut of Theoretical Physics (ITP) Hanover, Germany
Oct 2000 - Jun 2001	Diploma work in the Solid State Theory Group of Prof. Dr. G. Nenciu (Faculty of Physics) **Thesis Title** : *Dynamics of Band Electrons in Weak Electric Fields* supervisor : Prof. Dr. G. Nenciu
Jun 2001	Graduation with mark 9.86 (on a scale 1-10, 10 being the maximum)
Nov 2001 - May 2002	Practical Training in the group of Prof. Dr. J. F. van der Veen, Swiss Light Source (SLS), Villigen, Switzerland.
since Jun 2002	Employed as PhD student in the Surface Physics Group of Prof. Dr. Jürg Osterwalder, University of Zurich
Jul 2006	PhD Thesis; **Title** : *Time-Resolved Low-Energy Electron Diffraction and Photoemission Pump-Probe Experiments* supervisors : Prof. Dr. J. Osterwalder and Dr. M. Hengsberger

Teaching Experience

since Jun 2002	Teaching Assistant, University of Zurich; Taught lab-courses for physics, medical and biology students and problem classes in the Physics 3 advanced physics course.